WL-TR-95-4094

NOVEL NDE FOR CORROSION DETECTION:
NUCLEAR MAGNETIC RESONANCE

DONALD D. PALMER

MCDONNELL DOUGLAS AEROSPACE
P.O. BOX 516
ST. LOUIS, MO 63166

DAVID M. SNYDERMAN
MARK S. CONRADI

WASHINGTON UNIVERSITY
DEPARTMENT OF PHYSICS
ST. LOUIS, MO 63130

JANUARY 1996

FINAL REPORT FOR 09/30/93 - 11/30/95

APPROVED FOR PUBLIC RELEASE; DISTRIBUTION IS UNLIMITED

19960617 120

WRIGHT LABORATORY
MATERIALS DIRECTORATE
AIR FORCE MATERIEL COMMAND
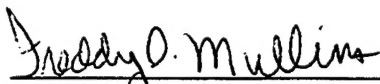WRIGHT-PATTERSON AFB OH 45433-7734

DTIC QUALITY INSPECTED 1

NOTICE

WHEN GOVERNMENT DRAWINGS, SPECIFICATIONS, OR OTHER DATA ARE USED FOR ANY PURPOSE OTHER THAN IN CONNECTION WITH A DEFINITELY GOVERNMENT-RELATED PROCUREMENT, THE UNITED STATES GOVERNMENT INCURS NO RESPONSIBILITY OR ANY OBLIGATION WHATSOEVER. THE FACT THAT THE GOVERNMENT MAY HAVE FORMULATED OR IN ANY WAY SUPPLIED THE SAID DRAWINGS, SPECIFICATIONS, OR OTHER DATA, IS NOT TO BE REGARDED BY IMPLICATION OR OTHERWISE IN ANY MANNER CONSTRUED, AS LICENSING THE HOLDER OR ANY OTHER PERSON OR CORPORATION, OR AS CONVEYING ANY RIGHTS OR PERMISSION TO MANUFACTURE, USE, OR SELL ANY PATENTED INVENTION THAT MAY IN ANY WAY BE RELATED THERETO.

THIS REPORT IS RELEASABLE TO THE NATIONAL TECHNICAL INFORMATION SERVICE (NTIS). AT NTIS, IT WILL BE AVAILABLE TO THE GENERAL PUBLIC, INCLUDING FOREIGN NATIONS.

THIS TECHNICAL REPORT HAS BEEN REVIEWED AND IS APPROVED FOR PUBLICATION.

FREDDY D. MULLINS
Nondestructive Evaluation Branch
Metals and Ceramics Division

TOBEY M. CORDELL, Chief
Nondestructive Evaluation Branch
Metals and Ceramics Division

WALTER M. GRIFFITH, Asst Chief
Metals and Ceramics Division
Materials Directorate

IF YOUR ADDRESS HAS CHANGED, IF YOU WISH TO BE REMOVED FROM OUR MAILING LIST, OR IF THE ADDRESSEE IS NO LONGER EMPLOYED BY YOUR ORGANIZATION, PLEASE NOTIFY, WL/MLLN, WRIGHT-PATTERSON AFB OH 45433-7817 TO HELP US MAINTAIN A CURRENT MAILING LIST.

COPIES OF THIS REPORT SHOUL.D NOT BE RETURNED UNLESS RETURN IS REQUIRED BY SECURITY CONSIDERATIONS, CONTRACTUAL OBLIGATIONS, OR NOTICE ON A SPECIFIC DOCUMENT.

REPORT DOCUMENTATION PAGE

FORM APPROVED
OMB NO. 0704-0188

1. AGENCY USE ONLY *(Leave Blank)*	2. REPORT DATE JANUARY 1996	3. REPORT TYPE AND DATES COVERED FINAL REPORT/30 SEP 93 - 30 NOV 95

4. TITLE AND SUBTITLE

NOVEL NDE FOR CORROSION DETECTION:
NUCLEAR MAGNETIC RESONANCE

5. FUNDING NUMBERS

F33615-93-C-5369
PE 62102F
PR 2418
TA 40
WU 09

6. AUTHOR(S)

DONALD D. PALMER, MCDONNELL DOUGLAS AEROSPACE
DAVID M. SNYDERMAN AND MARK S. CONRADI, WASHINGTON UNIVERSITY

7. PERFORMING ORGANIZATION NAME(S) AND ADDRESS(ES)

MCDONNELL DOUGLAS AEROSPACE
P.O. BOX 516
ST. LOUIS, MO 63166

8. PERFORMING ORGANIZATION REPORT NUMBER

9. SPONSORING MONITORING AGENCY NAME(S) AND ADDRESS(ES)

MATERIALS DIRECTORATE
WRIGHT LABORATORY
AIR FORCE MATERIEL COMMAND
WRIGHT-PATTERSON AFB, OH 45433-7734

10. SPONSORING/MONITORING AGENCY REP NUMBER

WL-TR-95-4094

11. SUPPLEMENTARY NOTES

12a. DISTRIBUTION/AVAILABILITY STATEMENT

APPROVED FOR PUBLIC RELEASE; DISTRIBUTION IS UNLIMITED

12b. DISTRIBUTION CODE

13. ABSTRACT

Nuclear magnetic resonance (NMR), a technique utilized extensively in the medical, chemical and petroleum industries, has shown to be very sensitive to corrosion and moisture entrapped in aircraft structures in cursory studies performed prior to this program. Both aluminum and hydrogen NMR techniques were evaluated relative to sensitivity to thin layers of corrosion on several aluminum alloys and a high strength steel. Other hydrogen-bearing aerospace materials were characterized to determine if discrimination between these materials and corrosion could be made relative to hydrogen NMR. RF magnetic field modelling was performed using two- and three-dimensional electromagnetic modelling codes to determine if RF magnetic fields could penetrate through gaps in joints and around fasteners. Actual RF magnetic field penetration was determined experimentally using simplified butt-joint, lap joint and fastener hole structures. The potential for detecting actual corrosion in these structures was also evaluated experimentally. In addition, the ability to detect corrosion under paint, primer and sealant was determined. Recommendations for future work relative to NMR as an inspection tool for detection and characterization of corrosion are included.

14. SUBJECT TERMS

Nuclear Magnetic Resonance (NMR), Knight Shift, Spin-Lattice Relaxation, Spin-Spin Relaxation, RF Magnetic Field, Pulse Sequence, Solenoidal Coil, Figure-Eight Coil, Superconducting Magnet, Electromagnet, Permanent Magnet

15. NUMBER OF PAGES

88

16. PRICE CODE

17. SECURITY CLASSIFICATION OF REPORT UNLIMITED	18. SECURITY CLASS OF THIS PAGE UNLIMITED	19. SECURITY CLASS OF ABSTRACT UNLIMITED	20. LIMITATION ABSTRACT SAR

Standard Form 298 (Rev 2-89)
Prescribed by ANSI Std Z239-18
298-102

TABLE OF CONTENTS

Page

LIST OF FIGURES

	Title	**Page**

PREFACE

This report describes the work performed under U.S. Air Force contract F33615-93-C-5369, "Novel NDE for Corrosion Detection: Nuclear Magnetic Resonance", from 30 September 1993 to 30 November 1995. This report is submitted in compliance with the subject contract, CDRL Item A004. The technical effort was managed by McDonnell Douglas Aerospace (MDA), P.O. Box 516, St. Louis, MO 63166, under the direction of Capt. Greg Jablunovsky and Fred Mullins at Wright Laboratory (WL/MLLP).

The program was conducted by the NDE Development Group of the New Aircraft and Missile Products Division of MDA under the direction of Donald D. Palmer, Program Manager and Dr. Arthur C. Lind, Principal Investigator. Major contributors of the multi-disciplinary team include Elias Malakelis (Specimen Preparation), Douglas J. Peterman (Corrosion Characterization) and Dau-Sing Wang (NMR Modelling). The NMR sensitivity measurements, RF magnetic field experimental study and NMR detection of corrosion in simple structures were performed by Washington University, St. Louis, MO, in conjunction with MDA. Specific contributions in these areas were made by David M. Snyderman and Dr. Mark S. Conradi of the Department of Physics Solid State NMR Laboratory at Washington University.

1.0 INTRODUCTION

1.1 Program Background

With forecasted reductions in defense spending, there is an ever present need to increase the service life of aircraft currently in the Air Force inventory. This requirement has made the detection and characterization of hidden and inaccessible corrosion the Air Force number one ranked technical need. While the problem with corrosion is primarily economic, safety is also a major concern. As the airframe ages, the potential for failure resulting from stress corrosion induced cracking, disbonding of stiffeners and structural weakening due to loss of material increases. Current field inspection technologies, including ultrasonics, radiography and eddy current require 5-10% loss of material for reliable detection of corrosion.

Nuclear magnetic resonance (NMR), a technique utilized extensively in the medical, chemical and petroleum industries, has shown to be very sensitive to corrosion and moisture entrapped in aircraft structures in cursory studies performed prior to this program. Figure 1.1-1 shows aluminum NMR data collected from a corroded aluminum surface as part of a program performed for the Naval Air Warfare Center (Lakehurst, NJ) [1]. Based on these results, a more extensive study was proposed to determine the usefulness of NMR in providing a quantitative measure of the amount of corrosion present on a metallic surface. Also, the ability of using NMR to detect corrosion in joints and fastener holes and under coatings was of extreme interest in evaluating the future potential of NMR as a practical inspection method for corrosion detection.
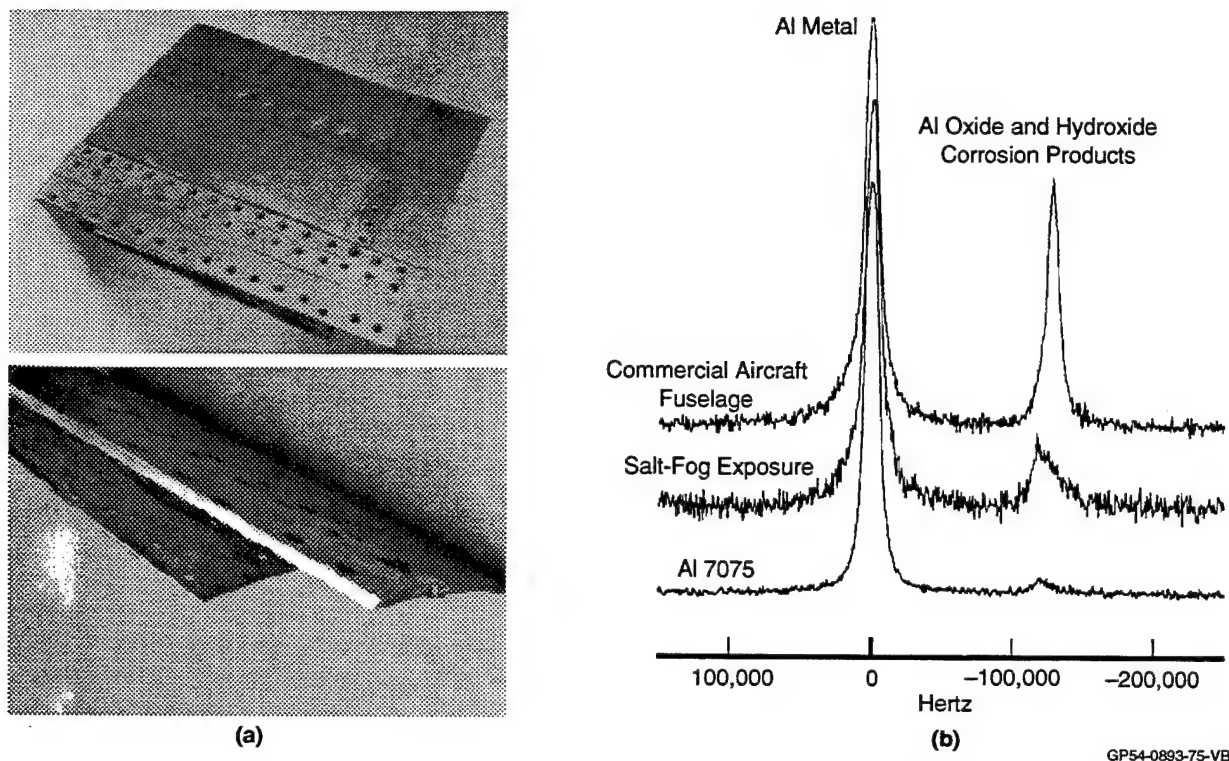
Figure 1.1-1. **(a) Corroded Aircraft Fuselage Section and (b) Initial NMR (Aluminum) Data Collected Demonstrating the Potential of the NMR Technique.**

1.2 Program Objective

The overall objective of this program was to evaluate the capabilities of nuclear magnetic resonance (NMR) as a tool for the quantitative assessment of corrosion behavior in metallic airframe structures. The specific program objectives included the following:

- Demonstrate increased sensitivity to corrosion using NMR over an established conventional nondestructive inspection (NDI) method.

- Assess the potential of using NMR signals as quantitative indicators of the amount of corrosion present.

- Determine the radio frequency (RF) magnetic field behavior in metallic structures both theoretically using electromagnetic modelling codes and experimentally using established laboratory hardware.

- Quantify the effects of coating materials, such as paint, primer and sealant, and other nonmetallic materials on NMR signals

2

1.3 Technical Approach

The technical approach devised to meet the previously stated program objectives incorporated the following two major elements:

- NMR Corrosion Characterization Sensitivity Analysis: In this task, the sensitivity of NMR as a function of the amount of corrosion present was determined. Specimens consisting of three aluminum alloys and a high strength steel were corroded in both neutral salt and SO_2 environments for specified periods of time to provide a range of corrosion layer thicknesses from nascent to a detectable level using a conventional film radiographic inspection method. The corrosion products were analyzed using Scanning Auger Microscopy (SAM) to determine product constituencies and corrosion layer thicknesses. The specimens were then evaluated using both aluminum and hydrogen NMR techniques to determine the sensitivity of each. In addition, the effects of corrosion product state of hydration as a function of temperature was evaluated.

- NMR Evaluation of Simulated Airframe Structures. In this task, the feasibility of detecting corrosion in complex airframe structures was assessed. Key to the success of NMR as a substructure corrosion detection method is the behavior of the RF magnetic field in the vicinity of joints and fastener holes. To evaluate this behavior, both 2-D and 3-D electromagnetic modelling codes were employed. In addition, NMR experiments were performed on simple aircraft structures such as a butt joint, lap joint and fastener/fastener hole combinations to verify the modelling results. To conclude this task, the ability to detect corrosion in these simple structure configurations and under coatings using NMR was experimentally determined using laboratory NMR hardware.

3

THIS PAGE INTENTIONALLY LEFT BLANK

2.0 NMR CORROSION DETECTION SENSITIVITY EVALUATION

The objective of this task was to determine the sensitivity of NMR as a function of the amount of corrosion present. Specimens consisting of three aluminum alloys and a high strength steel were corroded in both neutral salt and SO_2 environments for specified periods of time to provide a range of corrosion layer thickness from nascent to detectable using a radiographic inspection method. The corrosion products were analyzed using Scanning Auger Microscopy (SAM) to determine product constituencies and corrosion layer thicknesses. The specimens were then evaluated using both aluminum and hydrogen NMR techniques to determine the sensitivity of each. In addition, the effects of corrosion product state of hydration as a function of temperature was evaluated. The activities summarized in this paragraph are presented in more detail in the following sub-sections.

2.1 Corrosion Specimen Preparation

Specimens consisting of a variety of aluminum alloys and a high strength steel material were prepared in order to evaluate the sensitivity of nuclear magnetic resonance methods as a function of corrosion layer thickness. These specimens were ideally sized for both electron microscopy and NMR measurements. Both sets of specimens were exposed simultaneously to corrosive environments using the ASTM specification previously mentioned for specimen preparation. Sensitivity baselines were established as a function of detectability using conventional radiographic inspection methods.

2.1.1   Material Selection

The materials selected for investigation in this program were indicative of those utilized in fabrication of high performance airframe structures. These materials included three common aluminum alloys (2024-T3, 5056-H39, and 7075-T6) and a high strength steel alloy (300M). The heat treatments were chosen to provide alloys with reasonably poor corrosion resistance characteristics in order to expedite specimen preparation.

2.1.2   Corrosion Control Specimens

Two specimens for each alloy system were fabricated for exposure to corrosive environments to determine the optimum exposure time for the subsequent sensitivity analysis. Optimum exposure time was defined as the time at which pitting becomes detectable radiographically. The 2024-T3, 7075-T6 and 300M specimens were 0.063 inches in thickness and 0.43 x 0.55 inches in dimension. The 5056-H39

specimens were fabricated from actual honeycomb material to the same 0.43 x 0.55 inch dimensions. These specimens were exposed to both neutral salt (ASTM B117) and SO_2 (ASTM G85) environments. Dedicated neutral and SO_2 salt spray cabinets were used to expose the specimens; the SO_2 exposure system is shown in Figure 2.1.2-1. The specimens were removed from time to time for radiographic inspection per ASTM E94 using a Philips 160 kV static X-ray system to determine the time at which pitting becomes detectable. If pitting was detectable, the specimen was removed and the exposure time documented as optimum. If pitting was not detected, the specimen was placed back in the salt spray cabinet for continued exposure. A flow chart depicting control specimen preparation is shown in Figure 2.1.2-2. An example of radiographically detectable pitting is shown in Figure 2.1.2-3 for the 7075-T6 alloy. Figure 2.1.2-4 shows the optimum corrosion times for each alloy in both neutral salt and SO_2 environments. Based on these results, it was decided to use the SO_2 exposure for preparation of 2024-T3, 7075-T6 and 300M sensitivity specimens and the neutral salt environment for the 5056-H39 sensitivity specimens. This decision was made due to the significantly longer time period required to generate pitting in the 2024-T3 and 7075-T6 alloys. Since pitting was not observed in the 2024-T3 specimen at the time this decision was made, specimen exposure in the neutral salt environment was terminated. The neutral salt environment was chosen in lieu of the SO_2 environment for the 5056-H39 alloy due to extremely rapid degradation of the foil in the SO_2 cabinet.

(a)　　　　　　　　　　　　　　　　　　　　(b)　　　GP34-0053-36-VB
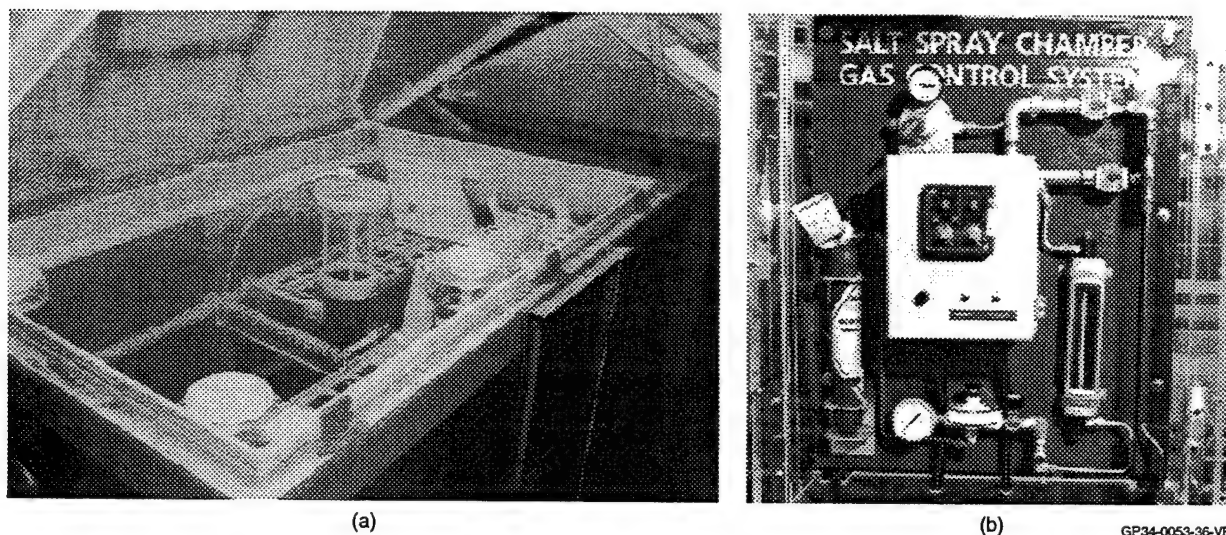
Figure 2.1.2-1. (a) Salt Spray Cabinet and (b) SO_2 Controller Used in Preparation of Corrosion Control and Sensitivity Specimens.
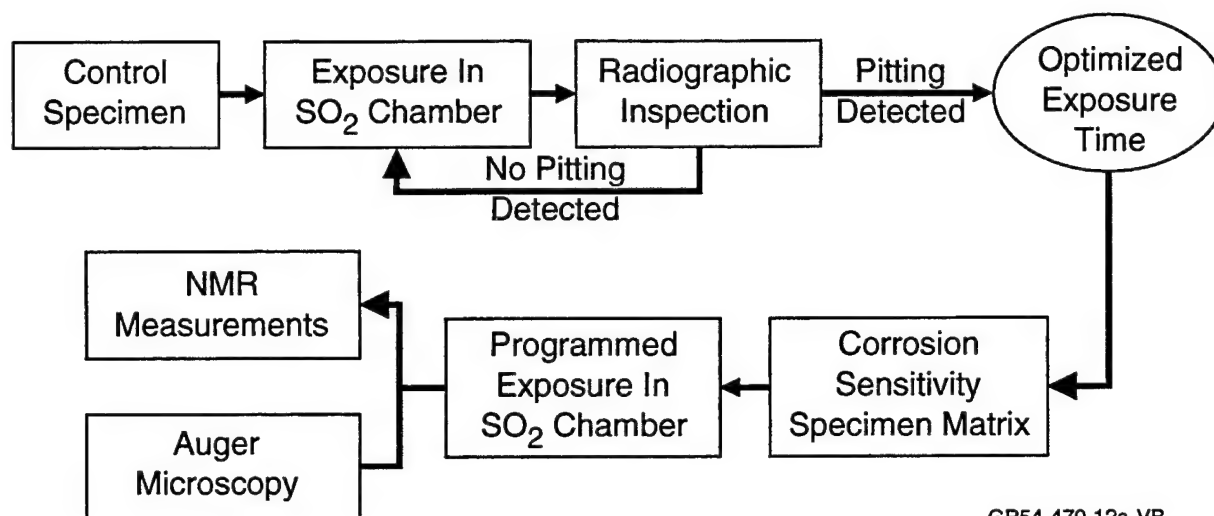
Figure 2.1.2-2. Flow Chart Illustrating Control and Sensitivity Specimen Preparation Process.

GP54-470-12a-VB
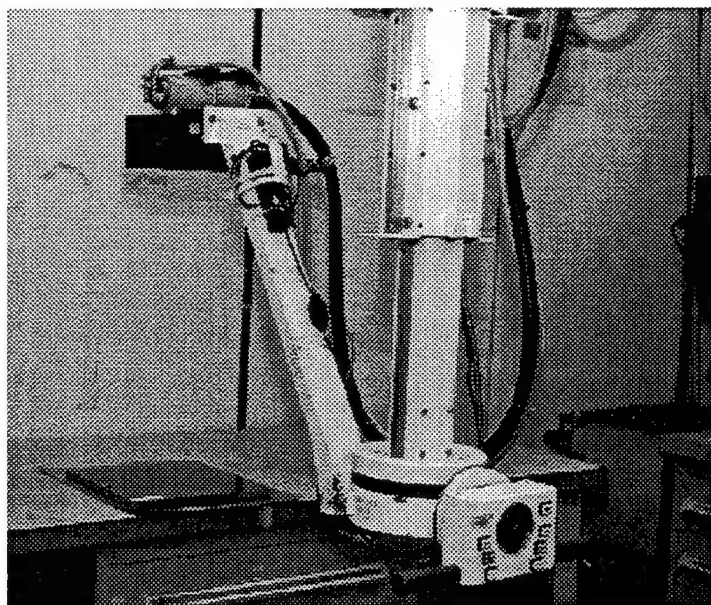
GP54-0470-16a-VC
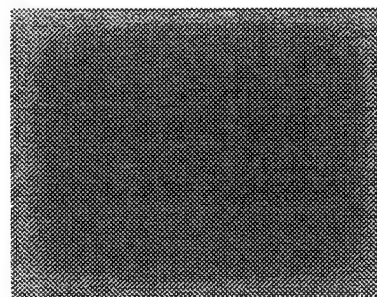
Reference Standard
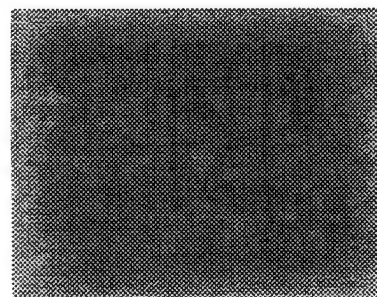
48 Hours SO_2 Exposure

Figure 2.1.2-3. (a) Philips 160 kV Static X-Ray System and (b) Radiographic Inspection Results for 7075-T6 Aluminum Alloy Exposed for 48 hours in an SO_2 Environment.

7

Material	Environment	Exposure	Observations
2024-T3	Neutral SO$_2$	84 Days 7 Days	Corrosion Visible Detected Using RT
5056-H39	Neutral SO$_2$	22 Days 2 Days	Detected Using RT Disintegrated
7075-T6	Neutral SO$_2$	84 Days 2 Days	Detected Using RT Detected Using RT
300M	Neutral SO$_2$	44 Days 7 Days	Detected Using RT Detected Using RT

GP54-0470-14-VB

Figure 2.1.2-4. Optimum Corrosion Exposure Times for 2024-T3, 5056-H39, and 7075-T6 Aluminum Alloys and 300M High Strength Steel. Exposure Times Include Both Neutral Salt and SO$_2$ Environments.

2.1.3 Corrosion Sensitivity Specimens

Based on the optimum corrosion times obtained for each alloy, corrosion sensitivity specimens were fabricated. These specimens were designed to provide a range of corrosion layer thicknesses below, at and above the thickness corresponding to the optimum exposure time. This range of exposures, consisting of times equivalent to 20%, 40%, 60%, 80%, 100% and 200% of the optimum times, was developed with the goal of providing a means for demonstrating the sensitivity of the NMR technique, primarily at thicknesses undetectable using conventional radiographic inspection methods. For each alloy, an NMR specimen and an electron microscopy specimen were simultaneously exposed in the designated environment for the prescribed period of time. Separate specimens, shown in Figure 2.1.3-1, were fabricated in order to minimize handling and potential contamination. Specimen dimensions included 0.43 x 0.55 inches for the electron microscopy evaluations and 0.16 x 0.55 inches for the NMR analysis. Specimen thicknesses were equivalent to those utilized for control specimen preparation. Actual sensitivity specimen exposure times are presented in Figure 2.1.3-2 for the four alloys evaluated. It should be noted here that no further effort was expended relative to the highly magnetic 300M specimens due to the inability to obtain an NMR signal. An explanation of the problems encountered with magnetic materials is provided in Section 2.3.1. From this point on, the focus was limited to aluminum alloys only.
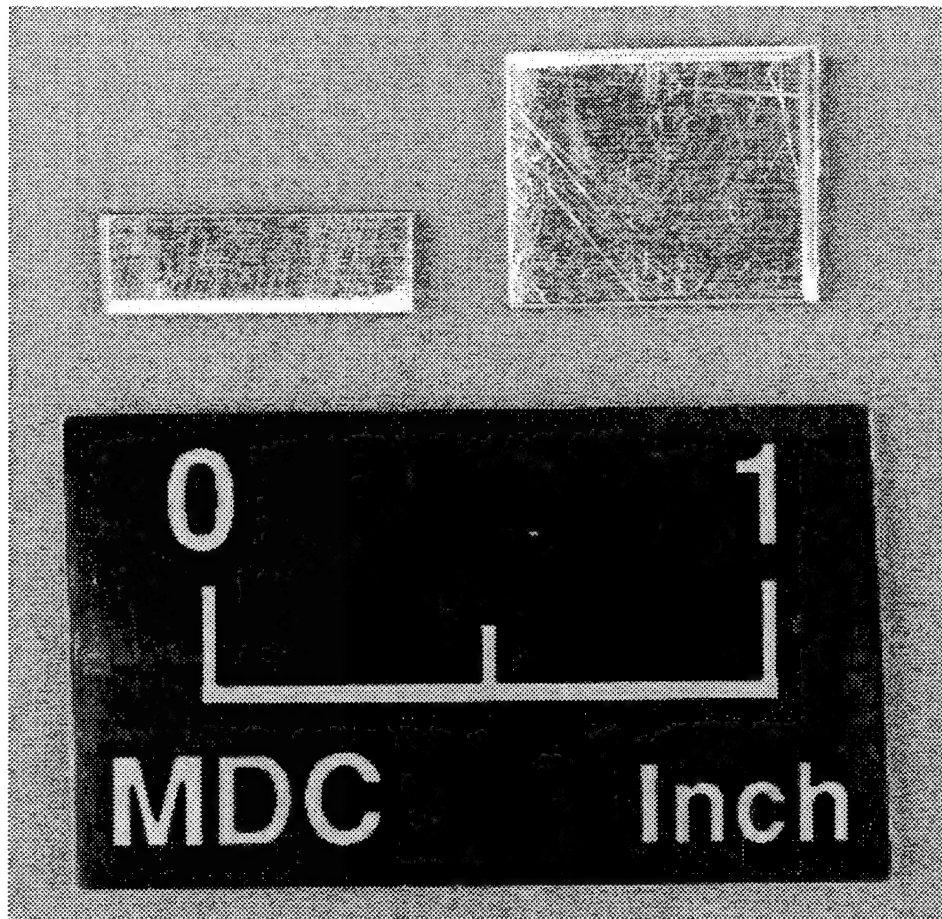
Figure 2.1.3-1. Ideally Sized Specimens for Corrosion Sensitivity Analysis: NMR (Left) and Auger Microscopy (Right).

Material	Optimum Time (Hrs)	Sensitivity Specimen Exposure Times						Environment
		1	2	3	4	5	6	
2024-T3	168	36.5	65.5	102	13.6	172.5	336	SO_2
5056-H39	528	104	188	318	43.6	594	1,056	Neutral
7075-T6	48	12	18	31	43.5	49	93.5	SO_2
300M	168	36.5	65.5	102	13.6	172.5	336	SO_2

Figure 2.1.3-2. Completed Corrosion Sensitivity Matrix Exhibiting Exposure Times for 2024-T3 and 7075-T6 Aluminum and 300M Steel (SO_2 Exposure) and 5056-H39 Aluminum (Neutral Salt Exposure).

2.2 Corrosion Characterization

The corrosion product characterization study was performed using Scanning Auger Microscopy. SAM is a powerful surface analysis tool, especially when the sample of interest has elements of low atomic number and for profiling the surface composition through the first micrometer in depth. SAM is limited by the need for the material to have at least some electrical conductivity and not to outgas in the ultra-high vacuum analysis chamber. The characterization work was performed using a Physical Electronics Model 600 Scanning Auger Microprobe, shown in Figure 2.2-1. It is equipped with dual argon ion sputter guns, an X-ray detector for energy dispersive x-ray (EDX) analysis, and an in-situ liquid nitrogen-cooled fracture stage.
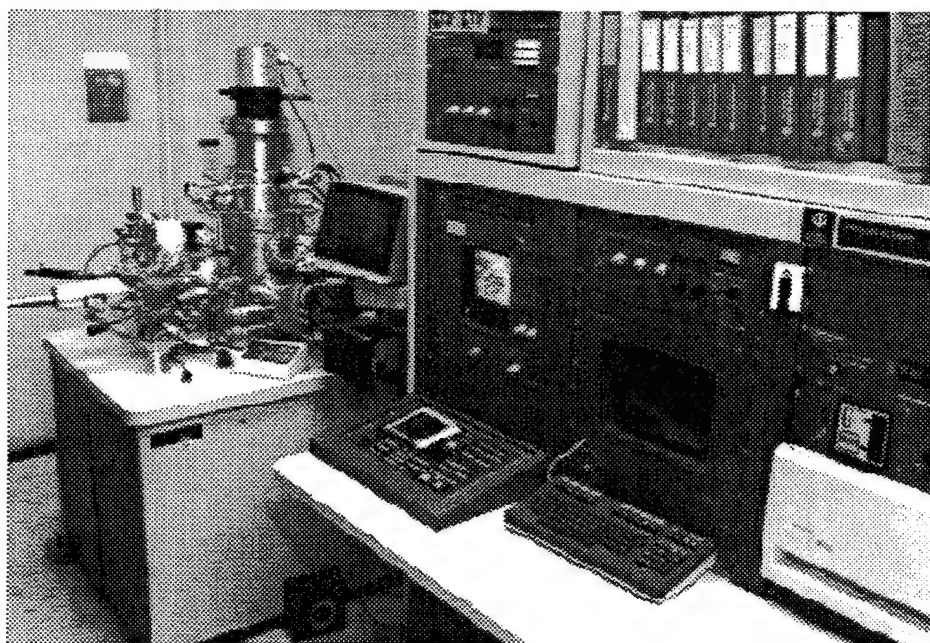
GP34-0053-37

Figure 2.2-1. Physical Electronics Model 600 Scanning Auger Microprobe.

2.2.1   Identification of Corrosion Products

Auger electron spectroscopy (AES) was used to determine the near-surface chemical composition of the 2024-T3, 5056-H39 and 7075-T6 aluminum alloys exposed to corrosive environments. Survey spectra taken from corroded specimens of each alloy are presented in Figures 2.2.1-1 through 2.2.1-4. These spectra were taken in the course of performing depth profiling measurements near the surface of the corrosion products. A survey spectrum from a 2024-T3 alloy exposed to an SO_2 environment for 102 hours is shown in Figure 2.2.1-1. The primary constituents, as was expected, were aluminum and oxygen. Also noticed were sulphur, argon, carbon and sodium. It was originally thought that copper would be present in the corrosion product for the 2024-T3 alloy; however, none was detectable due to the presence of a cladding layer. For the 7075-T6 alloy, a survey spectrum is shown in Figure 2.2.1-2 for a specimen exposed for 18 hours in an SO_2 environment. Again, the primary constituents of the corrosion product are aluminum and oxygen. Also noticed were sulphur and argon. Zinc, the primary alloying element of the 7075-T6 alloy, was not detected in the energy spectrum. This may indicate that diffusion of zinc into the oxide is limited in the early stages of oxide formation. Both the 2024-T3 and 7075-T6 alloys had sulphur present in the Auger spectrum, which is indicative of materials exposed in an SO_2 environment. In contrast, the 5056-H39 alloy specimens, exposed in a neutral salt environment, had no indication of sulphur in the corrosion product. The survey spectrum shown in Figure 2.2.1-3 for a 5056-H39 specimen exposed for 188 hours reveals chlorine and potassium in addition to aluminum and oxygen. Contaminants may also be detected using this spectroscopic technique. The survey spectrum in Figure 2.2.1-4 is also from a 5056-H39 specimen, however the exposure was greater at 594 hours. The exposure time was deceiving as the corrosion layer thickness was much less than the specimen exposed for 188 hours. By the indication of silicon in the survey spectrum, it can be assumed that the adhesive for bonding the thin sheets of material to produce the honeycomb geometry was not completely removed, causing an impediment to uniform corrosion product formation. Also noticed in the survey spectrum is chromium, which is an alloying element for the 5056-H39 alloy. Chromium was present in other 5056-H39 specimens with extremely thin corrosion product layers, indicating that chromium forms oxides on the surface, but does not diffuse into the corrosion product itself.
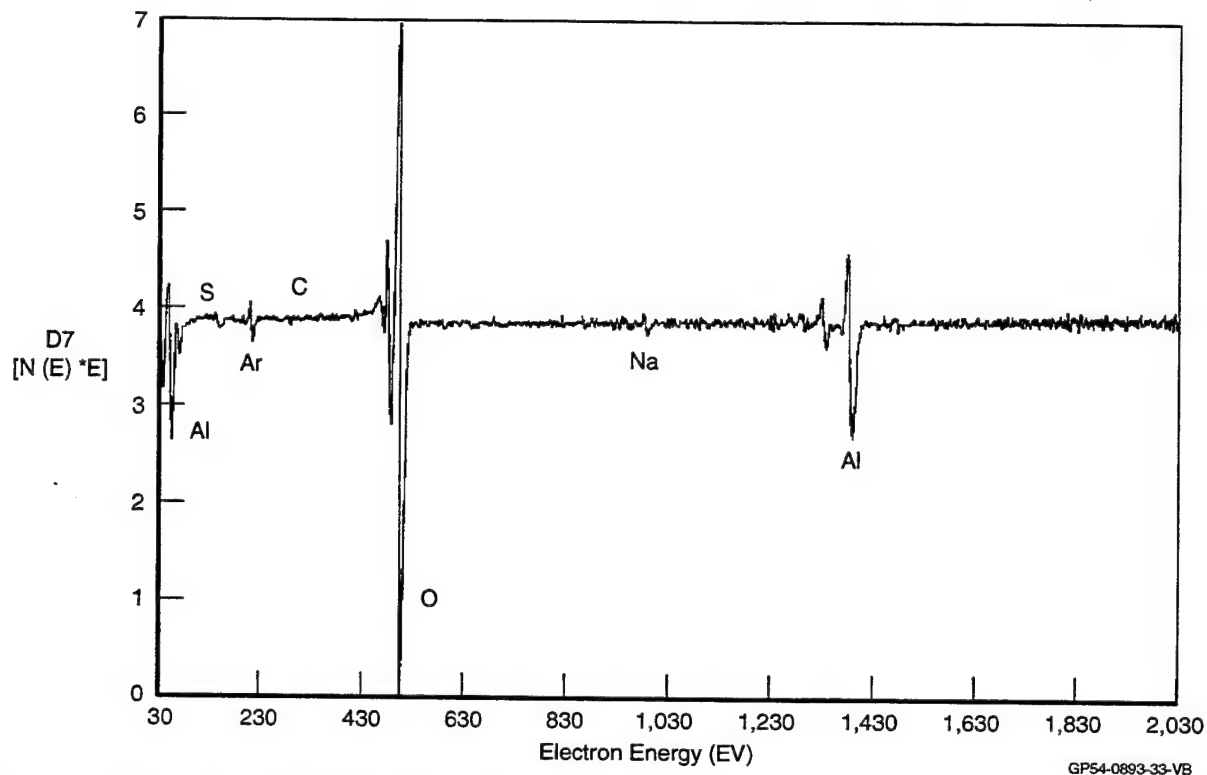
Figure 2.2.1-1. Auger Survey Spectrum for 2024-T3 Aluminum Alloy Exposed to SO$_2$ Environment for 102 hours (Sputter Time = 60 sec).
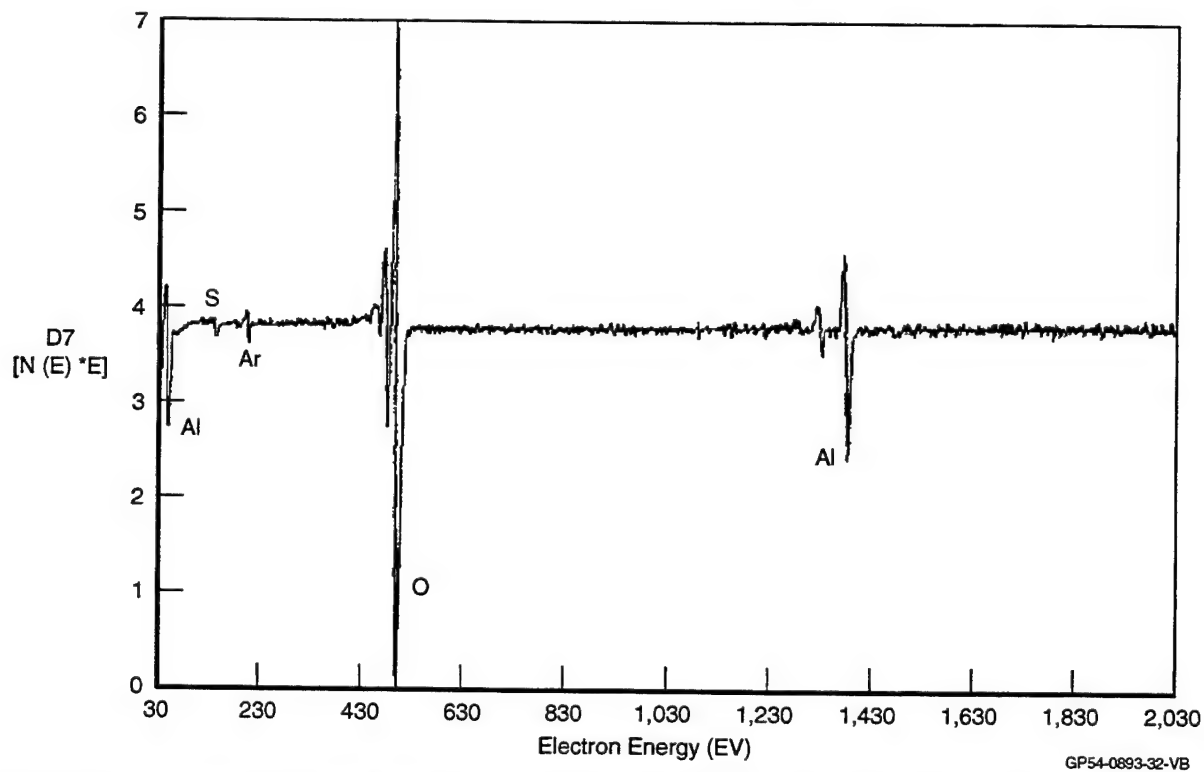
Figure 2.2.1-2. Auger Survey Spectrum for 7075-T6 Aluminum Alloy Exposed to SO$_2$ Environment for 18 hours (Sputter Time = 120 sec).

12
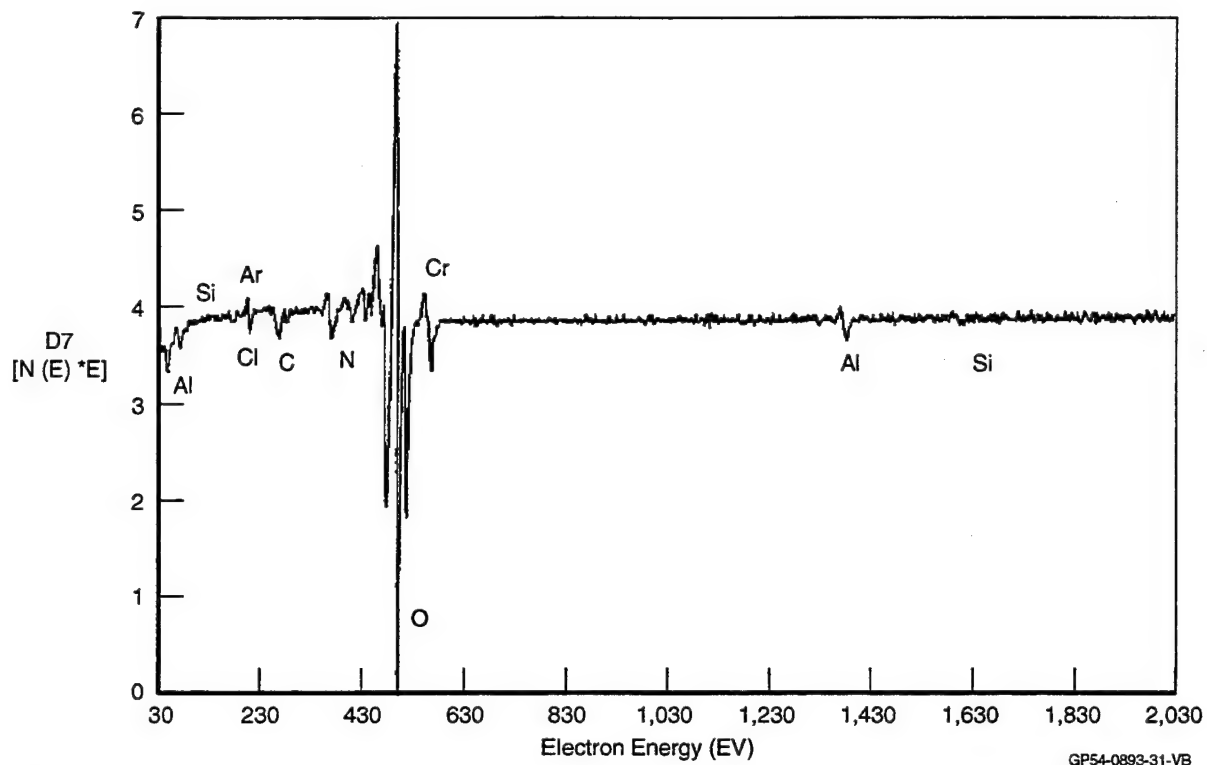
Figure 2.2.1-3. Auger Survey Spectrum for 5056-H39 Aluminum Alloy Exposed to Neutral Salt Environment for 188 hours (Sputter Time = 20 sec).
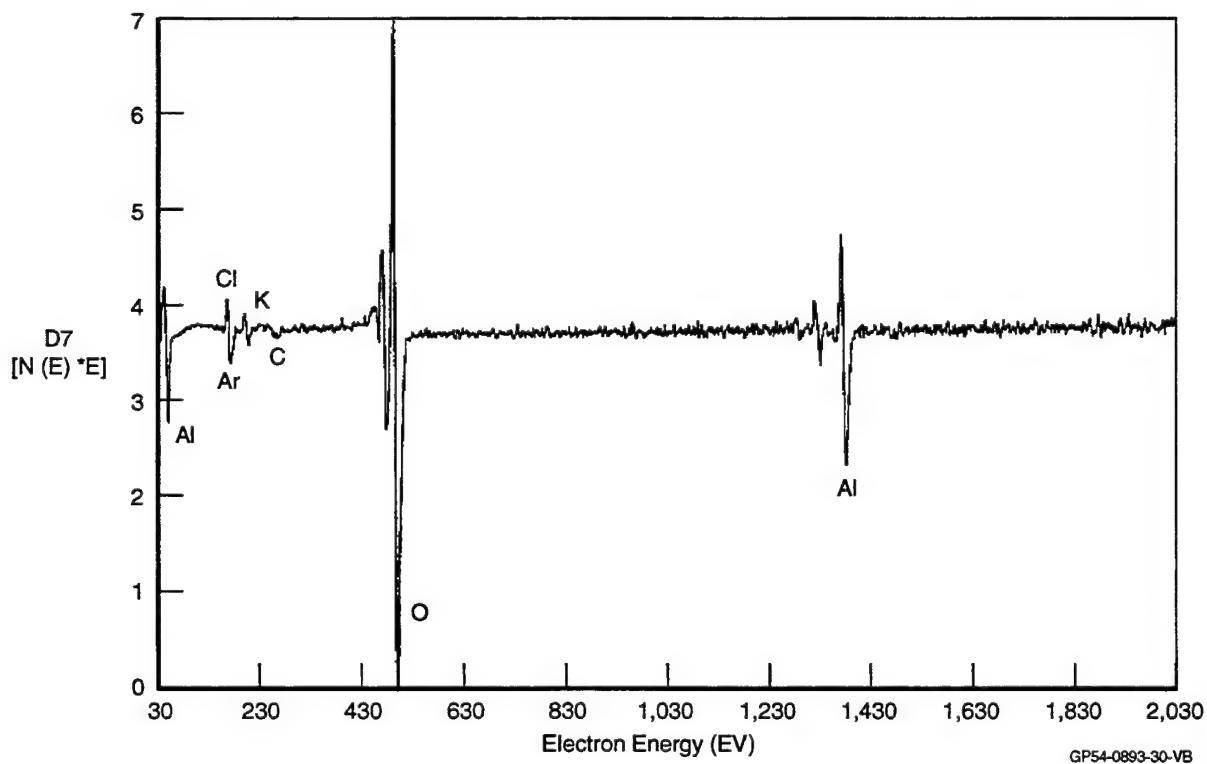
Figure 2.2.1-4. Auger Survey Spectrum for 5056-H39 Aluminum Alloy Exposed to Neutral Salt Environment for 594 hours (Slight Sputter).

13

These results indicate that the bulk of the corrosion products are in the form of Al_2O_3. This would lend itself to detection using an aluminum NMR technique, taking advantage of the Knight shift phenomenon. If the corrosion product is hydrated (i.e., in the form of $Al(OH)_3$), the hydrogen NMR technique becomes a strong candidate due to increased sensitivity. However, it should be noted that the Auger technique cannot detect hydrogen. This severely limits the effectiveness of Auger microscopy relative to correlation of elemental contributions with NMR signals. Both aluminum and hydrogen NMR techniques will be presented in more detail in Section 2.3.1.

2.2.2 Characterization of Corrosion Layer Thickness

Auger electron spectroscopy was used to examine the near-surface regions of 2024-T3, 5056-H39 and 7075-T6 aluminum corrosion sensitivity specimens to determine the thickness of the surface corrosion layers. Depth profiles of the Al and O concentrations were obtained from several randomly chosen rectangular regions on each specimen. Each of these regions covered an area of 0.04 mm^2. Plots of atomic concentration (at. %) as functions of depth, such as the ones shown in Figure 2.2.2-1 for the 2024-T3 alloy, were used to quantify the thicknesses of the surface oxide layers. Both the "down-turn" times and "cross-over" times were noted. The down-turn time represents the SiO_2 sputter time associated with a decreasing oxygen/aluminum concentration ratio. The cross-over time represents the SiO_2 sputter time associated with equivalent oxygen and aluminum concentrations. The thickness of the corrosion layer was obtained by multiplying the sputter time with the sputter rate and averaging the thicknesses measured across the surface (typically three to four measurements). The two data sets shown in Figure 2.2.2-1 correspond to 65.5 and 336 hour exposures in an SO_2 environment. The Auger spectroscopy results from each aluminum alloy system are summarized below:

14
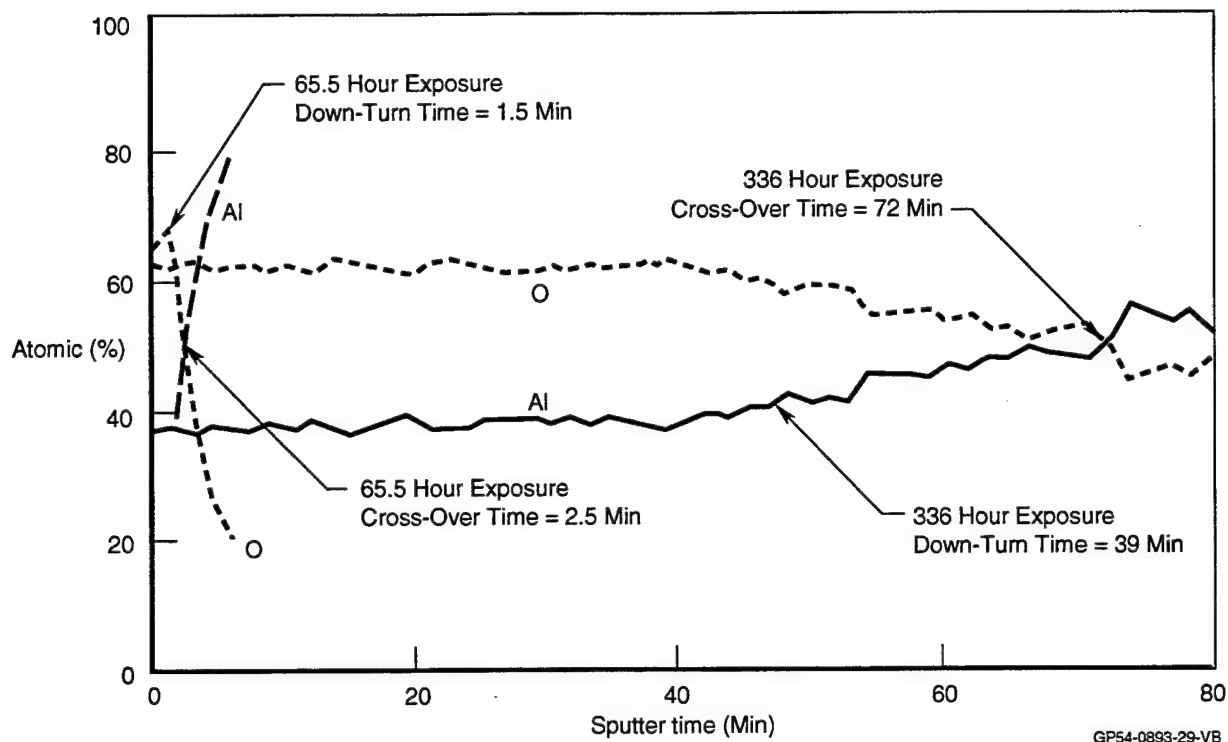
Figure 2.2.2-1. Aluminum-Oxygen Depth Profiles Collected on 2024-T3 Aluminum Specimens Exposed in SO$_2$ Environment for 65.5 and 336 hours, Respectively.

- <u>2024-T3 Aluminum</u>: The 2024 specimens were exposed in an SO_2 environment for times ranging from 36 to 336 hours. Secondary electron images of the surfaces revealed that they were quite inhomogeneous and contained many pits. The measured sputter rate of SiO_2 for these experimental conditions was approximately 48 nm/min. The calculated thickness data for the 2024 alloy are presented in Figure 2.2.2-2 as a function of exposure time. The cross-over time was used for correlation as there was too much specimen charging due to the thick oxide layer to identify the down-turn time. The data revealed a correlation between exposure time and oxide layer thickness with the rate of oxide layer growth also increasing with exposure time.

GP54-0893-78-VB
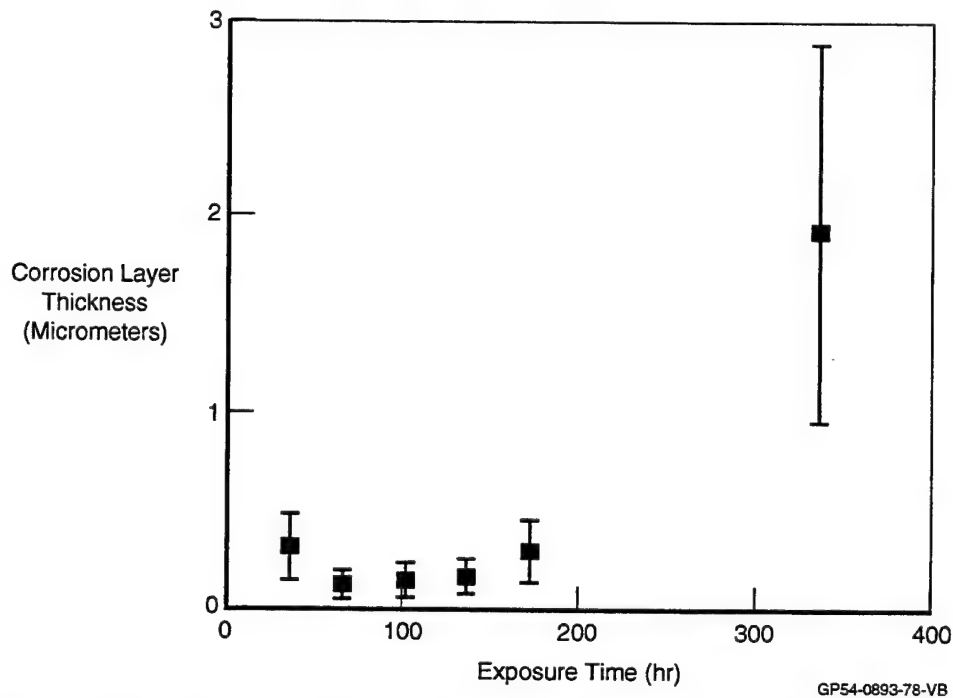
Figure 2.2.2-2. Corrosion Layer Thickness vs. SO_2 Exposure for 2024-T3 Aluminum Corrosion Sensitivity Specimens.

16

- 7075-T6 Aluminum: The 7075 specimens were exposed to an SO_2 environment for times ranging from 12 to 96 hours. Secondary electron images of these surfaces revealed that they were somewhat inhomogeneous and contained very few pits. In some cases, there were rather large regions of differing contrast levels in these images, presumably because of some compositional and/or thickness differences across the exposed surfaces. The measured sputter rate of SiO_2 for these experimental conditions was 40 nm/min. The calculated thickness data for the 7075 alloy are presented in Figure 2.2.2-3 as a function of exposure time. The down-turn time was used for correlation with the exposure times. The results showed that a general increase in corrosion layer thickness was noted as a function of exposure time. The specimen exposed for 31 hours had an unusually long sputter time, which corresponded to an unusually thick surface oxide layer. This data point is not shown due to the extreme corrosion layer thickness in comparison with the other specimens. It was believed that some surface contamination prior to or during exposure led to accelerated oxide layer growth.
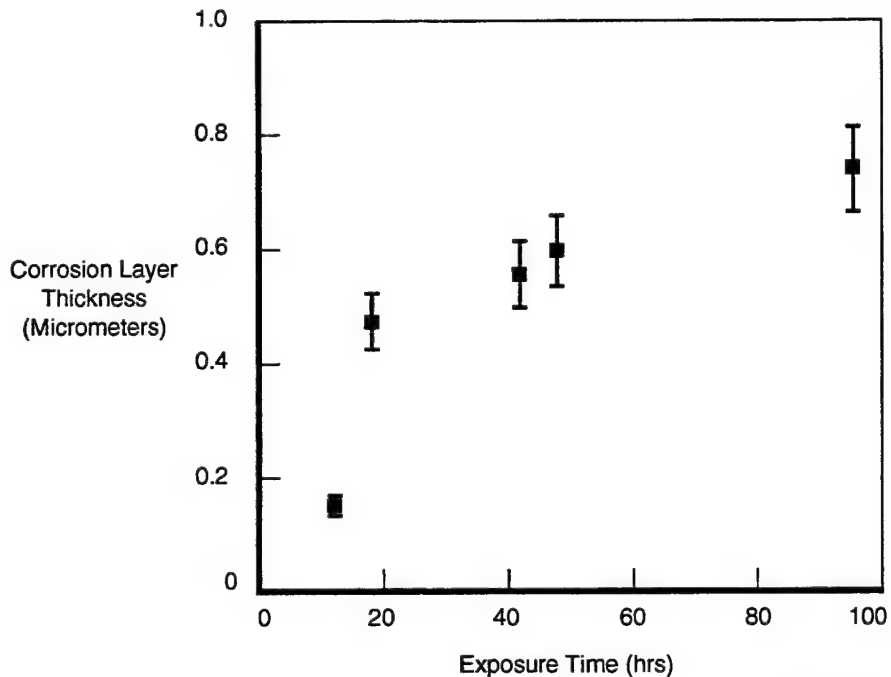
GP54-0893-43-VB

Figure 2.2.2-3. Corrosion Layer Thickness vs. SO_2 Exposure for 7075-T6 Aluminum Corrosion Sensitivity Specimens.

- 5056-H39 Aluminum: The 5056 specimens were exposed to a neutral salt environment for times ranging from 106 to 1056 hours. Secondary electron images of the 5056 specimens revealed that their surfaces were somewhat inhomogeneous and contained very few pits. The measured sputter rate of SiO_2 for these experimental conditions was approximately 62 nm/min. The calculated thickness data for the 5056 alloy are presented in Figure 2.2.2-4 as a function of exposure time. The down-turn time was used for correlation with the exposure times for the 5056 alloy. With the exception of the specimens exposed for 318 hours and 528 hours, these data reveal a systematic increase in the thickness of the corrosion layer as a function of exposure time. The only explanation for the higher than expected thickness layer for the specimen exposed for 318 hours is that only a few depth profiles taken across an inhomogeneous surface layer are not enough to accurately characterize a surface layer thickness. For the specimen exposed for 528 hours, AES survey spectra indicated that this was the only specimen with silicon on its surface. Furthermore, this specimen had a higher surface concentration of nitrogen and a lower surface concentration of aluminum than other specimens in the 5056 alloy category. It is speculated that the surface concentration of silicon limited the growth of corrosion, leaving a much thinner than expected corrosion layer.

GP54-0893-37-VB
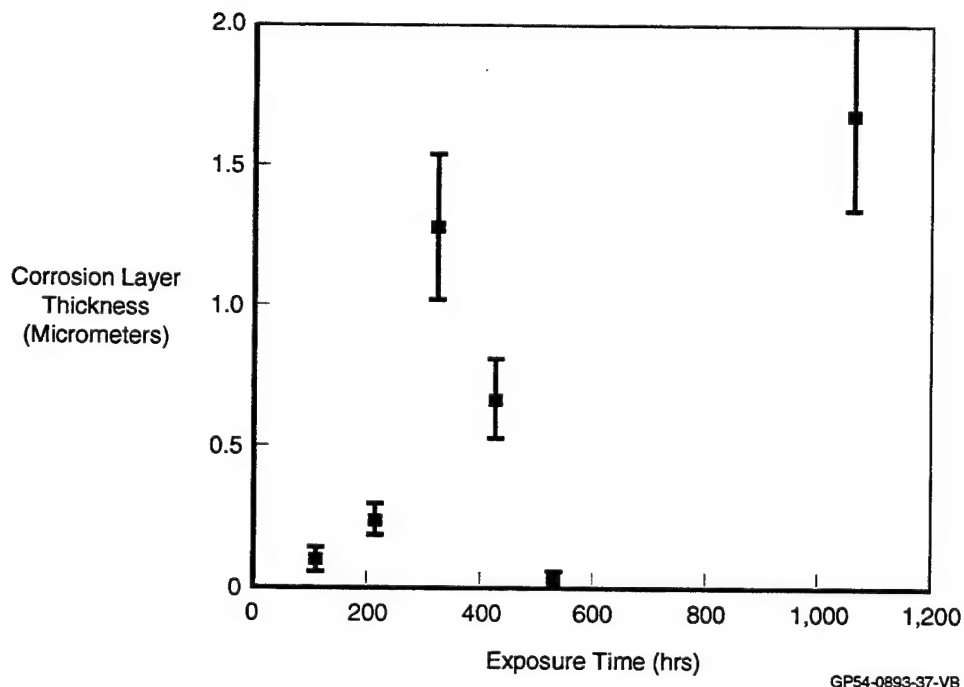
Figure 2.2.2-4. Corrosion Layer Thickness vs. SO_2 Exposure for 5056-H39 Aluminum Corrosion Sensitivity Specimens.

2.3 NMR Measurements

2.3.1 Background

Quantum Viewpoint: Nuclear magnetic resonance is a spectroscopic technique that examines transitions between magnetically separated nuclear spin energy levels [2]. Because most nuclei have a magnetic moment, usually denoted as a vector, μ, their preferred orientation is to lie parallel to an applied magnetic field. The interaction of the nuclear magnetic moment with the external field leads to an energy of the magnetic moment given by:

$$E = \vec{\mu} \cdot \vec{H}_0 \qquad (1)$$

In addition, the direction of the nuclear magnetic moments are quantized. This means that the nuclei can be oriented in a number of discrete directions, the number depending on the "spin number" of the nucleus, usually denoted I (I=0, 1/2, 1, 3/2,...): it turns out that the number of possible orientations of the magnetic moment is just 2I+1.

The magnetic moment of the nuclei mentioned above, μ, is dependent only on three things: (1) the nuclear spin number of the nucleus; (2) Planck's constant; and (3) the gyromagnetic ratio of the nucleus γ:

$$\vec{\mu} = \gamma \hbar \vec{I} \qquad (2)$$

Because I is quantized, the energy levels are also quantized. NMR examines the spectroscopic transitions between these discrete energy levels:

$$E_z = -\gamma \hbar H_0 m, \quad m = -I, \ -I + 1,..., \ I{-}1, \ I \qquad (3)$$

Because of selection rules, NMR involves transitions from one energy level to the one above or below ($\Delta m=1$). As a result, the energies absorbed or released in an NMR experiment is given by:

$$\Delta E = \gamma \hbar H_0 \qquad (4)$$

Thus, the frequency of energy absorbed or emitted, the Larmor frequency, is:

$$\omega_L = \Delta \frac{E}{\hbar} = \gamma H_0 \qquad (5)$$

Therefore, in the quantum viewpoint, the resonance absorption frequency is determined by the spacing between the spin energy levels.

The Larmor frequencies of several nuclei at a field strength of 7.0 Tesla, for example, are presented in Figure 2.3.1-1. Nucleus abundance is simply the fraction of the referenced isotope relative to the total number of nuclei. If the nucleus is in a metal, polarization of the conduction electrons will lead to an additional magnetic field seen by the nucleus in a conducting environment and the nucleus in a dielectric environment is called the Knight shift. An example of this phenomenon is shown in Figure 2.3.1-2 for a corroded aluminum alloy measured in a 7.0 Tesla magnetic field using an aluminum NMR technique. The corrosion peak was identified 128 kHz downrange from the aluminum metal peak. This 128 kHz shift in the frequency domain is the Knight shift. The magnitude of this shift is dependent on the external magnetic field strength.

Nucleus	Frequency (MHz)	Abundance (%)	Spin
^{1}H	300	100	1/2
^{13}C	75.4	1.1	1/2
^{23}Na	79.3	100	3/2
^{27}Al	78.2	100	5/2
^{29}Si	59.6	4.7	1/2
^{31}P	121	100	1/2
^{53}Cr	17.0	9.6	3/2
^{59}Co	70.8	100	7/2
^{55}Mn	74.0	100	5/2
^{57}Fe	9.7	2.2	1/2
^{63}Cu	79.5	69	3/2
^{93}Nb	73.3	100	9/2
^{119}Sn	112	8.6	1/2
^{183}W	12.5	14	1/2
^{195}Pt	64.5	34	1/2
^{199}Hg	53.5	17	1/2
^{207}Pb	62.8	23	1/2

GP44-0435-15-V

Figure 2.3.1-1. Larmor Frequencies for Selected Nuclei at a Magnetic Field Strength of 7.0 Tesla.
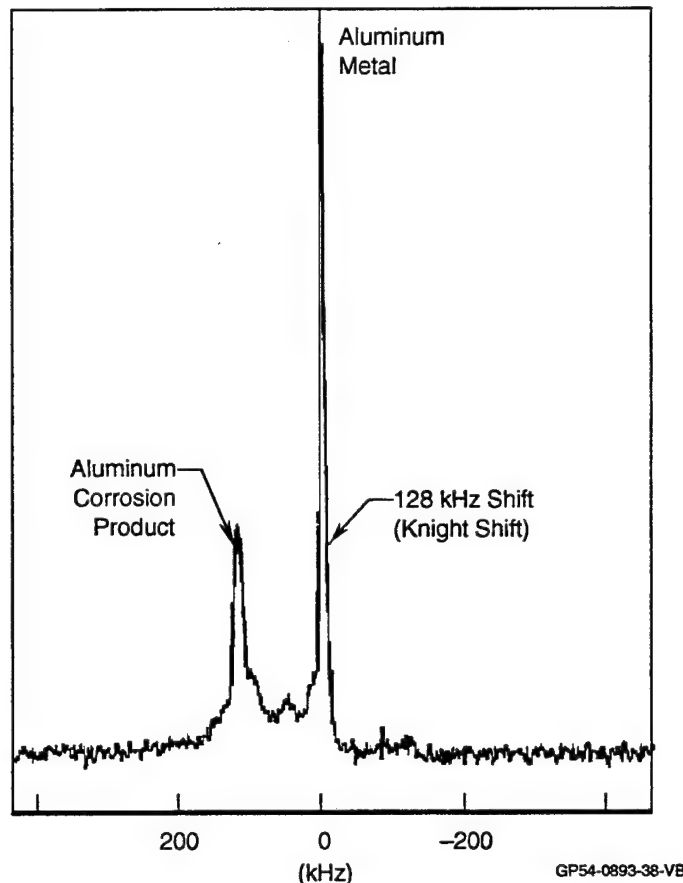
Figure 2.3.1-2. Aluminum NMR Signal From Corroded 5056-H39 Aluminum Alloy Measured at 7.0 Tesla (78 MHz) Exhibiting the Knight Shift Phenomenon.

Hydrogen, the nucleus most often examined using NMR, has a spin number of 1/2 and has two possible orientations (m=+/-1/2): parallel to the field ("up") and anti-parallel to the field ("down"). Aluminum, spin 5/2, has six possible orientations: m=5/2, 3/2, 1/2, -1/2, -3/2, -5/2.

If all of the spin states were equally populated, stimulated absorption and stimulated emission would be equal, leading to no net resonant absorption and no detectable signal. Thus, the net absorption is due to the slightly (of order one part per million) larger population in the lower energy spin states (parallel to H_o) than in the higher energy states anti-parallel to the static field

Classical Viewpoint: Although there are almost equal numbers of nuclei aligned with the field as there are against the field, the slight inequality leads to a net number of nuclei aligned parallel to the field. This net nuclear magnetization is the source of all NMR signals. Because the nuclear magnetization is comprised of a macroscopic number of nuclei (typically on the order of 10^{18} per gram of sample), the net

nuclear moment behaves as if it were a classical object and not quantized. As a result, it functions like a classical bar magnet: it can assume any orientation in space, not just the few possible quantized orientations [2].

If the magnetization is no longer oriented parallel to the external magnetic field, then the field will produce a torque on the magnetization. This torque will cause the magnetization to precess around the field at the Larmor frequency. It is noteworthy that the frequency of classical precession corresponds exactly to the spacing between the quantum energy levels (eq.5). Thus, the quantum and classical viewpoints yield the same frequency. A precessing moment placed inside a coil will induce an ac voltage across the coil with a frequency equal to the precession frequency.

Often, a rotating frame of reference is used in order to visualize the precession of the magnetization vector. The coordinates and vectors in this frame are usually denoted by primes. The Z' coordinate, which is the direction of the static magnetic field, is the axis of rotation and is chosen to be parallel to the Z coordinate in the lab frame. The reference frame rotates with a frequency equal to that of the applied RF field, which is generally at or near the Larmor frequency. As a result, the precessing magnetization appears nearly stationary in the reference frame. Because of the change in coordinate systems from lab to rotating, the external magnetic field is replaced by:

$$\vec{H}_0' = \vec{H}_0 - \frac{\vec{\Omega}}{\gamma}$$

(6)

where H_o' is the effective static field in the rotating frame, H_o is the static field in the lab frame, Ω is the frequency of the rotating frame, and g is the gyromagnetic ratio, as before. As a result, a frame of reference rotating at the Larmor frequency has no static magnetic field.

In a rotating reference frame, a circularly polarized magnetic field oscillating (rotating) at the Larmor frequency appears to be a stationary magnetic field because it rotates with the reference frame. As a result, in the rotating frame, the nuclear magnetization will precess (nutate) around this (static) radio frequency (RF) field with a frequency w_1 determined by the RF magnetic field strength, H_1:

$$\omega_1 = \gamma H_1$$

(7)

The angle that the magnetization nutates is equal to $\omega_1\tau$, where τ is the time duration of the RF magnetic field. As a result, pulses of RF field are usually referred to in a shorthand that states their nutation angle and the axis of the rotating frame along which they were directed. For example, a 90_x is a $90°$ pulse applied along the x' axis of the rotating frame. Once the magnetization has precessed into the X'Y' plane of the rotating reference frame, it is also in the XY plane of the lab frame, as represented in Figure 2.3.1-3. After the RF is turned off, the magnetization precesses about the static magnetic field and induces a signal in the probe coil. If the pulse angle is $180°$, then the nuclear magnetization is inverted and lies anti-parallel to the static external field. This is referred to as an inversion of the spin system.

Relaxation: If the magnetization's equilibrium orientation is parallel to the Z(Z') axis, then while it is precessing in the XY plane, it is in a nonequilibrium state. To re-establish equilibrium, two things need to happen: (1) the in-plane magnetization (perpendicular to the static field) must decay to zero and (2) the magnetization parallel to the static field must grow to its equilibrium value.

The time for the in-plane magnetization to decay is T_2, the transverse or spin-spin relaxation constant. The value of T_2 can be determined by acquiring the signal collected after a pulse. Because the signal is proportional to the magnitude of the magnetization vector precessing about the static field, the signal decays in a time determined by T_2. As a result, T_2 is defined to be the time required for the signal to decay to $1/e$ of its initial value. The signal is known as a free induction decay, or FID; so named because the spins are free, and not driven since $H_1=0$, they induce a voltage in the coil, and the signal decays. The FID can be Fourier transformed to give the spectral distribution of nuclei in the sample. The linewidth of the spectrum is $1/T_2$.

Besides T_2 relaxation, the magnetization will recover along the static magnetic field. The decay time is known as the longitudinal or spin-lattice relaxation time, T_1. T_1 processes change the Z-magnetization (the magnetization vector's component parallel to the external field) and thus change the spin system's energy, $E=-M_zH_o$. The energy must be exchanged with the rest of the sample ("the lattice," whether the sample is solid or not). These T_1 processes require that there be some physical motion in the sample with frequency components at the Larmor frequency. As a result, the spin-lattice relaxation rate T_1^{-1} is a measure of the extent of motion in the sample at the Larmor frequency. In a metal, it is the motions of the conduction electrons that typically relax the nuclei. Called Korringa relaxation, this phenomenon leads to short T_1 values.
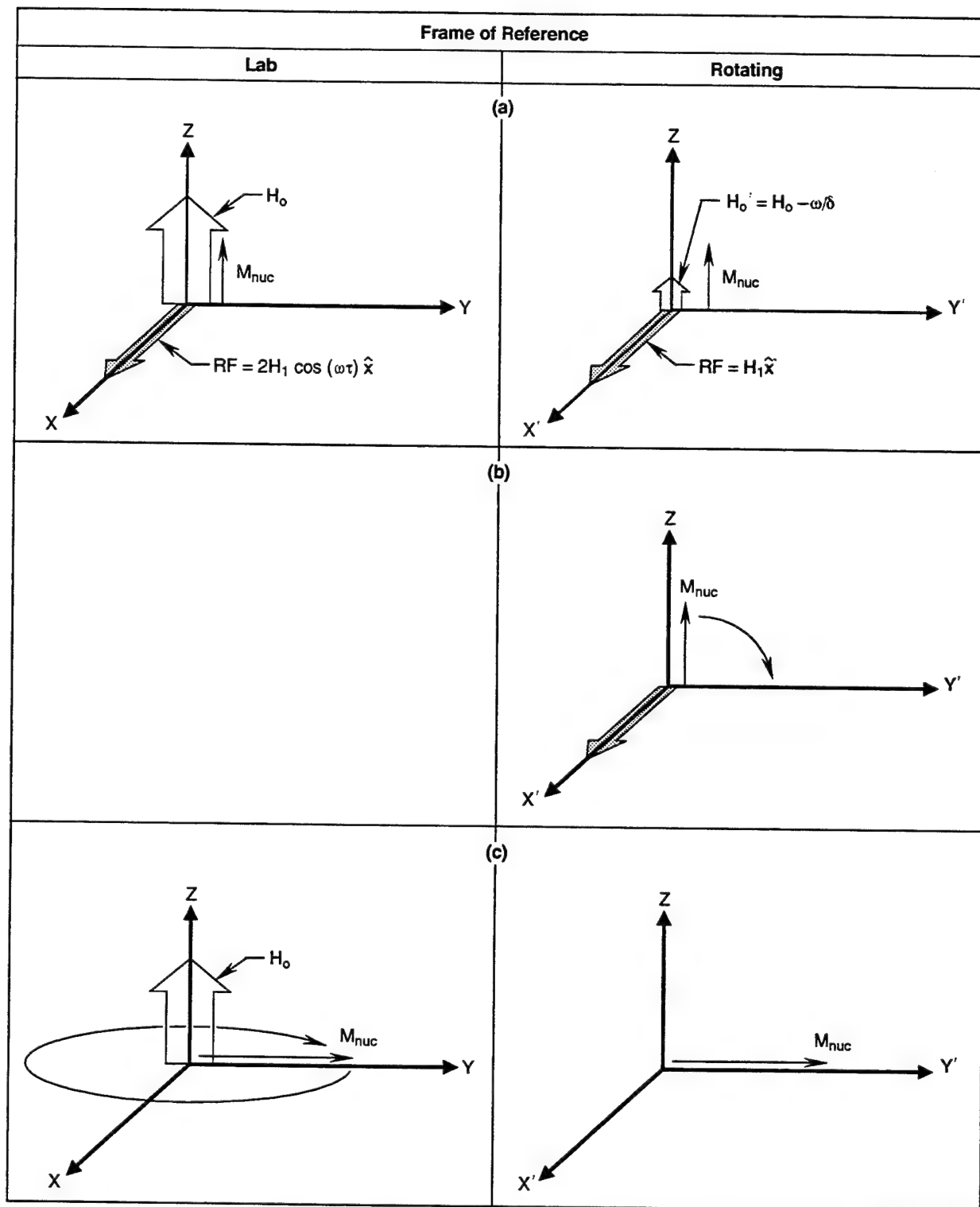
Figure 2.3.1-3. (a) The RF Oscillates Linearly in the Lab Frame But Is Static in the Rotating Frame (b) The Magnetization Processes Around the RF at the Rate $\omega_1 = \gamma H_1$. In a Time τ, the Magnetization Will Lie in the XY Plane. (c) Now the Magnetization Precesses Around the Static Magnetic Field, (H_o) in the Lab Frame: the Precessing Magnetic Field Generates a Voltage in the Coil Surrounding the Sample.

Materials may be differentiated on the basis of their spin-lattice relaxation times. A standard pulse sequence for this purpose is the saturate-wait-inspect sequence. A saturation pulse is a long RF pulse that causes the nuclear magnetization to become zero. During the waiting (or recovery) period, the nuclear magnetization begins to grow parallel to the external static field. A material with a shorter T_1 will have a larger nuclear magnetization vector at the end of a short (compared to T_1) waiting period. Finally, the inspection pulse generates an NMR signal proportional to the nuclear magnetization present just prior to the pulse. Because the nuclear magnetization of a material with a short T_1 will grow rapidly during the recovery period, signal from this material will dominate the total signal acquired.

Another method of differentiating materials on the basis of spin-lattice relaxation is to use the rapid repetition method. By rapidly repeating an NMR inspection pulse, the nuclear magnetization is able to recover parallel to the external field only during the time between the RF pulses.

A final method of discriminating between materials with differing T_1 values is to use an inversion-recovery method. The nuclear magnetization can be inverted with a 180° pulse, as mentioned previously. The nuclear magnetization then recovers parallel to the external field. If two materials are being compared, an inspection pulse can be applied when one of the materials' nuclear magnetization is passing through zero. At such time, this material will not contribute to the net signal.

In the absence of appreciable molecular motions in a solid sample, the value of T_2 remains constant at its rigid lattice limit. The linewidth then simply reflects the distribution of local fields present at the nuclei. Once the nuclei in the sample begin to move, the distribution of the magnetic fields inside the sample become motionally averaged; as a result, the linewidth decreases and T_2 increases.

As the motional frequency approaches the NMR frequency, ω_o, the spin-lattice relaxation time passes through a minimum. For the motion rate equal to the NMR frequency, the relaxation is most efficient. With the motion rate, ω_c, exceeding ω_o, T_1 is independent of the frequency ω_o. For $\omega_c < \omega_o$, T_1 varies as ω_o^2 [3].

Apparatus for NMR: The simplest NMR experiments to perform are continuous wave (CW NMR) experiments, illustrated in Figure 2.3.1-4. In this experiment, the sample is placed in a tuned (tank LC) circuit of a fixed frequency oscillator, at a frequency ω. The coil and sample are located in the external magnetic field H_o. The magnetic field is then swept through resonance ($H_o = \omega/\gamma$). As this occurs, the quality factor (Q) of the tank circuit changes as the nuclear spins in the sample absorb energy. This Q change is detected as a reduction in the RF voltage developed across the coil.
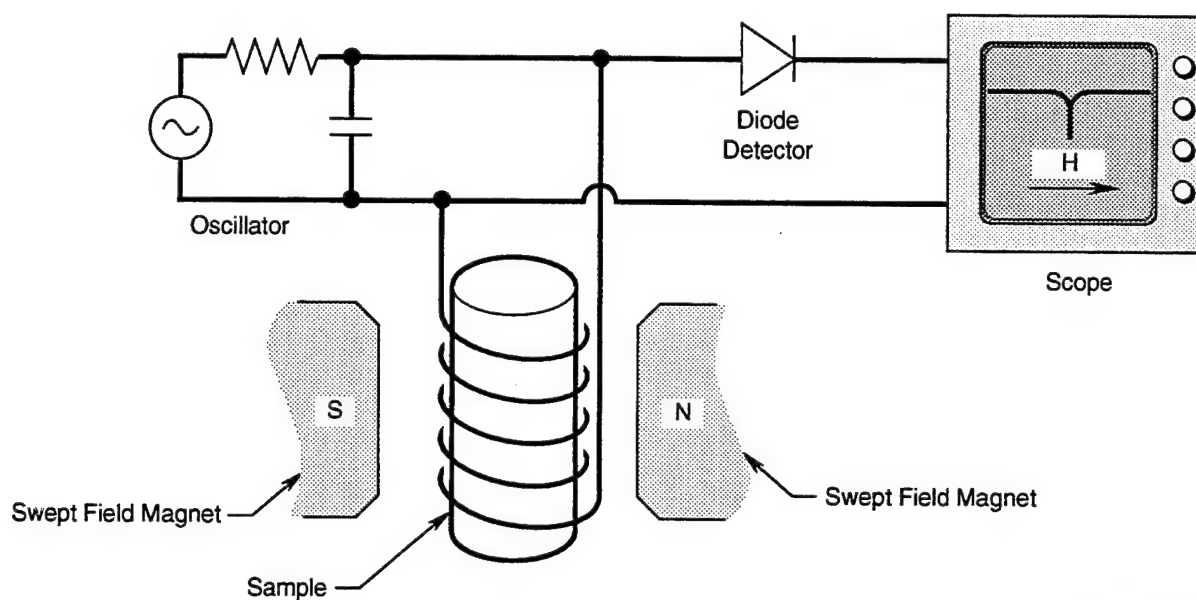
GP54-0893-40-VB

Figure 2.3.1-4. Simple Continuous Wave (Q-Meter) Spectrometer. As the Field, H, Is Swept Through the Spin Resonance, the Q of the Circuit Is Reduced by Resonant Absorption.

A pulsed NMR experiment typically consists of a pulsed RF transmitter to apply one or more RF pulses to a resonant high-Q probe in the magnet, shown in Figure 2.3.1-5, and a high sensitivity RF receiver [4]. After the pulses have been applied, the voltage induced by the precessing magnetization is amplified and then digitized for subsequent analysis. Because of the conjugate relationship between time and frequency, this time-based data can be Fourier transformed to give the frequency spectrum of the nuclei in the sample. This spectrum is the same as would be obtained from a CW experiment.
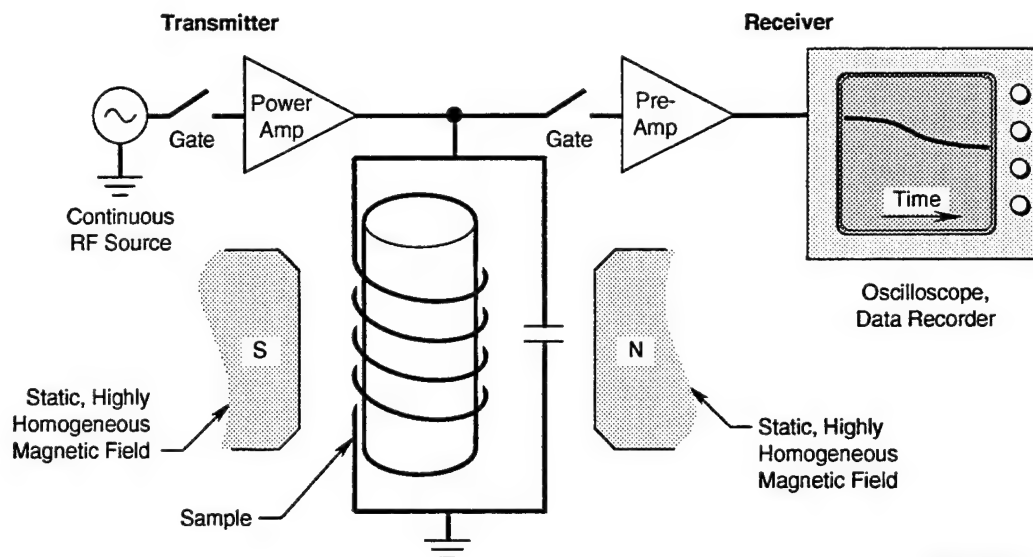
Figure 2.3.1-5. Schematic Representation of a Pulsed NMR Apparatus. Pulse Excitation of the Spins By the Transmitter Is Followed By a Free Induction Decay.

The equipment required for performing NMR measurements is basically the same regardless of the experiment. Figure 2.3.1-6 shows a block diagram of a pulsed NMR spectrometer [5]. The sample is placed either inside or underneath a coil, depending on the experimental configuration. Both coil and specimen are placed in a magnetic field. Connected to the probe is a duplexer that directs NMR pulses from the transmitter to the probe and away from the receiver. It then directs NMR signals from the probe to the receiver and away from the transmitter. Pulses are generated by a computer that gates a frequency synthesizer.
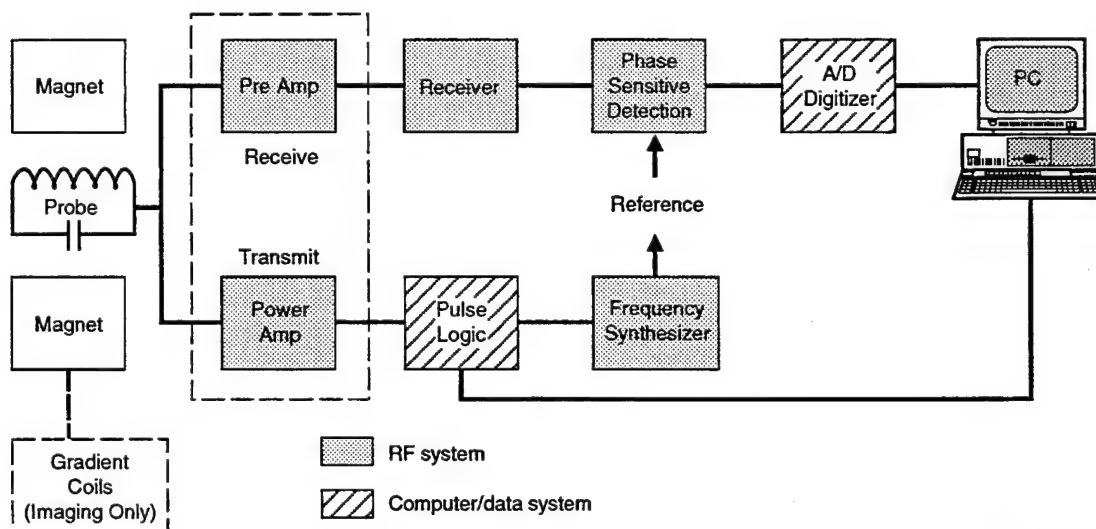
Figure 2.3.1-6. Block Diagram of Typical Experimental NMR System.

27

Effects of Magnetic Materials: It was originally intended in this program to evaluate the feasibility of using NMR to detect corrosion in high strength steels. The 300M steel chosen for evaluation was determined to be highly magnetic and, therefore, was not a candidate for NMR. The following is a description on why highly magnetic materials are impossible to evaluate using NMR.

When a magnetic material is placed in a homogeneous magnetic field, as shown in Figure 2.3.1-7, the magnetic field lines bend at the surface of the magnetic particle because of the superimposed magnetic field of the magnetic material [6]. As a result, the initially homogeneous magnetic field is now distorted (inhomogeneous) over the region of space containing the material and beyond. Since the precision frequency of a nuclear spin depends primarily on the magnetic field strength ($\omega = \gamma H_o$), the resulting distribution of magnetic fields over the volume of the material leads to a broadening of the NMR spectral line. Since the total area under the the NMR signal is proportional to the number of nuclei examined (and, therefore, constant), the amplitude of the signal diminishes dramatically. The resulting broad width, low intensity NMR line is difficult to detect either by continuous wave or pulsed NMR. The conclusion is that it is impractical to examine highly magnetic materials using NMR.
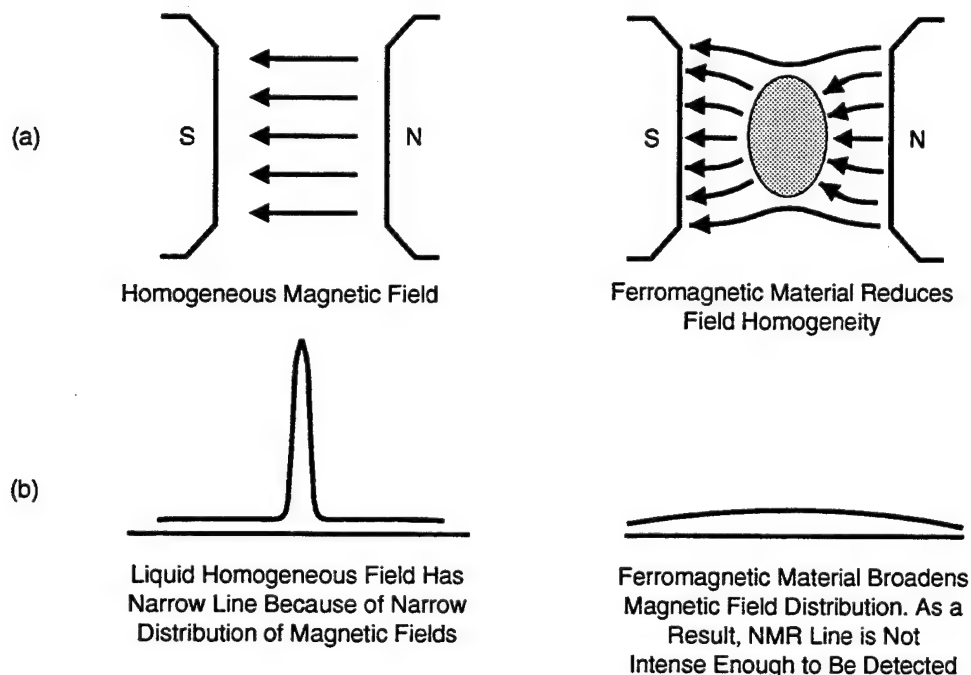
GP54-0893-79-VB

Figure 2.3.1-7. (a) Magnetic Material Placed in a Magnetic Field Adversely Affects the Static Magnetic Field Homogeneity. (b) As a Result, the NMR Signal Is Broadened and its Intensity Is Reduced Below the Noise Threshold.

2.3.2 Aluminum NMR Sensitivity Analysis

Aluminum NMR measurements were performed on the 2024-T3, 5056-H39 and 7075-T6 aluminum alloy corrosion sensitivity specimens using the 8.5 Tesla superconducting magnet shown in Figure 2.3.2-1. The sensitivity measurements were performed using an external magnetic field strength of 8.0 Tesla, which corresponds to a frequency of 89 MHz for aluminum-27 nuclei. The results of the aluminum NMR analysis are shown in Figures 2.3.2-2, 2.3.2-3 and 2.3.2-4 for the 2024-T3, 5056-H39 and 7075-T6 corrosion sensitivity specimens, respectively. The Knight shift, which was described in the previous subsection, allows for the discrimination of the corrosion signal from the metal signal. At the 8.0 Tesla field used for this analysis, a 299 kHz frequency shift between the aluminum-27 signals from the corrosion product and the metal was observed. The NMR data plotted in Figures 2.3.2-2 through 2.3.2-4 have been normalized using the metal signal acquired simultaneously with the corrosion signal. These data, referenced as corrosion/metal signal ratio, were plotted as functions of both exposure time and corrosion layer thickness.
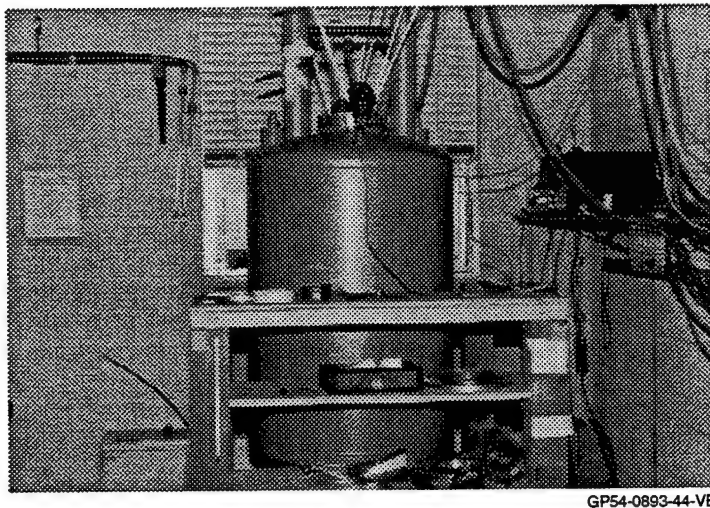
GP54-0893-44-VB

Figure 2.3.2-1. Superconducting Magnet (8.5 Tesla) Used for Aluminum NMR Measurements.

Figure 2.3.2-2. Aluminum NMR Corrosion Sensitivity Results for 2024-T3 Aluminum (8.0 Tesla/89 MHz).

Figure 2.3.2-3. Aluminum NMR Corrosion Sensitivity Results for 5056-H39 Aluminum (8.0 Tesla/89 MHz).

30

Figure 2.3.2-4. Aluminum NMR Corrosion Sensitivity Results for 7075-T6 Aluminum (8.0 Tesla/89 MHz).

For the three alloy systems evaluated, a general trend was identified: The aluminum NMR signal increased as functions of exposure time and, correspondingly, corrosion layer thickness. Two specimens, namely the 5056-H39 specimen exposed for 594 hours (neutral salt) and the 7075-T6 specimen exposed for 31 hours (SO_2), opposed this trend. The results obtained from these specimens, however, correlated well with the Auger depth profiling results documented in Section 2.2.2, where the abnormal behavior of these specimens was described. The correlation between NMR signal and corrosion layer thickness was not as consistent. It was determined that averaging several depth profile measurements over the surface of a specimen may not be the best way to characterize the surface. Since the NMR measurements evaluated each specimen as a whole, variations in data consistency are inevitable when trying to correlate these data with several spot surface measurements. This was especially so due to the inhomogeneity of the surface corrosion layers. Since the strength of the NMR signal is dependent on the amount of material present, better correlations may have been obtained using weight measurements instead. However, this exercise did demonstrate the superior sensitivity of the NMR technique compared to that of conventional radiographic inspection methods. The fact that small amounts of corrosion product were detected using NMR supports this claim.

The spin lattice relaxation time (T_1) of aluminum-27 in aluminum alloys is determined by the interaction of the aluminum nuclei with electrons in the conduction band of the metal (Korringa relaxation, which is also used to determine the Knight shift). Spin-lattice relaxations for the three alloy systems measured as a function of the fraction of optimum exposure time are presented in Figure 2.3.2-5. This figure shows the variation of the aluminum-27 spin-lattice relaxations from the Knight shifted position of the signal (metal component). Again, a general trend is immediately evident: Aluminum-27 spin lattice relaxations increase with increasing exposure time. It was also determined that the T_1 of the metal increases by up to 20% due to pitting and other minute surface flaws initiated during exposure. The increase in T_1 may reflect the large number of aluminum-27 nuclei that are in metallic regions influenced by nearby corrosion. Unfortunately, the increase in T_1 is not large enough to allow for reliable discrimination of corroded aluminum metal from pristine metal strictly on the basis of T_1 alone.
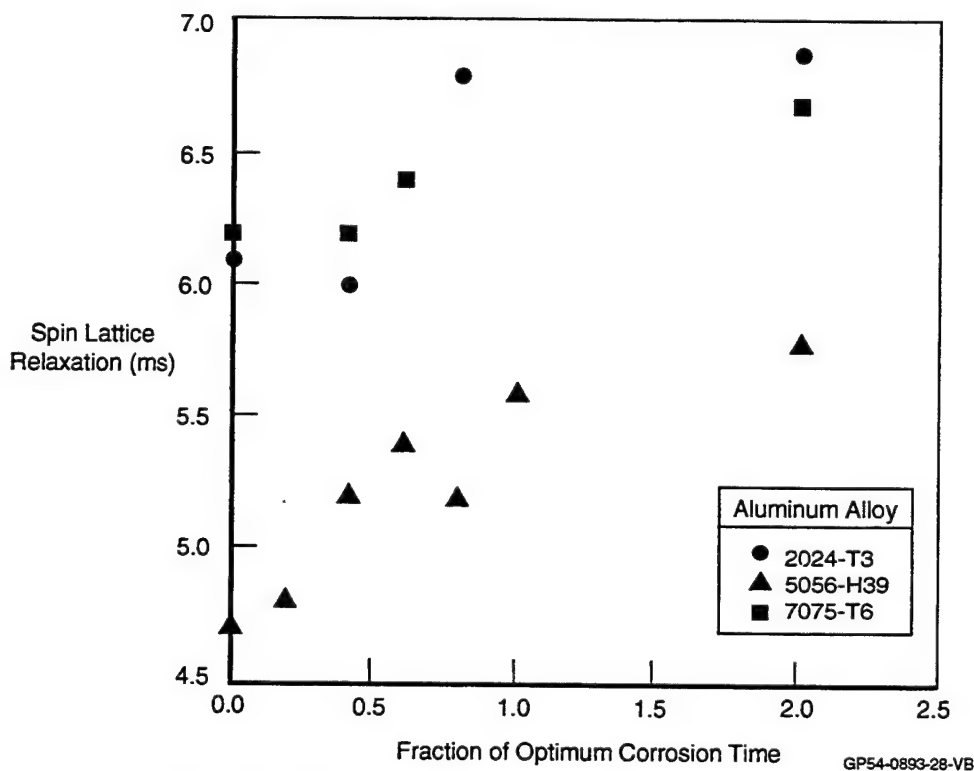
Figure 2.3.2-5. **Aluminum Spin-Lattice Relaxation vs. Fraction of Optimum Corrosion Exposure Time for 2024-T3, 5056-H39, and 7075-T6 Aluminum Alloys (8.0 Tesla/89 MHz).**

Although the aluminum NMR technique demonstrated improved sensitivity over conventional techniques, the question of practicality is another matter. The aluminum nucleus, unlike hydrogen, has an electric quadrupole moment. As a result, the width of the corrosion peak is determined by second order quadrupole broadening. It was expected that the width of the line will vary as ω_L^{-1} and increase at lower fields. Figure 2.3.2-6 shows measured and predicted behavior for the Knight shift and the $1/H_o$ variation of the corrosion line width. Because of this increasing line broadening, coupled with the decreasing difference between the two resonance lines, it will not be possible to distinguish between the metal and corrosion lines at a field below 1.0 Tesla on the basis of frequency shift. As a result, this line separation can not be used as an NDE technique assuming that low fields would be required for a practical inspection technique.
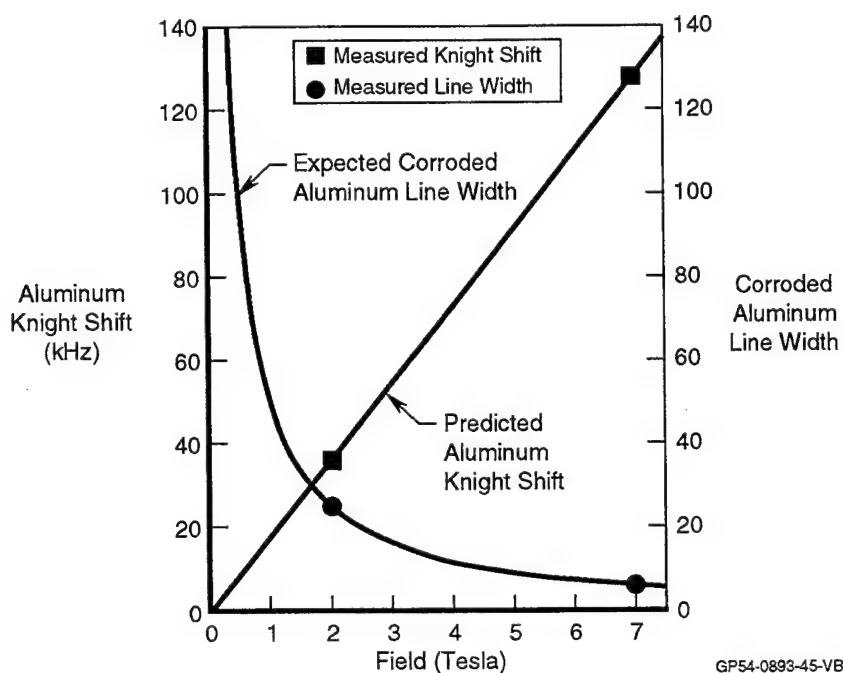
Figure 2.3.2-6. Frequency Shift and Corrosion Line Width Changes as a Function of Field Strength.

2.3.3 Hydrogen NMR Sensitivity Analysis

Hydrogen NMR measurements were performed on the 2024-T3, 5056-H39 and 7075-T6 aluminum alloy corrosion sensitivity specimens using the 2.0 Tesla electromagnet shown in Figure 2.3.3-1. The sensitivity measurements were performed using an external magnetic field strength of 2.0 Tesla, which corresponds to a frequency of 85 MHz for hydrogen nuclei. The results of the hydrogen NMR analysis are shown in Figures 2.3.3-2, 2.3.3-3 and 2.3.3-4 for the 2024-T3, 5056-H39 and 7075-T6 corrosion sensitivity specimens, respectively. In these data sets, the hydrogen NMR signal has been normalized by the signal intensity measured from 20 mg of corrosion product. Therefore, the hydrogen NMR signal intensity was reported in units of corrosion mass. The NMR data were plotted as functions of both exposure time and corrosion layer thickness.
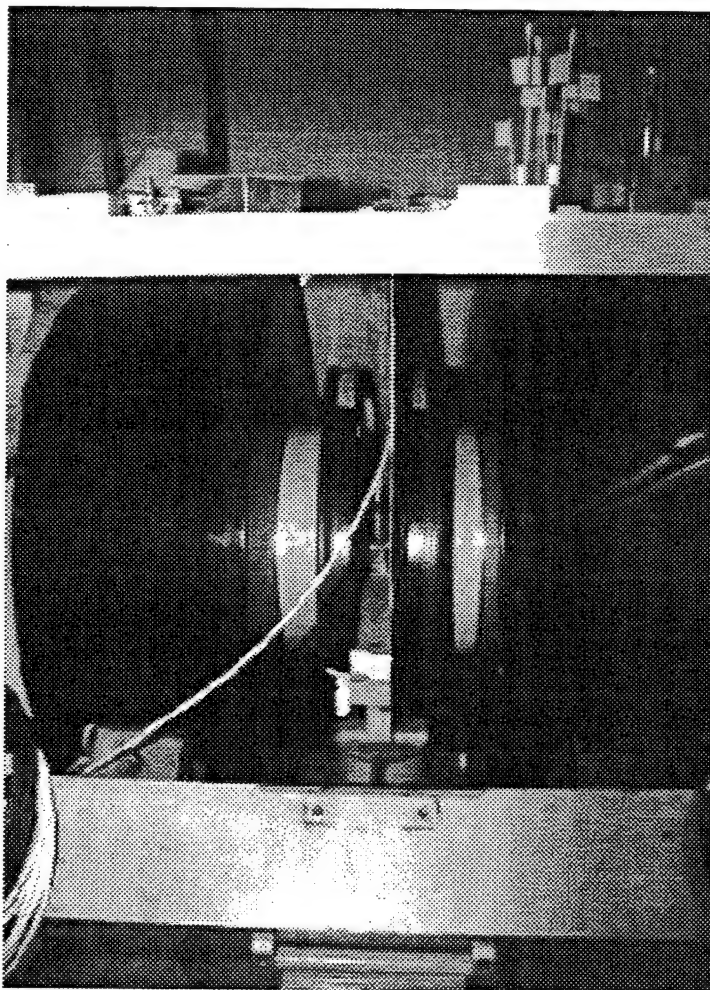
GP54-0893-46-VB

Figure 2.3.3-1. Electromagnet (2.0 Tesla) Used for Hydrogen NMR Measurements.
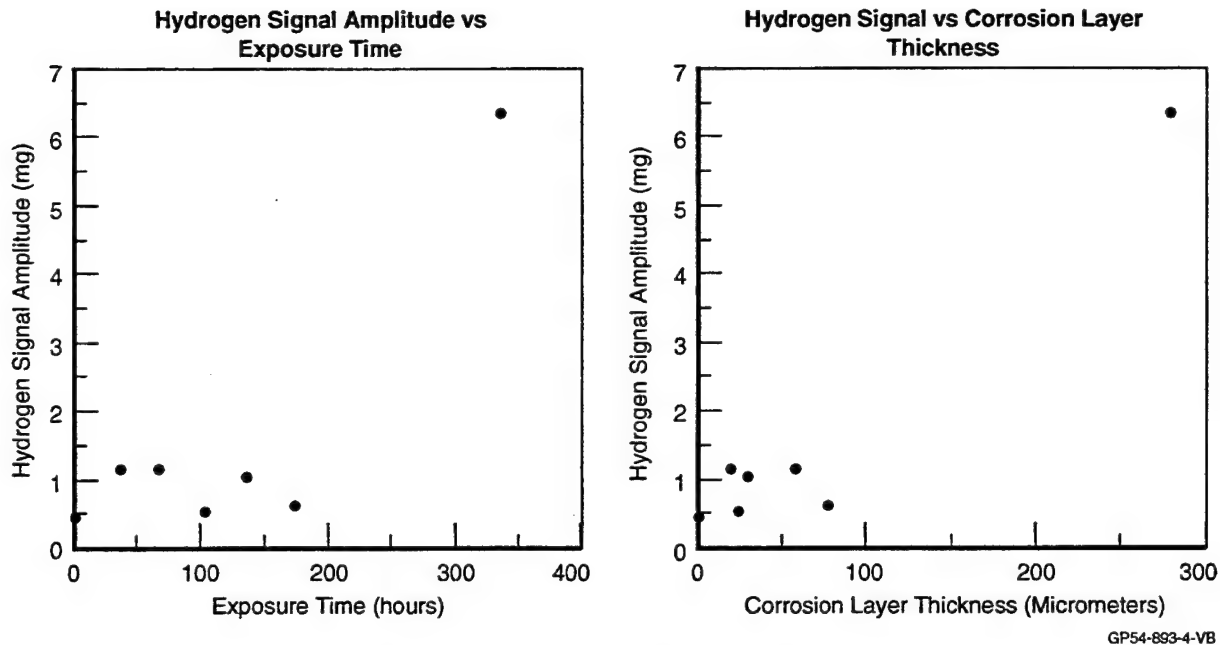
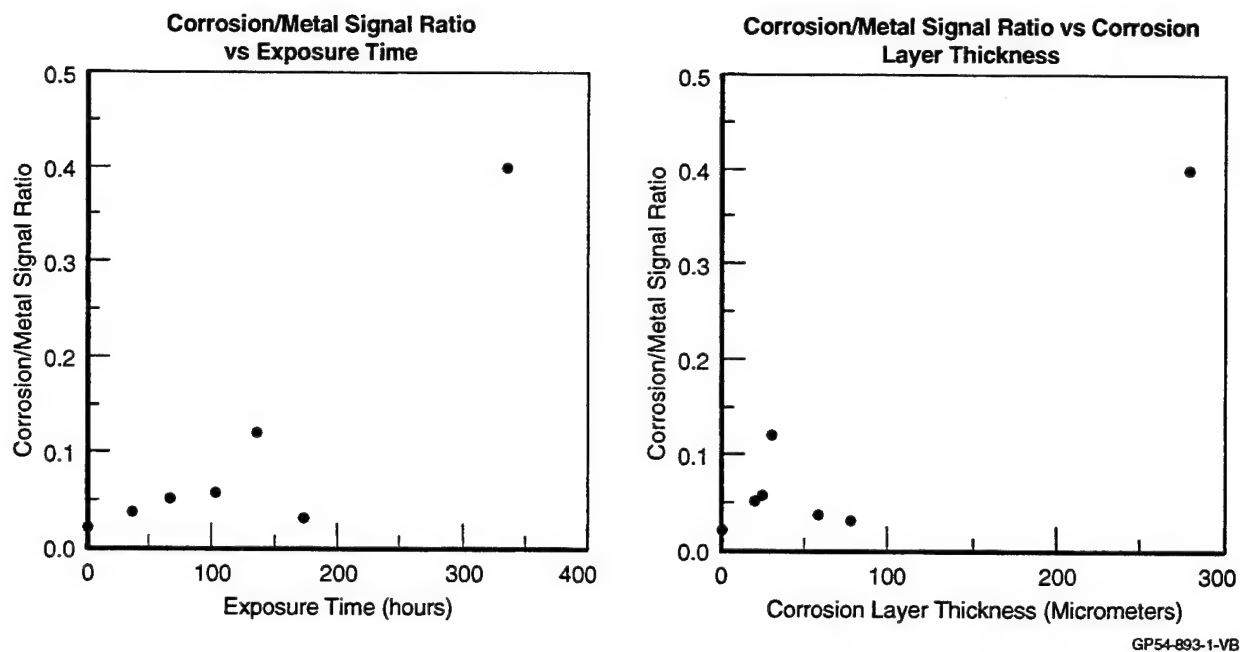**Figure 2.3.3-2. Hydrogen NMR Corrosion Sensitivity Results for 2024-T3 Aluminum (2.0 Tesla/85 MHz).**
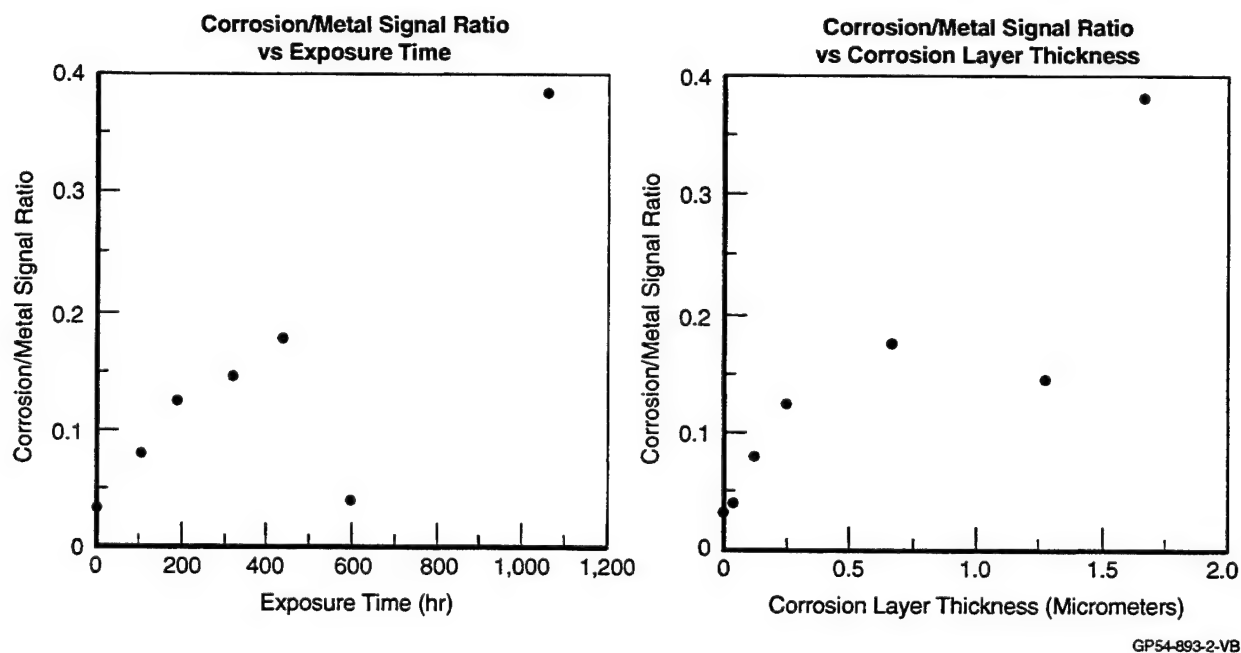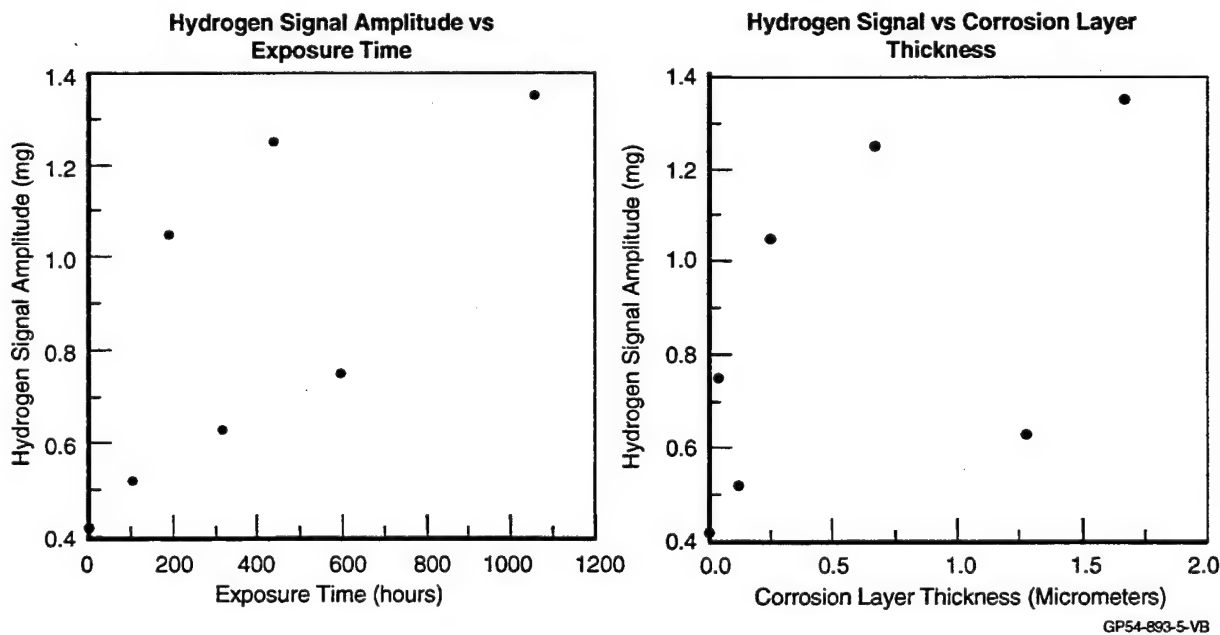

Figure 2.3.3-3. Hydrogen NMR Corrosion Sensitivity Results for 5056-H39 Aluminum (2.0 Tesla/85 MHz).
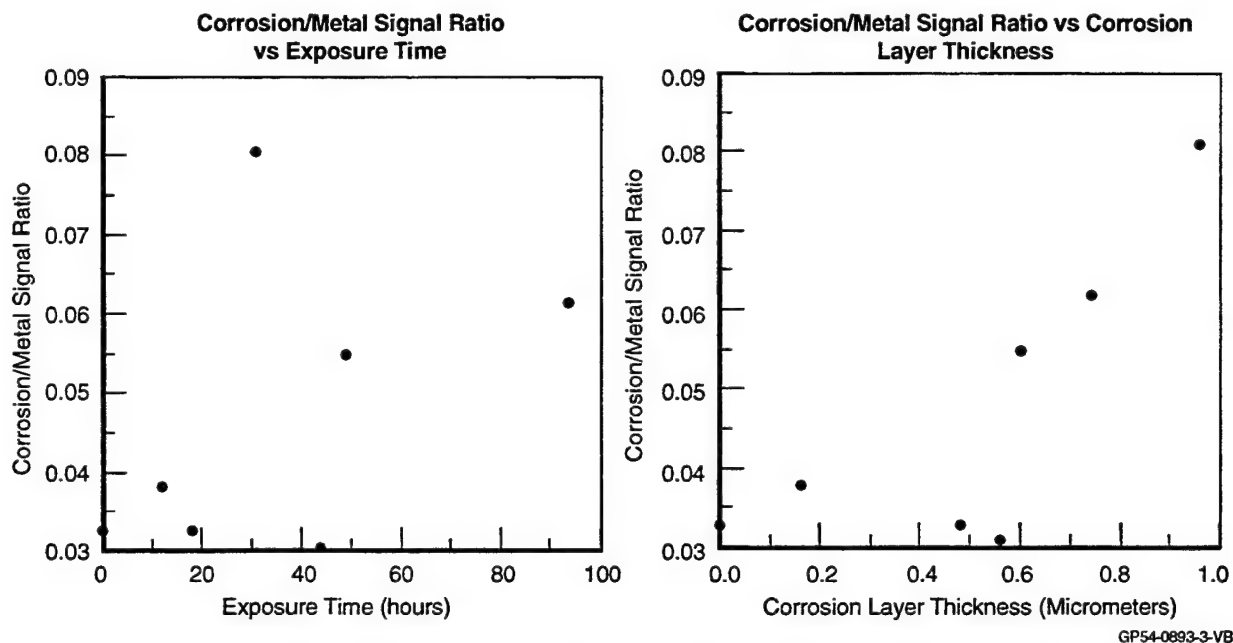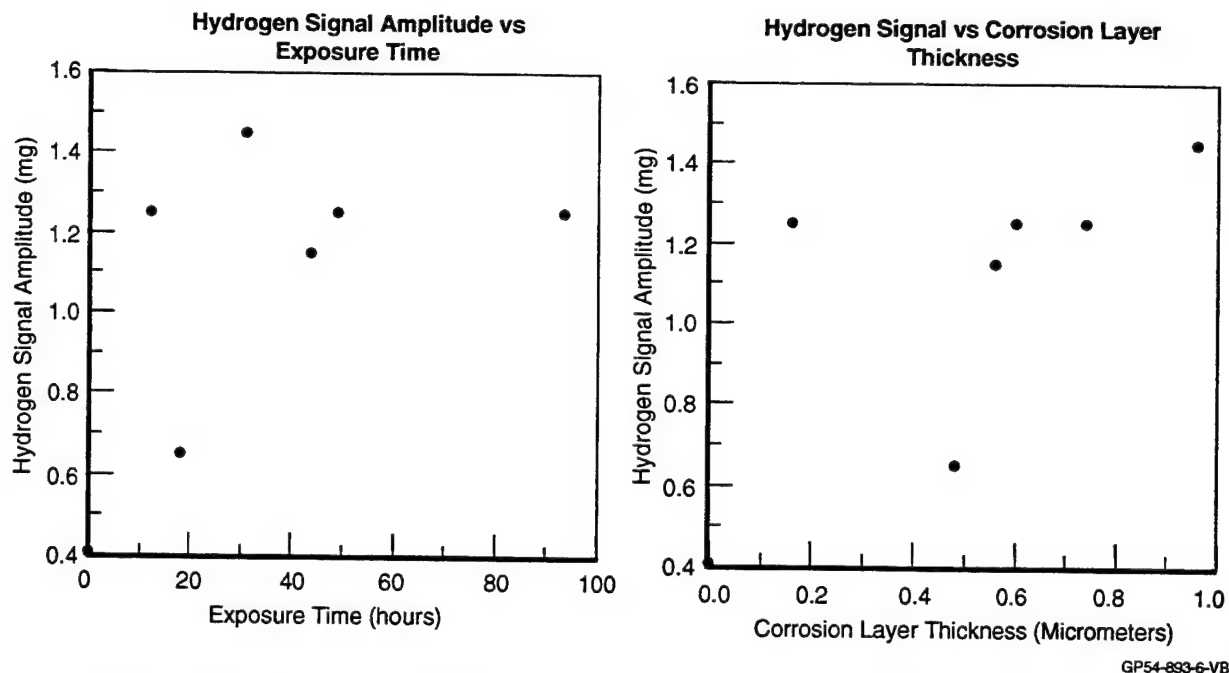
Figure 2.3.3-4. Hydrogen NMR Corrosion Sensitivity Results for 7075-T6 Aluminum (2.0 Tesla/85 MHz).

As was the case for the aluminum NMR results, the same general trend can be noted for the hydrogen NMR results: NMR signal increases with increasing exposure time. However, this trend is less evident for the hydrogen NMR results due to the fact that a two month interval between the aluminum and hydrogen NMR analyses existed. During this two month period, the sensitivity specimens continued to corrode at an undefined rate due simply to atmospheric exposure. As a result, the correlations between corrosion layer thickness and exposure became less noticeable. Consequently, the correlations between NMR signal and exposure/corrosion layer thickness became less definite. Nevertheless, the data did show that, much like the aluminum NMR technique, the hydrogen NMR signal intensity is strongly dependent on the amount of corrosion present on the surface. An advantage of the hydrogen technique is that equivalent sensitivities may be obtained at much lower magnetic field strengths. For the sensitivity evaluations, a factor of four drop in magnetic field strength was noted for the hydrogen technique. Based on the lower field potential of the hydrogen technique, all RF magnetic field penetration and corrosion detection work relative to simple structures were limited to the hydrogen NMR technique.

2.3.4 Hydration/Temperature Dependence

The spin-lattice relaxation time (T_1) of the nuclei in aluminum corrosion product is determined by the fluctuations of magnetic fields at or near the NMR frequency of the nucleus in question, as was discussed in Section 2.3.1. As a result, T_1 is typically temperature dependent. The value of T_1 is a minimum at a temperature corresponding to a maximum amount of internal molecular motion at the NMR frequency. Some significant fraction of the molecular motion in aluminum corrosion is likely to be due to waters of hydration. Increasing the relative hydration of the sample should, therefore, have a substantial effect upon the T_1 of the nuclei in the sample. In addition to a change in T_1, more molecular motion from additional waters of hydration or an increase in temperature will cause an increase in the spin-spin relaxation time, T_2.

In order to evaluate the effects of hydration and temperature on NMR signal behavior, bulk quantities of corrosion product were prepared. The corrosion product was created using a sheet of 6061 aluminum electrically connected to a brass ring. The aluminum/brass arrangement was placed in contact with saturated saline solution, which was then allowed to evaporate. Small quantities of this corrosion product were identified as either fully hydrated, bake dehydrated or flame dehydrated. Corrosion product removed from the surface of the aluminum sheet was designated as fully hydrated. The bake dehydrated specimen was heated in an evacuated chamber for 9 hours at 212°F. The flame dehydrated specimen was dehydrated rapidly (for less than two minutes) at a high temperature using a natural gas torch.

For the hydration study, hydrogen NMR measurements were performed using the 2.0 Tesla electromagnet. From the data shown in Figure 2.3.4-1, it is evident that the fully hydrated signal decays much more slowly than does the signal from the bake dehydrated corrosion product, implying a longer spin-spin relaxation (T_2) for the hydrated specimen. For the fully hydrated corrosion product, $T_2 = 110$ μs; for the bake dehydrated corrosion product $T_2 = 24$ μs.
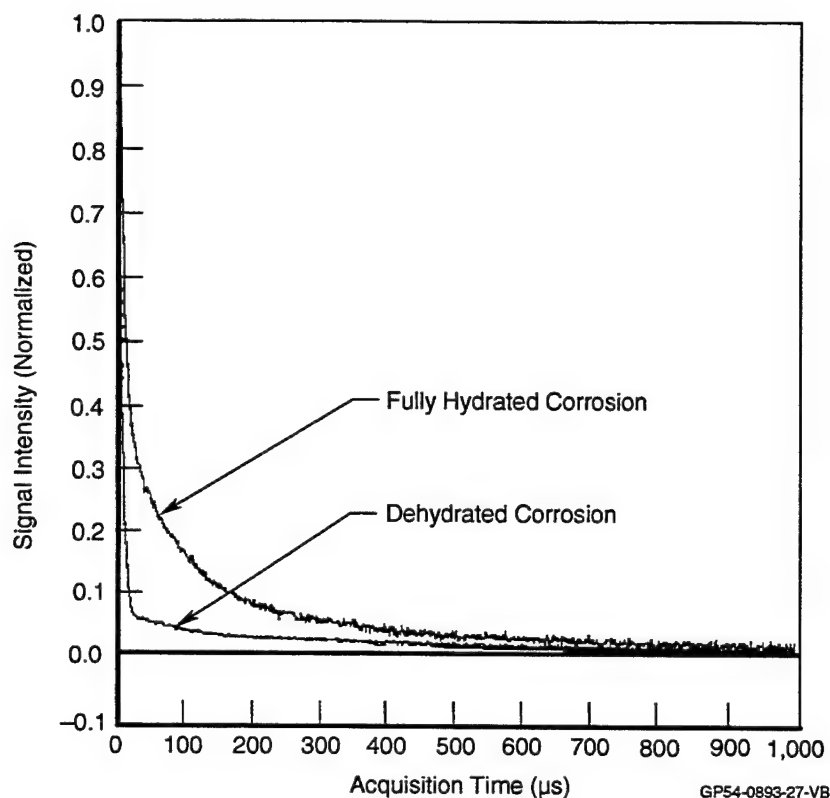
Figure 2.3.4-1. Comparison of Hydrogen NMR Signals From Both Hydrated and Dehydrated Corrosion Products. Note the Longer Lasting Signal From the Hydrated Corrosion Product. The NMR Signal of the Dehydrated Corrosion Also Has a Long-Lived Component (Remaining Signal After 30 μs); However, Most of the Signal From This Product Decays Rapidly.

For the variable temperature study, the spin-lattice relaxation time (T_1) was measured for both aluminum nuclei (8.5 Tesla/92 MHz) and for the hydrogen nuclei (2.0 Tesla/85 MHz). T_1 was measured over a temperature range of 100 K to 350 K. The temperature was regulated by monitoring the temperature of flowing nitrogen gas passing over the specimen. The aluminum NMR results are presented in Figure 2.3.4-2 for the hydrated and dehydrated cases. The data show that, regardless of the dehydration method, the spin-lattice relaxations are basically the same. The data also show that, for the hydrated specimen, T_1 is lower at room temperature (295 K) but higher at low temperatures (below 150 K). The hydrogen NMR results are shown in Figure 2.3.4-3 for specimens consisting of both states of hydration. The similarity between the aluminum and hydrogen NMR results indicate that both the aluminum and hydrogen nuclei are being exposed to the same fluctuating internal magnetic fields. In addition, both plots show a plateau (a T_1 minimum) near room temperature. The plateau indicates that over the temperature range likely to be encountered in operational environments (250 K to 350 K), T_1 of fully hydrated aluminum corrosion product will be nearly constant.
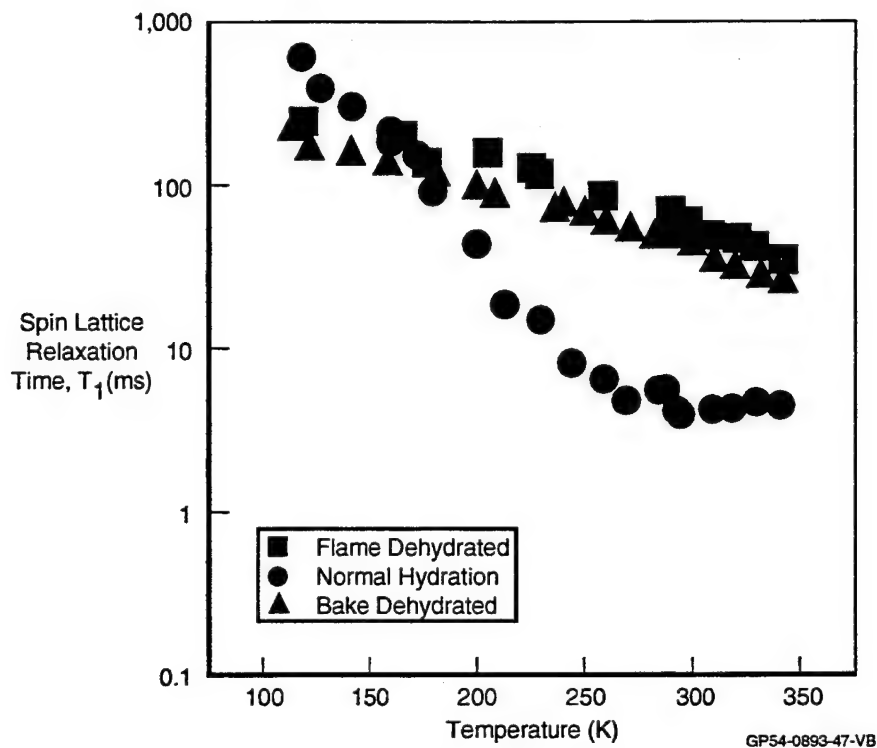
Figure 2.3.4-2. Aluminum NMR Evaluation of Hydrated and Dehydrated Corrosion Products as a Function of Temperature (8.5 Tesla/92 MHz).
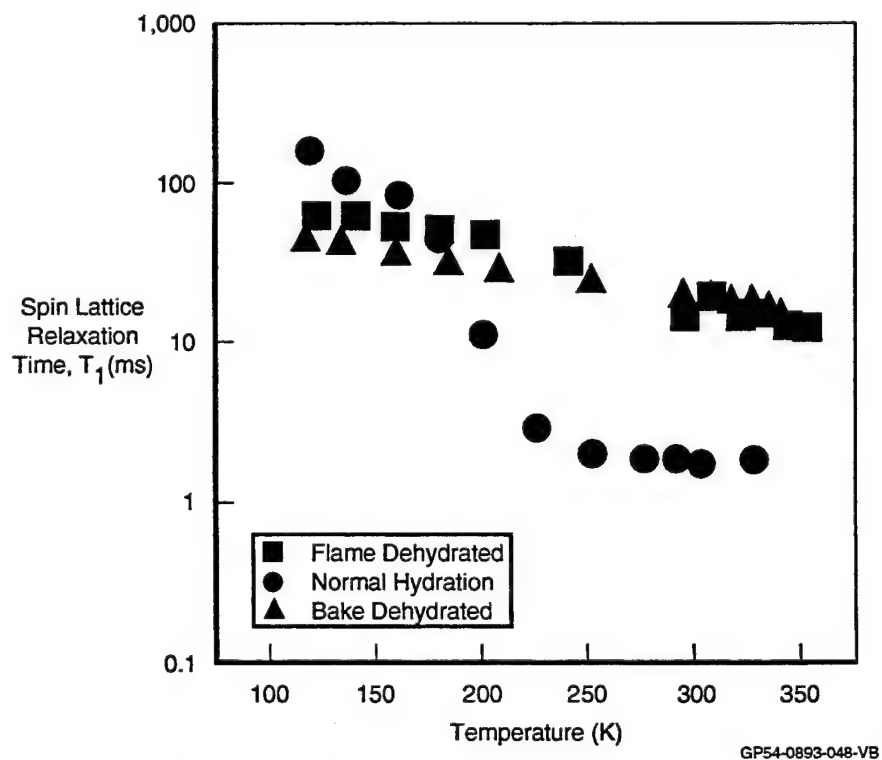
Figure 2.3.4-3. Hydrogen NMR Evaluation of Hydrated and Dehydrated Corrosion Products as a Function of Temperature (2.0 Tesla/85 MHz).

39

Active corrosion sites are likely to be moist; hence, the corrosion should be in an elevated state of hydration. The data presented in Figures 2.3.4-1 to 2.3.4-3 indicate that at temperatures near room temperature, the NMR signal near active corrosion sites will have a short T_1, which will allow for rapid signal averaging and differentiation from most other materials. Furthermore, the corrosion product will have a long T_2 (compared to rigid solids), which will require only a modest bandwidth of the detection spectrometer (as opposed to the larger bandwidth required for rigid solids). Smaller bandwidth translates into better signal-to-noise.

2.3.5 Effects of Included Aerospace Materials

Of paramount importance in the detection of corrosion in aluminum is the ability to differentiate the NMR signal of corrosion from the NMR signal of miscellaneous (innocuous) aircraft materials. Materials such as paint, primer, polysulfide sealant, film and foaming adhesive and a carbon-fiber composite material were evaluated using a hydrogen NMR technique at 2.0 Tesla (85 MHz). Critical NMR parameters were determined for each material, with the data listed in Figure 2.3.5-1. Several of the materials evaluated have two-component NMR signals; the T_1 and T_2 values reported in this figure are of the longer lived component, even though it may have a lower intensity than the shorter lived (more rigid) NMR signal. The longer T_2 component is more likely to interfere with the signal emanating from the corrosion product. The value for the T_1 of the aluminum corrosion product is much shorter than T_1 of any of the included materials evaluated. As a result, it will be possible to distinguish the NMR signal of aluminum corrosion product from the NMR signal from various included materials.

Material	T_2 (μS)	T_1 (mS)	$T_{1\rho}$ (μS)
Corrosion Product	107	19	521
Paint	75	152	1298
Primer	271	77	1664
FM-400 Film Adhesive	14	629	1890
FM-300 Film Adhesive	642	151	6504
AS4/3501-6 Carbon/Epoxy	294	478	2297
FM 404 Foam Adhesive	238	587	2945
EA 9394 Liquid Shim	287	383	4717
Sealant	98	62	4279

GP54-0893-49-VB

Figure 2.3.5-1. Hydrogen NMR Relaxation Times For a Variety of Included Aerospace Materials (2.0 Tesla/85 MHz).

Figure 2.3.5-2 shows NMR signals from all aircraft materials and the signal from aluminum corrosion product in a single plot. These signals were normalized by (divided by) the mass of the specimen. These data were acquired by saturating the NMR line (equalizing the populations of the respective energy levels by eliminating the nuclear magnetization), allowing the nuclear magnetization to recover for 20 seconds and inspecting the signal from the recovered magnetization. Because the recovery period (20 seconds) is much greater than T_1 of any of the aircraft materials, the resultant signal is fully relaxed; all spins contribute to the observed signal in proportion to their numbers. When acquiring a signal from several materials simultaneously, it is useful to reduce the recovery period so that it is less than T_1 for all of the materials. Thus, materials with a short T_1 will contribute disproportionately to the total signal. Indeed, when the recovery period is reduced to 7 ms, as shown in Figure 2.3.5-3, the only signals that remain come from corrosion and from the polysulfide sealant. However, because the T_1 of the sealant is longer than T_1 of the corrosion (62 ms vs. 19 ms), another pulse sequence can be employed to null out the sealant signal.
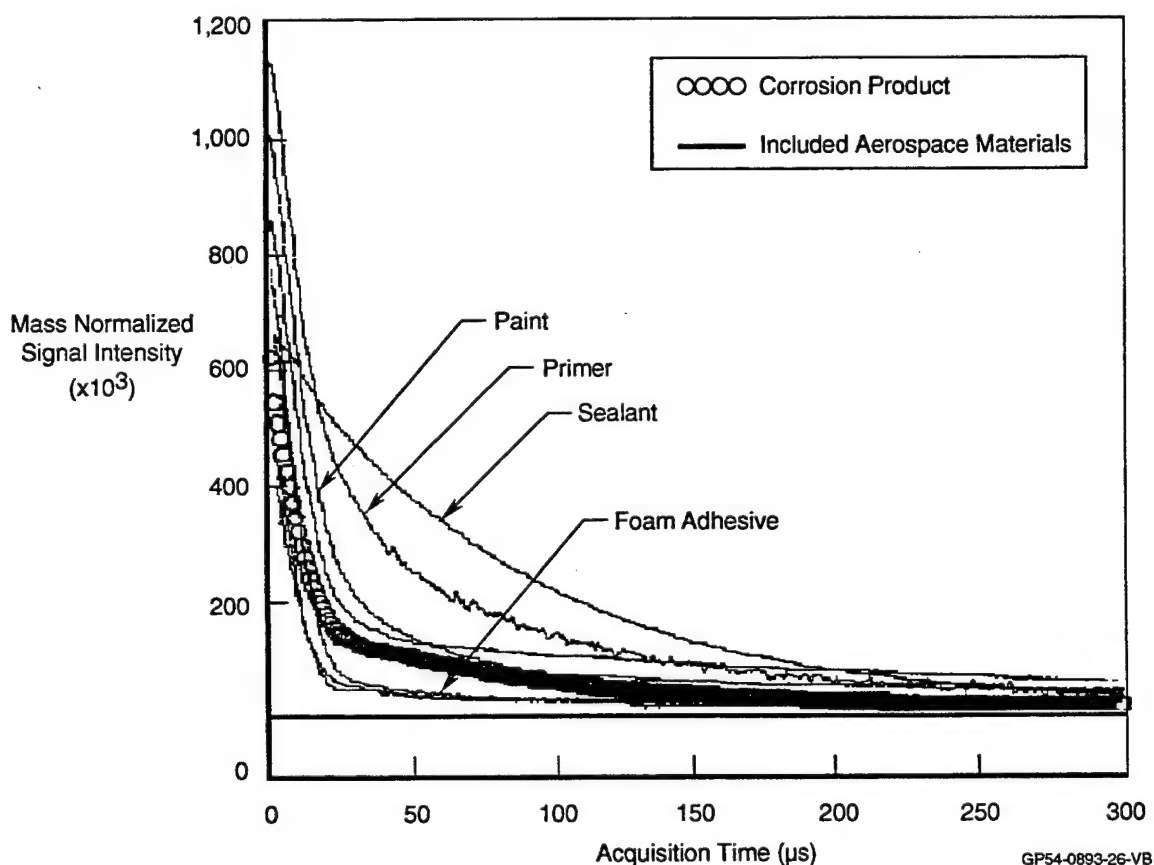
Figure 2.3.5-2. Fully Relaxed Hydrogen NMR Signals From Aluminum Corrosion Product and Included Aerospace Materials Listed in Figure 2.3.5-1 (2.0 Tesla/85 MHz).
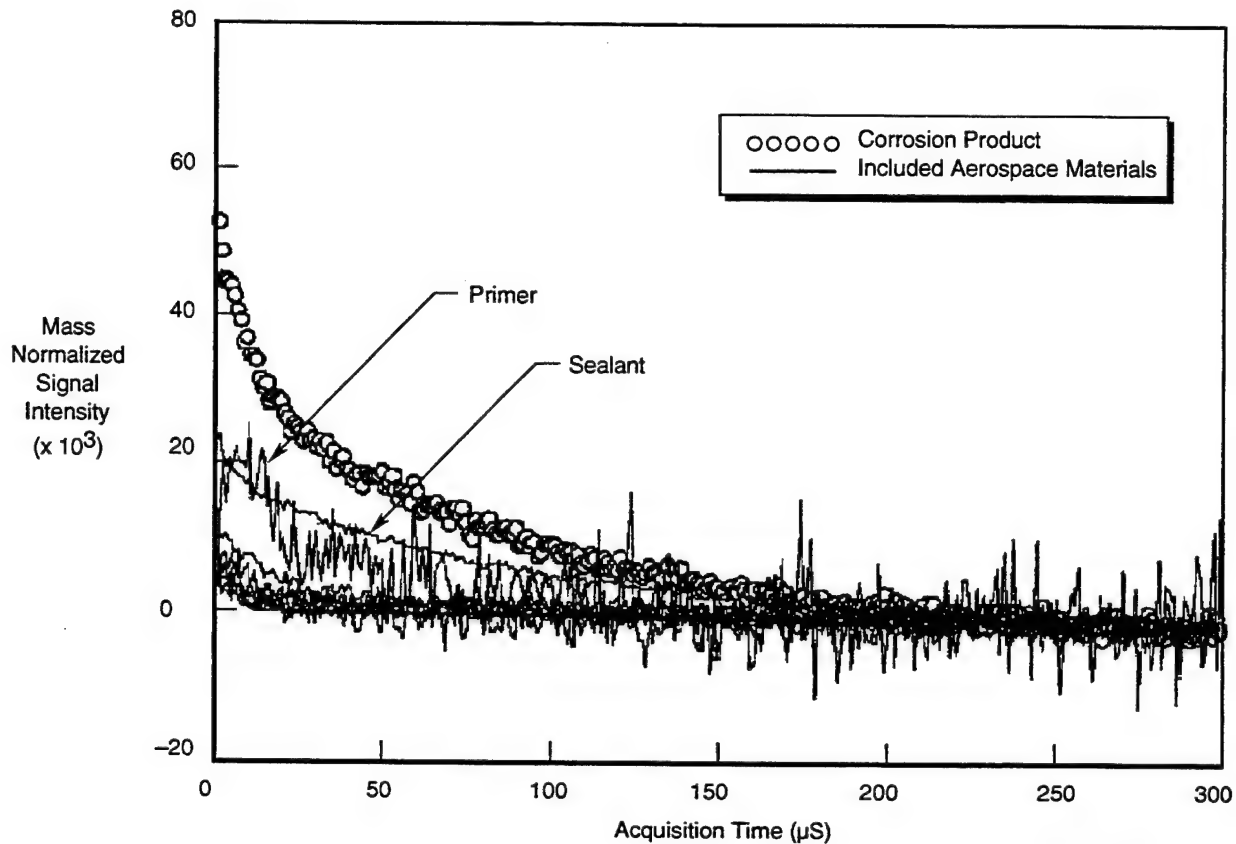
Figure 2.3.5-3. Hydrogen NMR Signals of Aluminum Corrosion Product and Included Aerospace Materials Acquired With a Saturate-Wait (1.0 ms)- Inspect Pulse Sequence (2.0 Tesla/85 MHz).

An RF pulse of the appropriate intensity and duration can be applied so that the NMR signal is inverted, as shown in Figure 2.3.5-4. If the signal is inspected at some time after the inverting RF pulse, it will still be inverted, but at a smaller magnitude. As the recovery time (the time between the inversion RF pulse and the signal inspection) is increased, the signal amplitude will progress from small and inverted, to zero, then small and upright, and finally, fully relaxed and upright. If a specimen consisting of sealant and aluminum corrosion product is inspected, the recovery time in the "invert-recover-inspect" pulse sequence can be chosen so that the signal from the sealant is minimized with respect to the corrosion signal, as illustrated in Figure 2.3.5-5. In this manner, the sealant signal can be differentiated from the signal of sealant combined with corrosion.
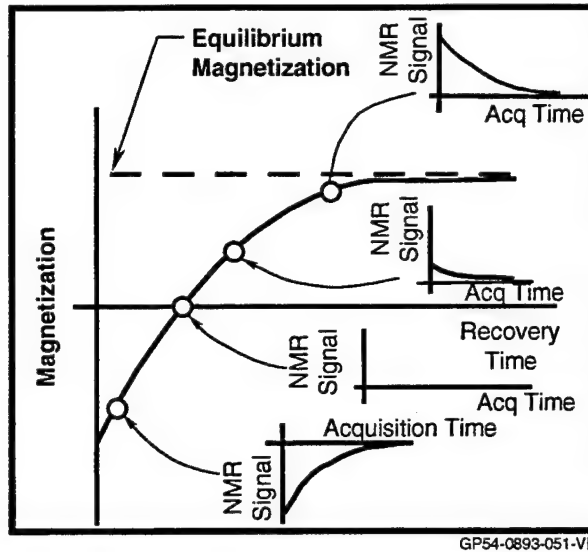
Figure 2.3.5-4. Graphic Representative of Inversion Recovery.
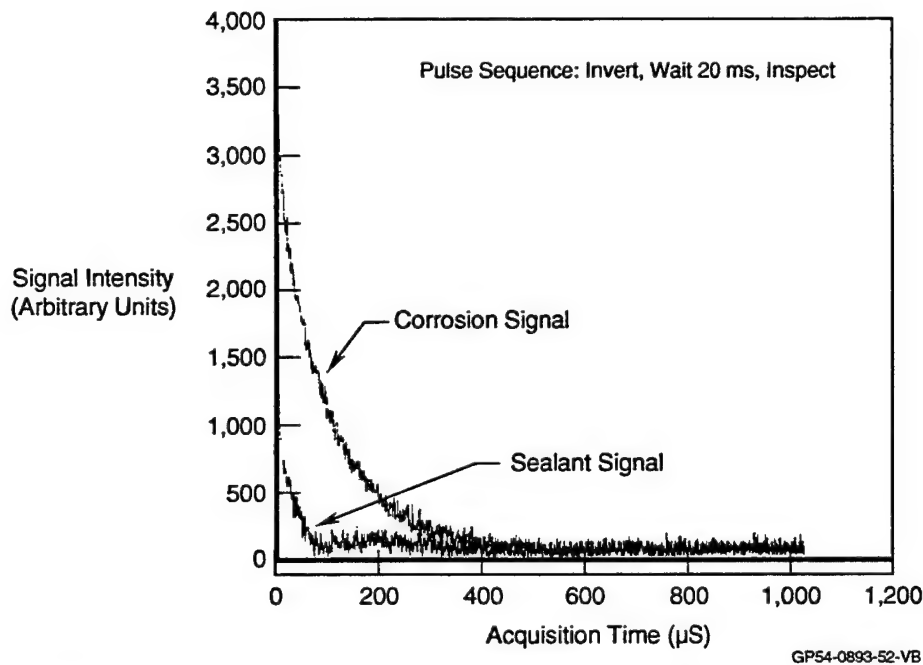
Figure 2.3.5-5. Differentiation of Corrosion Product and Sealant Hydrogen NMR Signals Using an Invert-Recover-Inspect Pulse Sequence (2.0 Tesla/85 MHz).

2.3.6 Effects of Fastener Materials

Corrosion-resistant metallic fasteners are those made of stainless steels and non-ferrous alloys. This broad definition could include hundreds of alloys, but in practice the materials actually used are limited to several stainless steels and several copper alloys, plus a few nickel, aluminum and titanium alloys [7].

43

Over half of all industrial fasteners classified as corrosion resistant are made of stainless steels. This general designation covers austenitic, martensitic and ferritic stainless steels. Of all stainless steels, the 300 series austenitic types are the most popular for fastener use. Austenitic stainless steels are nonmagnetic for all practical purposes. Martensitic grades, such as type 410 and 416, and ferritic alloy type 430 are all magnetic and would be detrimental to NMR.

Aluminum alloys, such as 2117 and 2024, are used for fasteners, primarily in the form of rivets. Typically, aluminum fasteners are used to join aluminum components. Titanium alloy Ti-6Al-4V is used extensively for titanium fasteners. They have excellent corrosion resistance and maintain their strength at moderately high temperatures.

As was described in Section 2.3.1, highly magnetic materials are not ideal candidates for NMR. A simple test may be performed to determine if the ferromagnetic behavior of the fastener would inhibit an NMR evaluation. This test is performed by simply placing a permanent magnet near the fastener. If the attraction is immediate, then it is safe to say that an NMR signal would be lost in the vicinity of the fastener. If no attraction is observed, then NMR measurements are still a possibility and the effectiveness of such would need to be determined experimentally. Using this simple screening procedure, fasteners fabricated from a variety of materials were evaluated, with the results shown in Figure 2.3.6-1 [8]. As can be seen by this screening process, fasteners fabricated from PH13-8Mo steel would destroy an NMR signal.

Fastener Type	Part Number	Material	Screening Results
Hi-Lok (Flush Head)	ST3M419V	Ti-6Al-4V	No Attraction
Hi-Lok (Protruding Head)	ST3M420V	Ti-6Al-4V	No Attraction
Hi-Lok (Protruding Head)	ST3M420C3	A286	No Attraction
Screw	MS42693	SS304	No Attraction
Rivet	MS20470	Al 2117-T4	No Attraction
Hi-Torque (Flush Head)	ST3M454	PH13-8Mo	Strong Attraction

GP54-893-7-VB

Figure 2.3.6-1. Fasteners Surveyed For Magnetic Properties [8].

An experiment was performed using a titanium fastener to determine if magnetic behavior existed. This was a concern since the Ti-6Al-4V has a 0.4% Fe impurity limit, which may be enough to show some magnetic behavior. A Ti-6Al-4V protruding head hi-lok fastener (ST3M420V8) was used to determine if ferromagnetic behavior was present. Hydrogen NMR signals were obtained at 85 MHz for the titanium fastener, a water sample and the fastener immersed in water. The acquired hydrogen NMR signals are shown in Figure 2.3.6-2. This figure reveals several items of note: (1) there is no residual hydrogen signal in the titanium fastener; (2) the hydrogen signal from the water has a very long duration with no fastener present; and (3) the hydrogen signal from the water decreased dramatically if a titanium fastener is placed in the water. The latter result indicates that the titanium fastener has paramagnetic susceptibility. As will be seen in Section 3.3.2, the paramagnetism exhibited by the titanium fastener does little to affect an NMR signal from aluminum corrosion in the vicinity of the fastener.
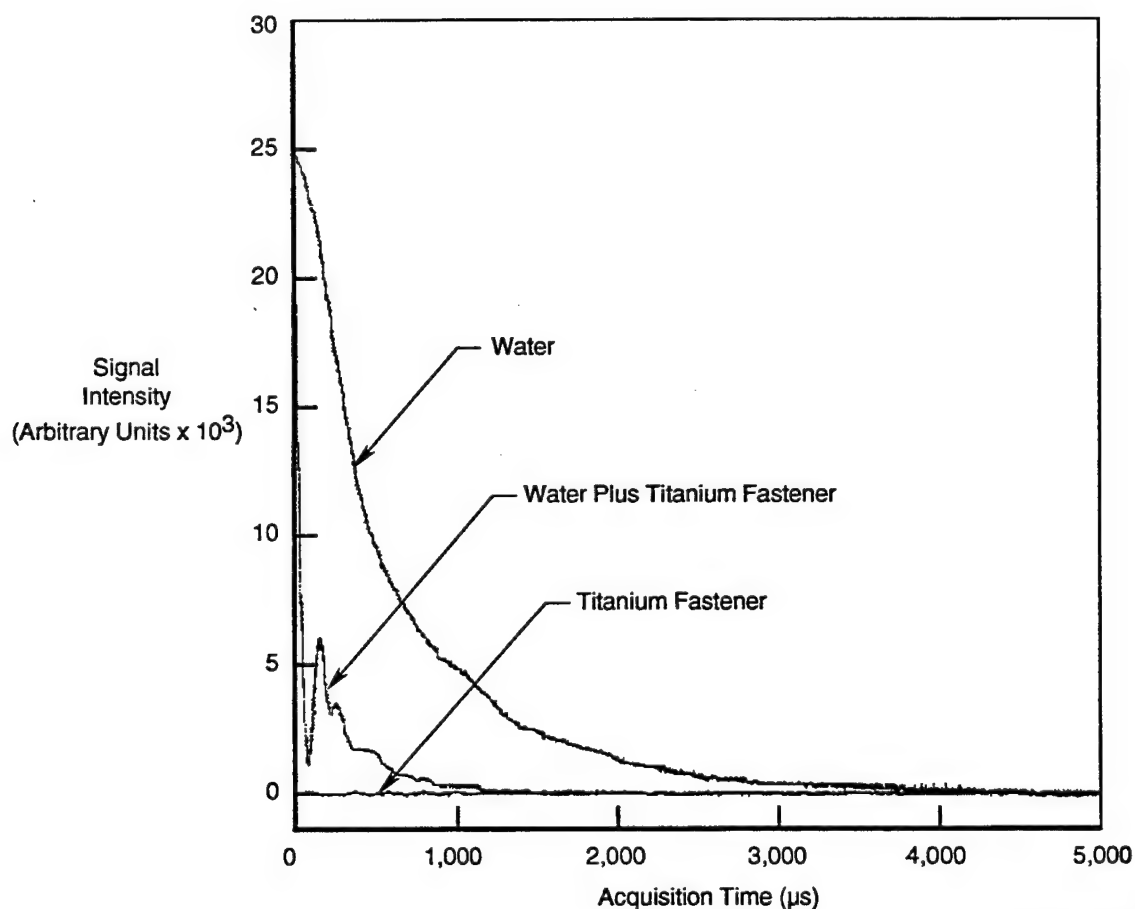
GP54-0893-053-VB

Figure 2.3.6-2. Effects of Titanium (Ti-6Al-4V) Fastener on Hydrogen NMR Signal Obtained From Water (2.0 Tesla/85 MHz).

THIS PAGE INTENTIONALLY LEFT BLANK

3.0 NMR EVALUATION OF SIMULATED AIRFRAME STRUCTURES

The objective of this task was to assess the feasibility of detecting corrosion in complex airframe structures. Key to the success of NMR as a substructure corrosion detection method is the behavior of the RF magnetic field in the vicinity of joints and fastener holes. To evaluate this, both 2-D and 3-D electromagnetic modelling codes were employed to evaluate this behavior. In addition, NMR experiments were performed on simple aircraft structures such as a butt joint, lap joint and fastener/fastener hole combinations to verify the modelling results. To conclude this task, the ability to detect corrosion in these simple structure configurations and under coatings using NMR was experimentally determined using laboratory NMR hardware. The results of these investigations are presented in detail in the following subsections.

3.1 RF Magnetic Field Modelling

The objective of the RF magnetic field modelling subtask was to theoretically determine if RF magnetic fields can penetrate joints and propagate in gaps underneath skins in the frequency range of interest to NMR. If it was determined that no RF magnetic field penetration occurs, then the subsequent experimental study would focus on detection of corrosion under coatings and sealants. Electromagnetic modelling codes routinely employed to evaluate electromagnetic wave behavior for materials and structure development relative to low observable technology were used in this investigation.

3.1.1   Electromagnetic Modelling Codes

In order to better understand RF magnetic field behavior in the vicinity of joints, gaps and holes, electromagnetic modeling codes originally developed for low observable technology were employed. Although several computational electromagnetics codes were evaluated, The Code for Analysis of Radiation on Lossy Surfaces (CARLOS) was utilized for the bulk of the modelling effort. CARLOS implements the method of moments solution for fully arbitrary three-dimensional complex scatterers [9]. These solutions were obtained for perfectly electrically conducting bodies as well as fully or partially penetrable ones. The electromagnetic scattering formulation is based on surface integral equations spanning the entire external surface of the body and the internal boundaries between penetrable and perfectly electrically conducting regions. All of the surface integral equation formulations, whether for perfectly electrically conducting or penetrable bodies, are derived from the Stratton-Chu [10] and Maue

[11] formulations. These implicitly satisfy the Sommerfeld radiation condition at infinity. This results in a rigorous theoretical formulation for all of the foregoing classes of problems with the computational domain terminated at the outer surface of the scatterer. This is in contrast to partial differential equation solvers of Maxwell's equations where either the computational domain must be extended beyond the outer surface of the scatterer or various approximate on-surface or off-surface boundary conditions must be imposed [12].

3.1.2   Butt Joint Analysis

The butt-joint, one of the primary structural joining configurations, consists of two outer mold line skins butted together and mechanically fastened to a common substructure. From a corrosion standpoint, attention must be paid to the joint area and the gap between the outer mold line skins and the substructure. Based on these concerns, a model structure was developed for CARLOS where RF magnetic field behavior could be evaluated as functions of both joint gap width and plate spacing between surface and substructure. This model is shown schematically in Figure 3.1.2-1. In this model, a single-loop, 0.1 inch
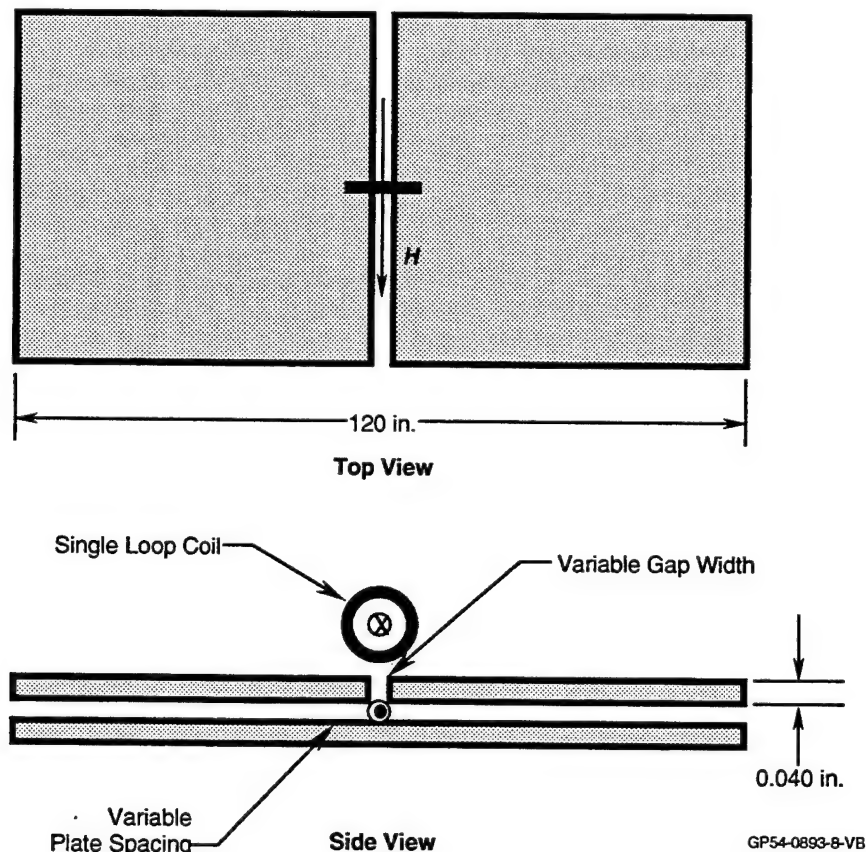
Figure 3.1.2-1. Butt-Joint Structure/Surface Coil Configuration For RF Magnetic Field Modelling.

48

diameter coil was oriented such that the RF magnetic field was aligned parallel to the joint. This orientation allows for maximum penetration of the RF magnetic field. The overall length of the structure was chosen so that edge effects would be minimized and terminations would not be necessary. In order to compliment experimental data, all calculations were made at a fixed frequency of 85 MHz (2.0 Tesla for hydrogen).

For the first set of calculations, the joint gap widths chosen for analysis ranged from a maximum of 0.020 inches to a minimum of 0.001 inches with a fixed plate spacing of 0.010 inches. The results of the variable joint/fixed plate spacing analysis is shown in Figure 3.1.2-2. The normalized (to the excitation field) RF magnetic field intensity is plotted as a function of distance along the structure using a four inch window centered around the joint. The results indicate that RF magnetic field is present in the joint and a short distance beneath the outer mold line skins. The field essentially dies out 0.5 inches on either side of the joint. It was interesting to note that the intensity varied little as a function of gap width in the range chosen. The data in Figure 3.1.2-3 show a set of calculations where the joint gap width was held constant at 0.010 inches and the plate spacing was varied from 0.005 to 0.020 inches. Here again, the results show that even at plate spacings down to 0.005 inches, RF magnetic field is present. Also, much like the variable joint gap width analysis, the field intensity out to 0.5 inches on either side of the gap changed little as a function of plate spacing. Calculations with plate spacings down to 0.001 inches were attempted; however, the effects of Greens Theorem at extremely small plate spacings resulted in "no solution."
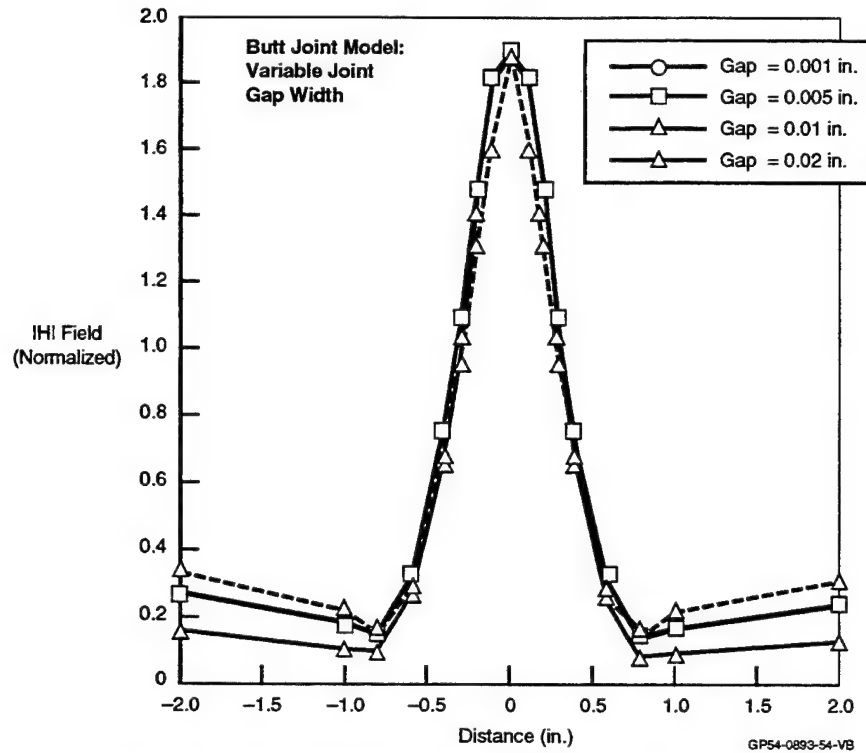
Figure 3.1.2-2. RF Magnetic Field Modelling Results For Variable Joint Width in a Butt-Joint Structure (Plate Spacing = 0.010 in./Frequency = 85 MHz).
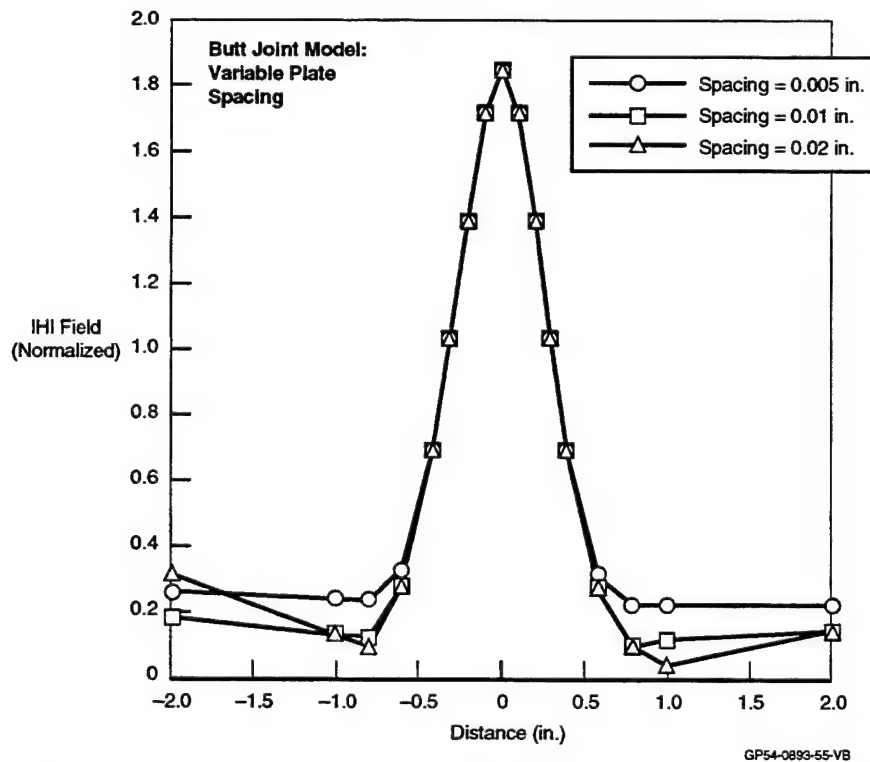
Figure 3.1.2-3. RF Magnetic Field Modelling Results For Variable Plate Spacing in a Butt-Joint Structure (Joint Gap Width = 0.010 in./Frequency = 85 MHz).

50

In addition to gaps and plate spacings, the effects of grounding (top shield planes) were analyzed relative to the butt-joint structure. In the calculation shown in Figure 3.1.2-4, the joint gap width was 0.020 inches and the plate spacing was 0.005 inches. The two sets of data show the RF magnetic field behavior in the vicinity of the joint in cases where the structure is grounded and ungrounded. The results show that the grounded case yields consistently higher intensity fields in the vicinity of the joint. This effect was due to the ground plane acting as a reflector of energy, thereby intensifying the RF magnetic field at and near the joint.
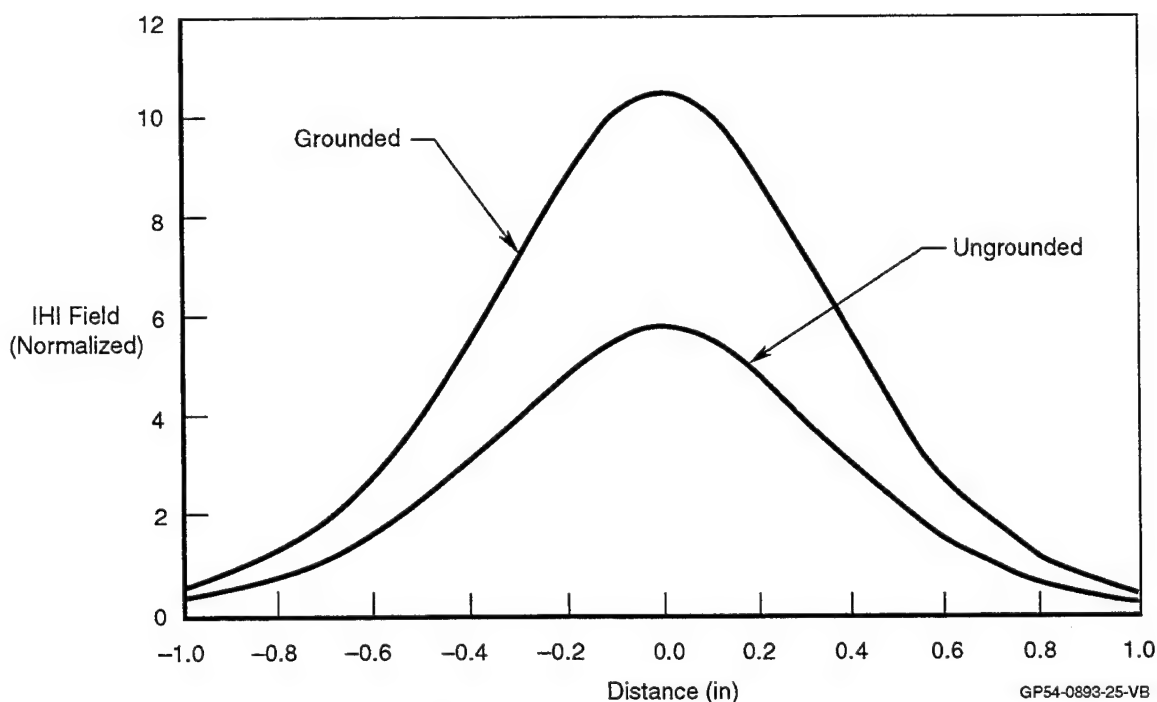
Figure 3.1.2-4. RF Magnetic Field Modelling Results Showing Effects of Grounding Relative to a Butt-Joint Structure (Plate Spacing = 0.020 in./Joint Gap Width = 0.005 in./Frequency = 85 MHz).

3.1.3 Lap Joint Analysis

Another of the primary structural joining configurations is the lap joint. From a corrosion standpoint, attention must be paid to the gap in the overlap region as a potential source for moisture intrusion. Similar to the butt joint analysis described previously, a model was developed for the lap joint configuration. This model is shown schematically in Figure 3.1.3-1. Like the butt-joint model, a single-loop, 0.1 inch diameter coil was oriented such that the RF magnetic field was aligned parallel to the joint. The overall length of the structure was chosen so that edge effects would be minimized and terminations would not be necessary. All calculations were made at a fixed frequency of 85 MHz (2.0 Tesla for hydrogen).
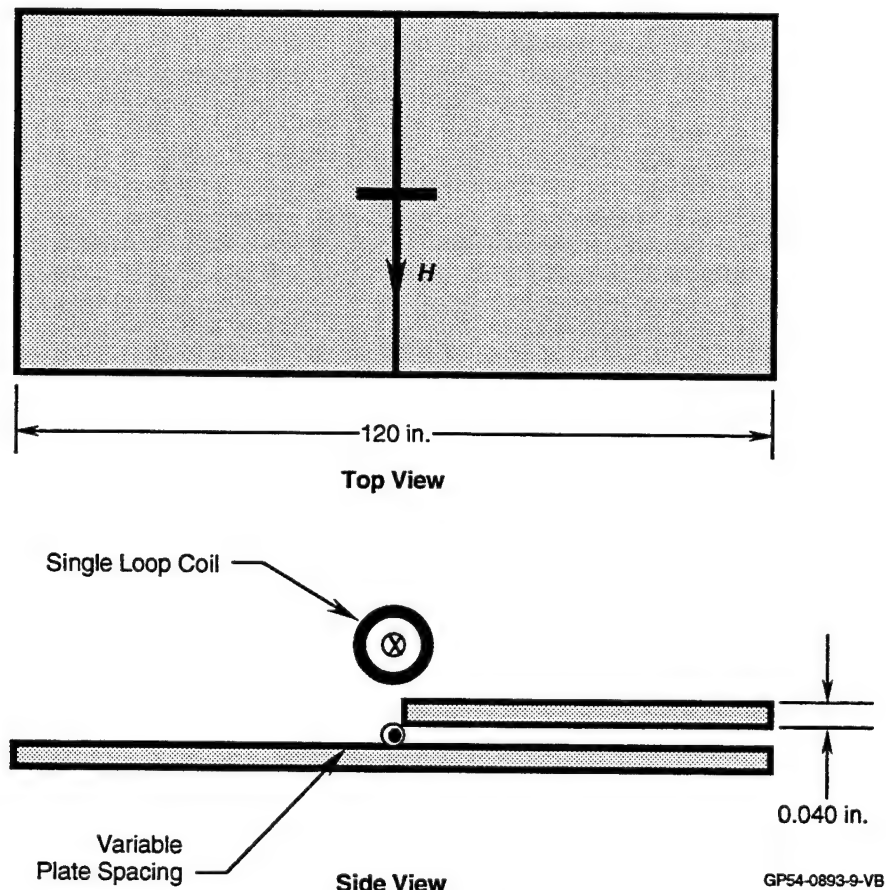
Figure 3.1.3-1. Lap-Joint Structure/Surface Coil Configuration For RF Magnetic Field Modelling.

A set of calculations were made for the lap joint model where the overlap spacing ranged from 0.010 to 0.020 inches, the results of which are shown in Figure 3.1.3-2. Attempts were made using smaller overlap spacings; however, similar to the butt joint calculations, the effects due to Green's Theorem at extremely small spacings resulted in no solution. At spacings between 0.010 and 0.020 inches, the results were remarkably consistent.. In fact, at 0.5 inches away from the joint, the RF magnetic field intensities were equivalent to those identified for the butt joint (approximately 28% of the RF magnetic field intensity at the joint).

GP54-0893-56-VB
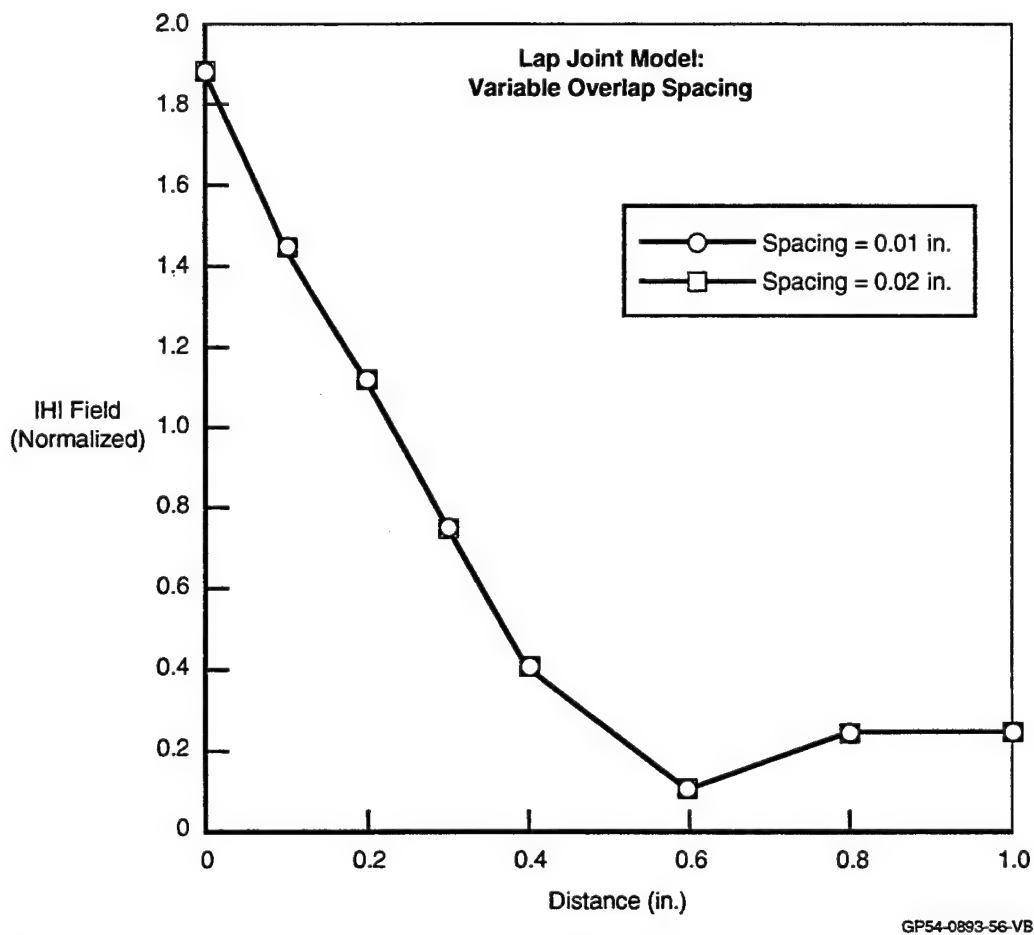
Figure 3.1.3-2. RF Magnetic Field Modelling Results For Variable Overlap Spacing in a Lap-Joint Structure (Frequency = 85 MHz).

3.1.4 Fastener Hole Evaluation

The third area of concern from a moisture intrusion or corrosion standpoint is the fastener hole. Moisture intrusion and corrosion frequently occur in gaps between fastener and fastener hole. A simple model, shown schematically in Figure 3.1.4-1, was developed to simulate these conditions. A single-loop, 0.01 inch diameter coil was oriented such that the RF magnetic field was aligned parallel to the joint. A circular structure was chosen so that edge effects, if any would not be preferential to any one orientation. The overall dimension was chosen so that edge effects would be minimal. A circular gap of 0.006 inches was used to simulate an arbitrary gap between fastener hole of 0.800 inches and a fastener. The plate spacing was chosen to be 0.030 inches. All calculations were made at a fixed frequency of 85 MHz (2.0 Tesla for hydrogen).

GP54-0893-10-VB
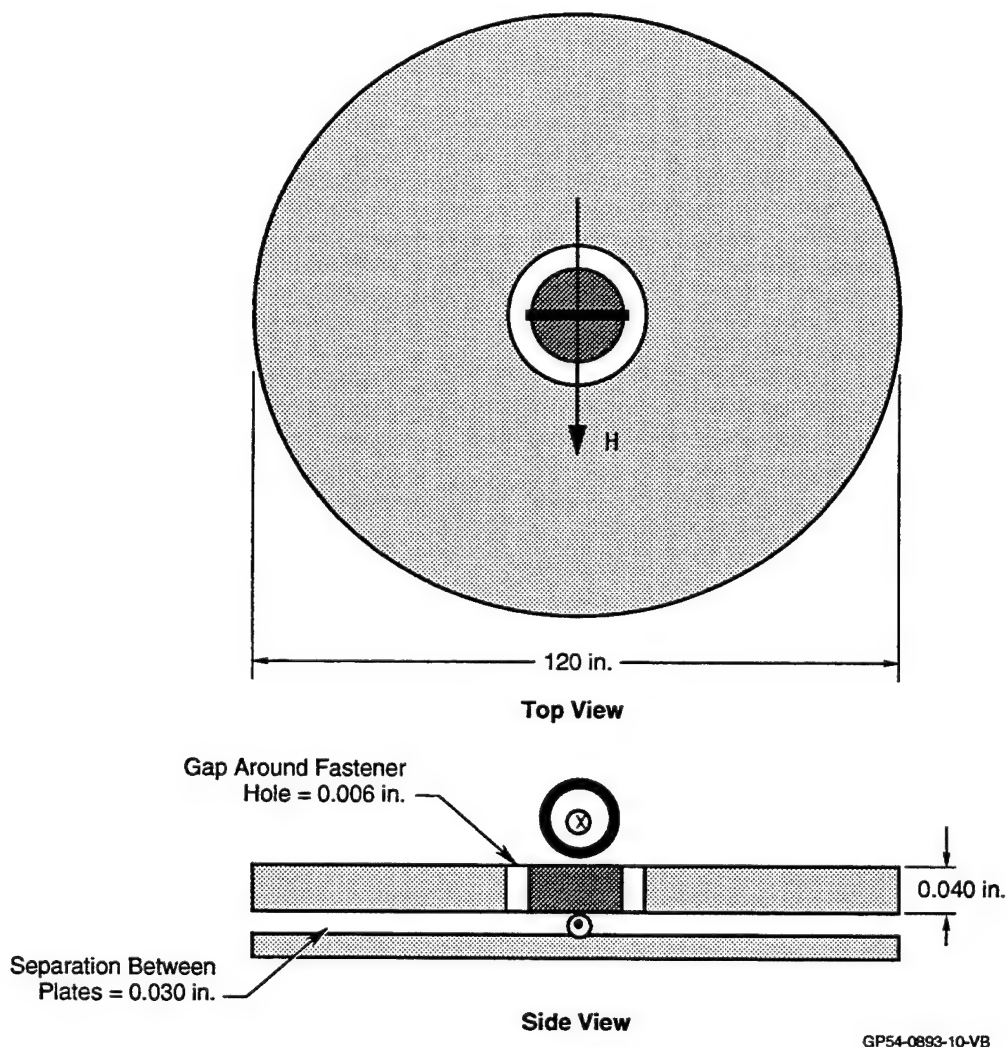
Figure 3.1.4-1. Fastener Hole Structure/Surface Coil Configuration For RF Magnetic Field Modelling.

Calculations were made relative to the fastener hole model described previously. The results in Figure 3.1.4-2 were obtained by varying the fastener hole diameter and keeping the surface coil diameter constant. The results show a negligible change in RF magnetic field intensity as a function of hole diameter (in the range evaluated). A complementary calculation was made by holding the fastener hole diameter constant at 0.8 in. and varying the surface coil diameter. The results in Figure 3.1.4-3 show that the smaller coil diameter (0.1 in.) produces magnetic fields that fall off slower than those for the larger coil. At a distance of one inch away from the center of the hole, the difference is about 50%. The key result obtained from this evaluation was that with the circular geometry and gaps comparable to those used for the joint models, the RF magnetic field still penetrates into the gap.
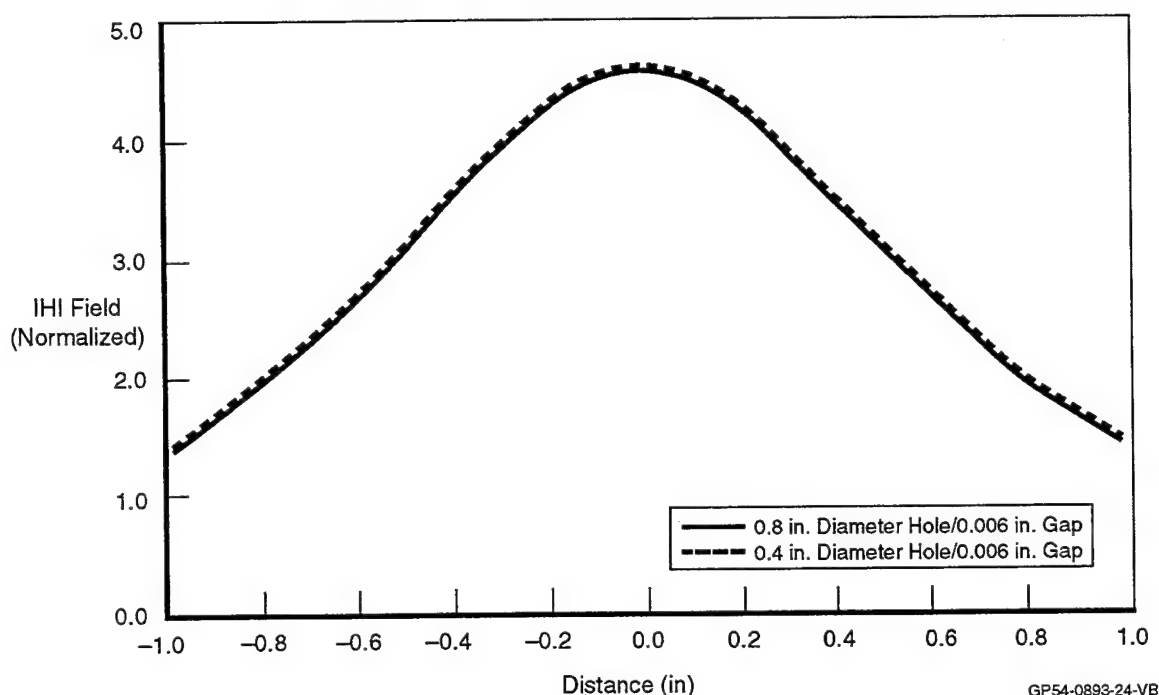
Figure 3.1.4-2. RF Magnetic Field Modelling Results for Variable Fastener Hole Diameter (Plate Spacing = 0.030 in./Gap = 0.006 in./Frequency = 85 MHz).

55
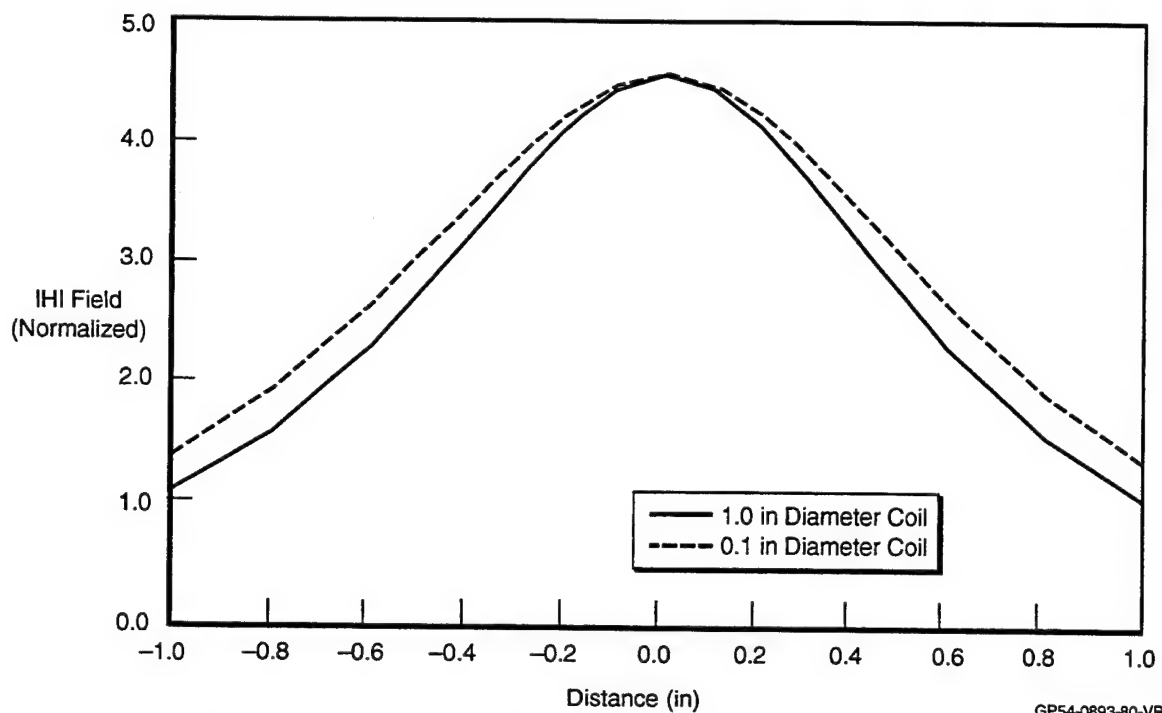
Figure 3.1.4-3. RF Magnetic Field Modelling Results for Variable Surface Coil Diameter (Plate Spacing = 0.030 in./Gap = 0.006 in./Frequency = 85 MHz).

3.2 Simple Structure RF Magnetic Field Evaluation

In order to verify the RF magnetic field modelling results, a set of simple structures were fabricated to simulate structural configurations commonly found on airframes. These simple structures consisted of a butt-joint, lap joint and fastener configurations. The measurements were made using the 2.0 Tesla electromagnet at a frequency of 85 MHz for hydrogen NMR. A shielded surface coil was placed close to the surface of the structure with the magnetic field oriented parallel to surface for all structures. For the joint structures, the magnetic field was oriented parallel to the joint as well. The experimental configuration is shown in Figure 3.2-1.
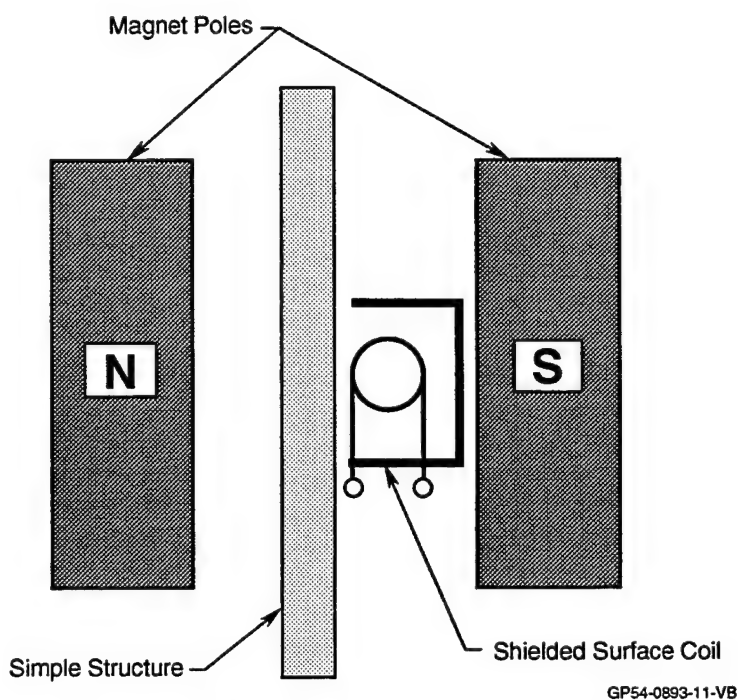
Figure 3.2-1. Experimental Configuration For RF Magnetic Field Evaluations.

3.2.1 Butt Joint Configuration

A simple structure was constructed out of 2024 sheet aluminum to represent a butt-joint. The structure design is shown schematically in Figure 3.2.1-1 and pictorially in Figure 3.2.1-2. The structure was created in a flexible, modular fashion that allows the experiment to vary both the joint gap width and spacing between the outer mold line (OML) skins and substructure. In addition, inspection coils, tuning elements and static field monitoring devices could be changed quickly.
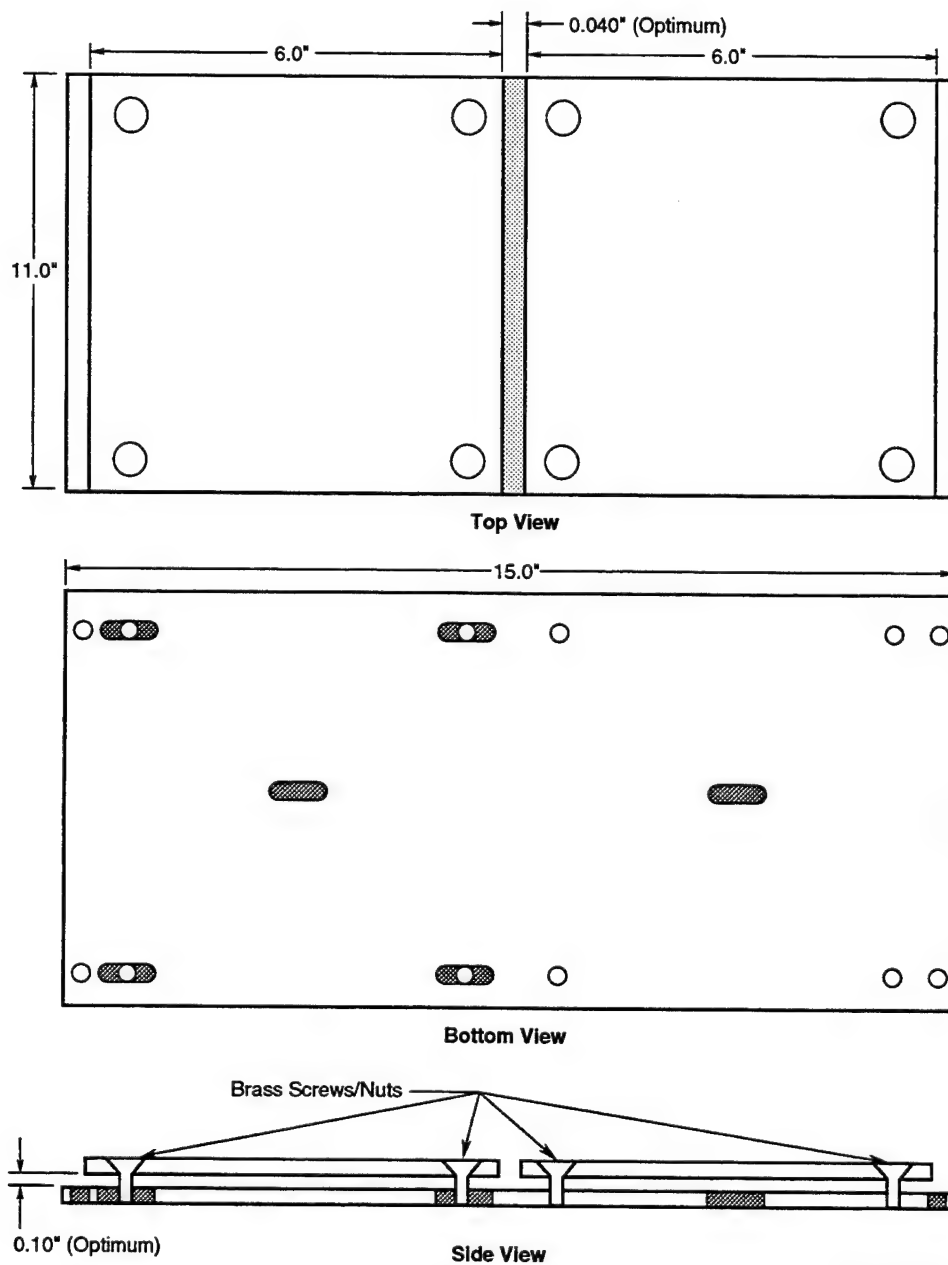
Figure 3.2.1-1. Schematic Representation of Butt-Joint Simple Structure Developed For RF Magnetic Field Evaluation.

GP54-0893-81-VB
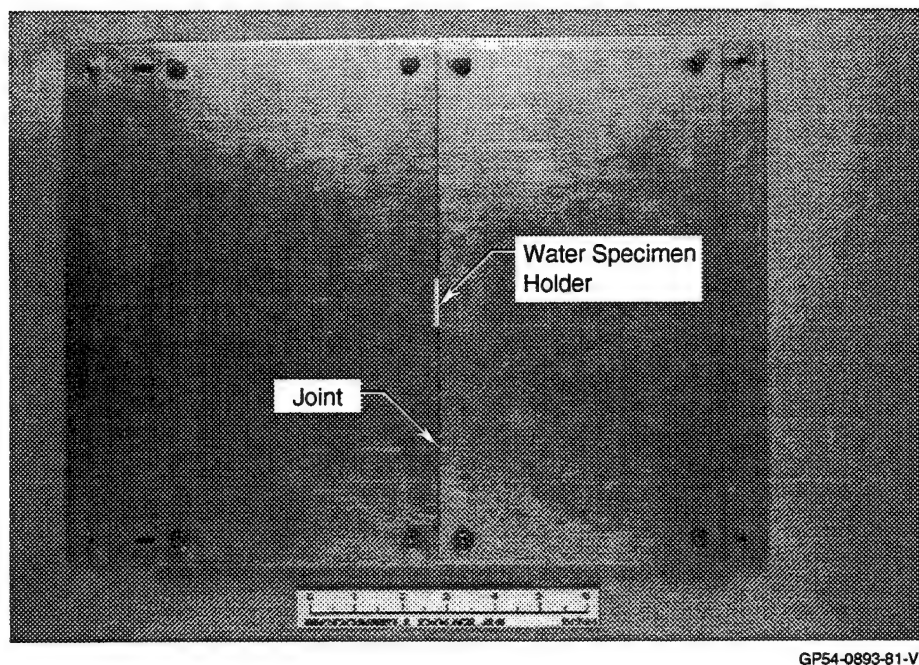
Figure 3.2.1-2. Photograph of Butt-Joint Simple Structure.

RF field strength was measured using NMR on a specimen placed in the butt-joint. The NMR experiment performed was a two pulse sequence. The nuclear magnetization present after the first pulse was:

$$M(\text{pulse width}) = M_0\cos(\text{pulse width x RF field strength x } \gamma)\, e^{(-\text{pulse width x } \Delta v_1)} \qquad (8)$$

where M_0 is the initial magnetization, γ is the gyromagnetic ratio and Δv_1 represents the inhomogeneity in the magnetic field. The size of the signal after the second pulse was proportional to the nuclear magnetization after the first pulse. By finding the first zero crossing in the amplitude of the signal after the second pulse, it is easy to determine the RF field strength at the NMR specimen.

Initial work with the butt-joint simple structure was performed with a solenoidal coil whose axis was oriented parallel to the butt-joint gap. The solenoidal coil had an inner diameter of 0.2 inches, a length of 0.25 inches and 6.5 turns. The specimen used to evaluate the RF field was a small capillary tube (0.040 inch inner diameter) of water held in a Teflon specimen holder. From the center of the coil to the center of the specimen holder was a distance of 0.3125 inches. The specimen was moved from directly under the joint gap to 0.4 inches from the center of the gap. The plate spacing was held constant at 0.120 inches, while the joint gap was varied from 0.012 to 0.100 inches. The data collected are shown in Figure 3.2.1-3. The data contained in this plot can be compared with the modelling data shown in Figure

3.1.1-2. Qualitatively, both sets of data show that the amount of RF that penetrates into the butt joint decreases as the distance away from the joint increases. Quantitatively, there are differences which may possibly be attributed to source size, grounding conditions and/or two dimensional modelling calculations.
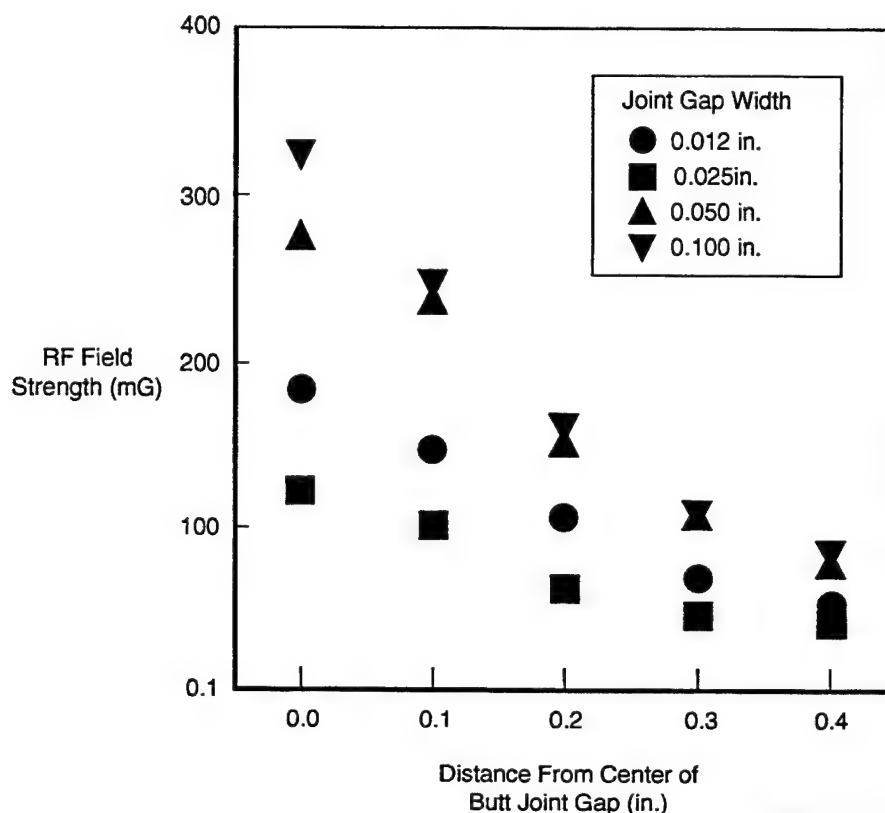
Figure 3.2.1-3. RF Magnetic Field Penetration Data Collected Using a Solenoidal Coil With Joint Gap Widths Ranging From 0.012 to 0.100 in. (2.0 Tesla/85 MHz).

As shown in the schematic in Figure 3.2.1-1, there were eight screws that connected the substructure to the outer mold line skins. The data shown in Figure 3.2.1 were collected with the brass screws connecting the OML skins to the substructure, thereby grounding the OML skins. To simulate conditions where no grounding was present, nylon screws were used to connect the structure. Figure 3.2.1-4 presents data collected in both grounded and ungrounded conditions. The results show a slight increase in RF field intensity for the grounded condition. The change was less dramatic than was revealed in the modelling exercise. A possible explanation for this may be that, for the experimental conditions, the structure was not ideally grounded. For the respective model, ideal grounding was the case.
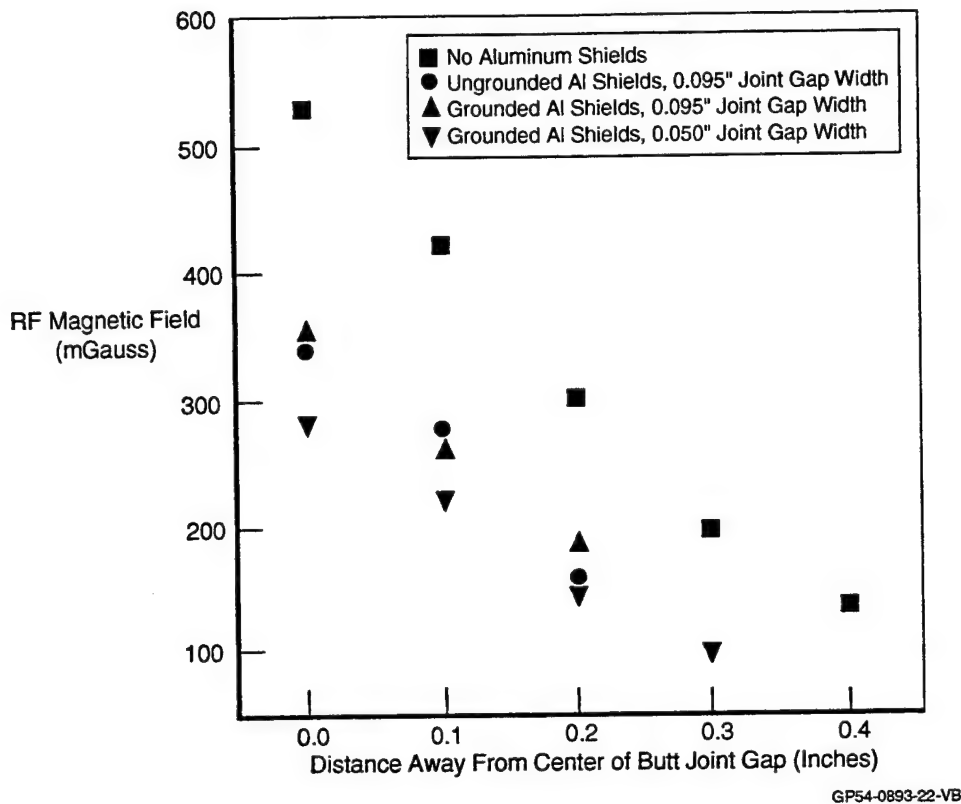
Figure 3.2.1-4. Plot of RF Magnetic Field as Functions of Joint Gap Width and Grounding Condition.

A long solenoidal coil generates an RF field that is parallel to its axis, but which is located primarily inside the coil windings. By winding a coil in the shape of a "figure-eight," it is possible to generate an RF field pattern that has a larger amount of the RF field external to the coil. In addition, the RF field projected toward the butt-joint gap by the figure-eight coil is larger than the RF field projected by the solenoidal coil. Both solenoidal and figure-eight coils are pictured in Figure 3.2.1-5. A figure-eight coil was wound with two complete turns, each with a diameter of 0.4375 inches. It was placed such that the bottom-most winding was 0.25 inches from the center of the water specimen holder. A comparison of the RF fields generated by the figure-eight coil and the solenoidal coil is shown in Figure 3.2.1-6. As can be seen, the figure-eight coil projects an RF field into the butt-joint gap with an intensity approximately 3.5 times as large as the RF field projected for the solenoidal coil. In other words, the figure-eight coil is a better transmission antenna; by a well known reciprocity theorem, it is a better receiving antenna as well.

Side View

Top View

(a)

Side View

Top View

(b)
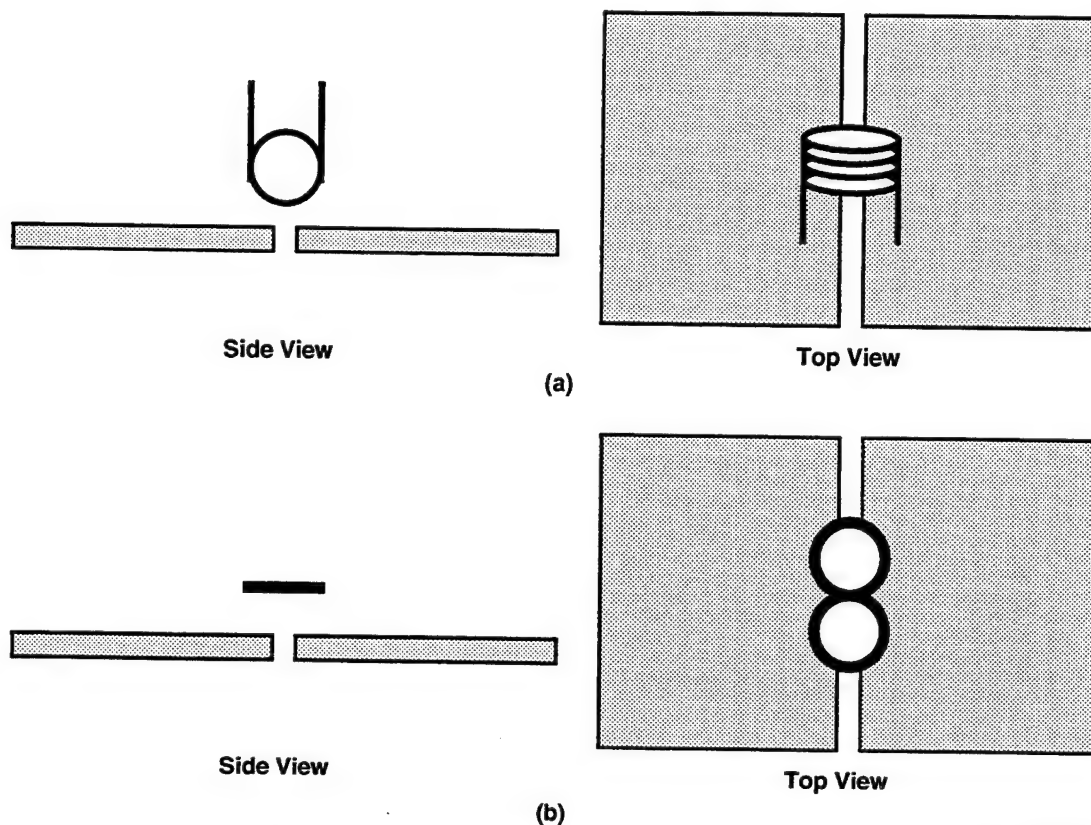
GP54-0893-59-VB

Figure 3.2.1-5. Coils Used for RF Magnetic Field Evaluation: (a) Solenoidal Coil
and (b) Figure-Eight Coil.

RF Magnetic
Field
(mGauss)

Distance From Gap
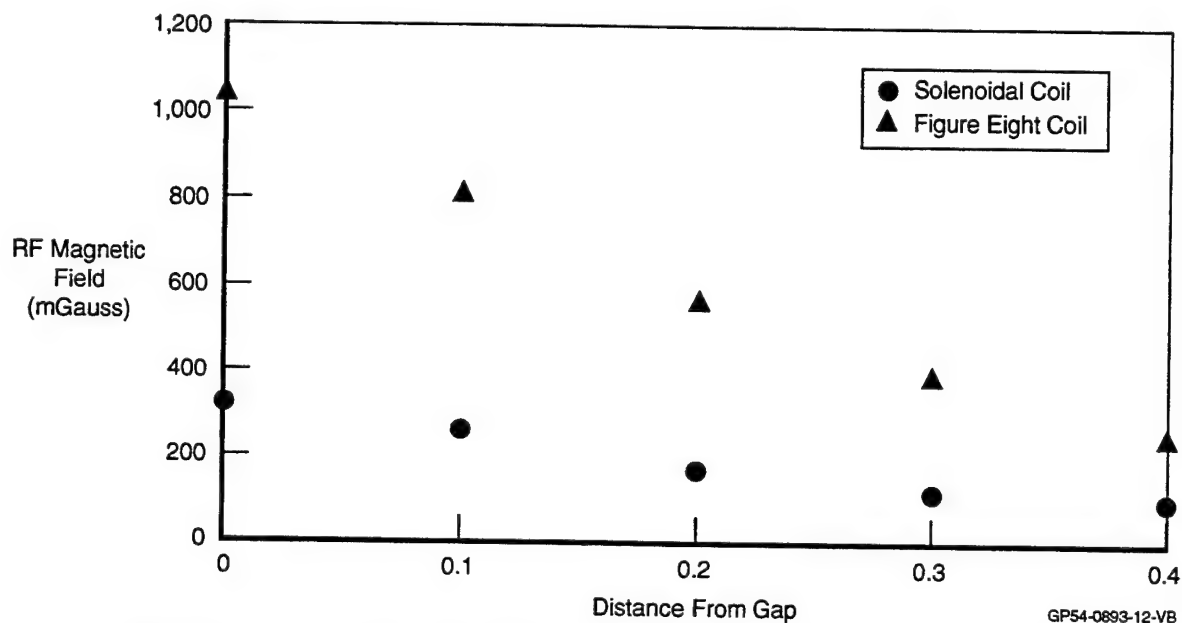
GP54-0893-12-VB

Figure 3.2.1-6. RF Magnetic Field Intensity as a Function of Coil Geometry.

62

The butt-joint simple structure was modified in order to decrease the gaps so that the structure was more representative of actual conditions. The water specimen was replaced with a latex rectangle (0.2 x 0.5 x 0.002 inches). Latex produces a convenient hydrogen NMR signal with a long spin-spin relaxation. The spacing between the OML and the substructure was approximately 0.006 inches, with a joint gap width of 0.012 inches. For this tight tolerance evaluation, the figure-eight coil was used. The RF magnetic field strength was measured at three points: (1) with the latex directly under the joint; (2) with the latex center 0.2 inches from the joint; and (3) with the latex center 0.4 inches from the joint. The data collected are shown in Figure 3.2.1-7. The results show that even with these tight spacings, RF magnetic field does penetrate to a certain extent. Once again, the data agree qualitatively with modelling results shown in Figure 3.1.1-2 in that the RF field decreases as the distance away from the gap increases.
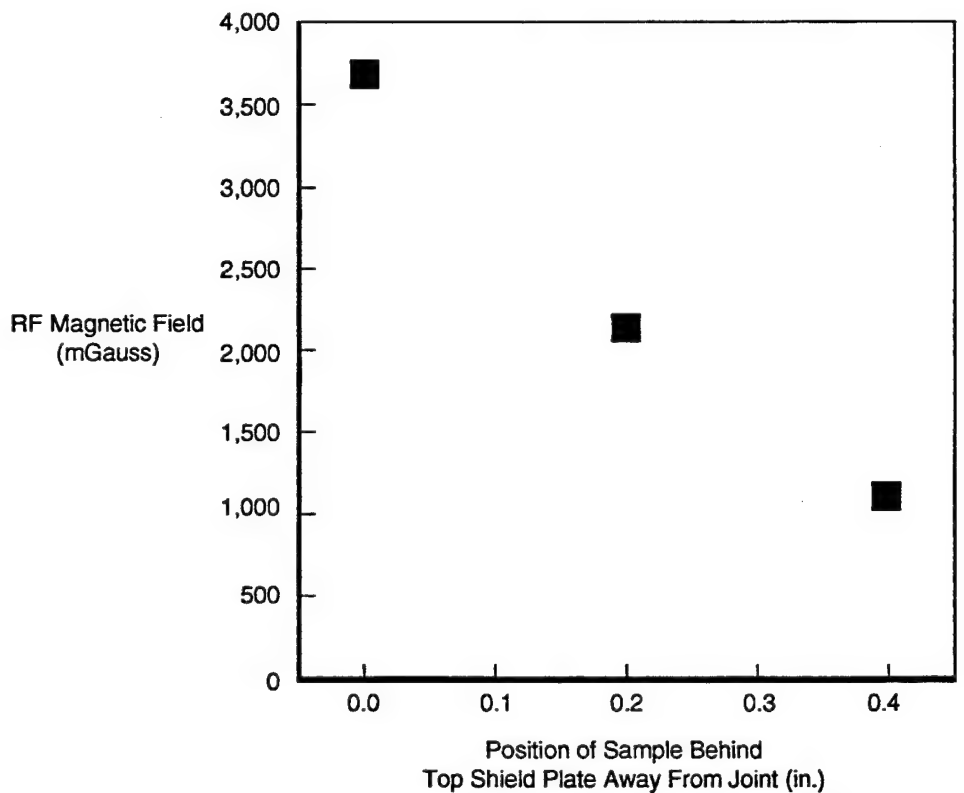
GP54-0893-60-VB

Figure 3.2.1-7. RF Magnetic Field Intensity Evaluated Using Figure-Eight Coil and Joint Gap Width of 0.006 in.

3.2.2 Lap Joint Configuration

In order to perform an evaluation similar to the butt-joint configuration, a simple structure was fabricated to simulate a lap joint. The lap joint simple structure is shown schematically in Figure 3.2.2-1
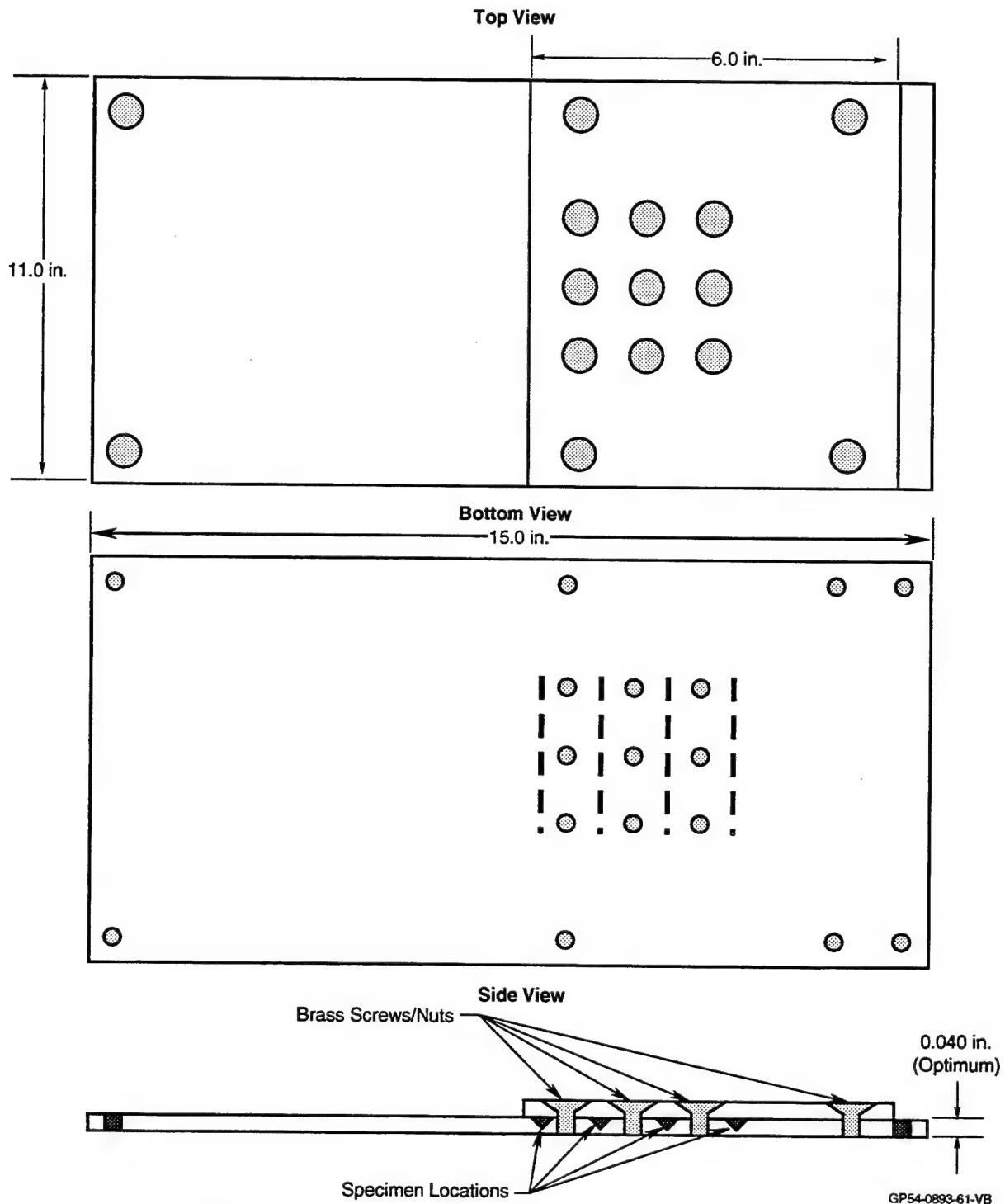
Figure 3.2.2-1. Schematic Representation of Lap-Joint Simple Structure Developed For RF Magnetic Field Evaluation.

and pictorially in Figure 3.2.2-2. The structure was constructed using 2024 sheet aluminum and was designed to contain nine brass screws to simulate an array of rivets near the joint. The array was inset from the edge of the lap joint by 0.5 inches. Since extremely small gaps in the overlap area were required, a latex rubber sheet was used as the hydrogen-bearing specimen in this evaluation. The 0.002 inch thick latex sheet was cut to dimensions of 0.1 x 0.5 inches. The specimen was placed in three positions: (1) half-covered by the overlapping plate in the joint; (2) specimen center 0.1 inches from the edge of the lap joint and (3) specimen center 0.3 inches from the edge of the joint. Like the butt-joint analysis, the NMR measurements were performed in the 2.0 Tesla electromagnet, which for hydrogen NMR, corresponds to a frequency of 85 MHz.

GP54-0893-82-VB
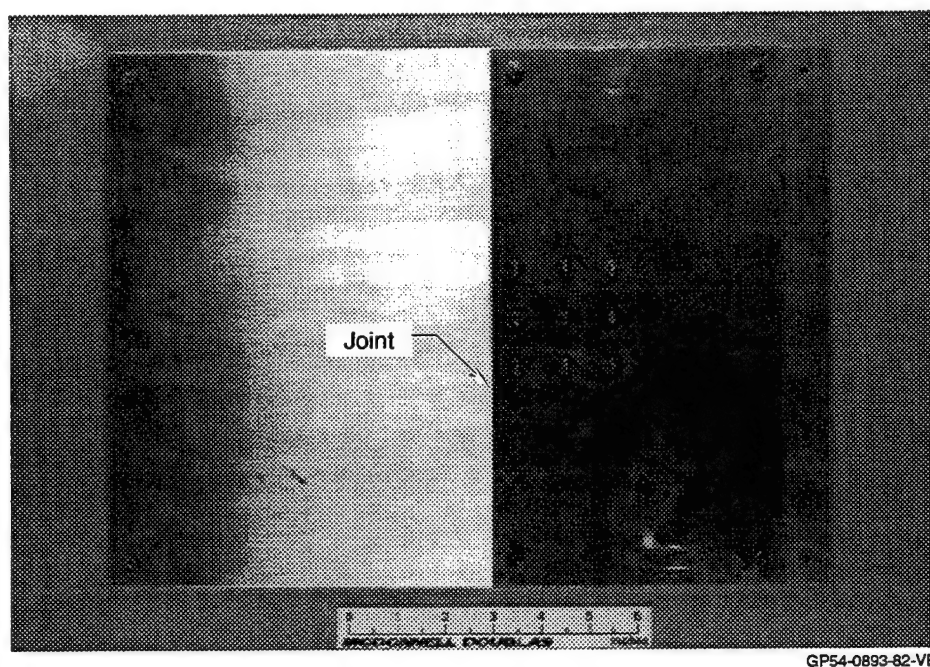
Figure 3.2.2-2. Photograph of Lap-Joint Simple Structure.

The RF magnetic field data relative to the three specimen positions in the joint are shown in Figure 3.2.2-3. The results show that the RF magnetic field decreases as the specimen is moved underneath the overlapping sheet of metal. As was noticed for the butt joint analysis, the experimental data agree qualitatively with the modelling results; however, the experimental results show that RF magnetic field intensity detected under the overlap is consistently lower than what was observed in the modelling exercises. Explanations for the lap joint inconsistencies between theory and experiment are believed to be consistent with those identified for the butt-joint.
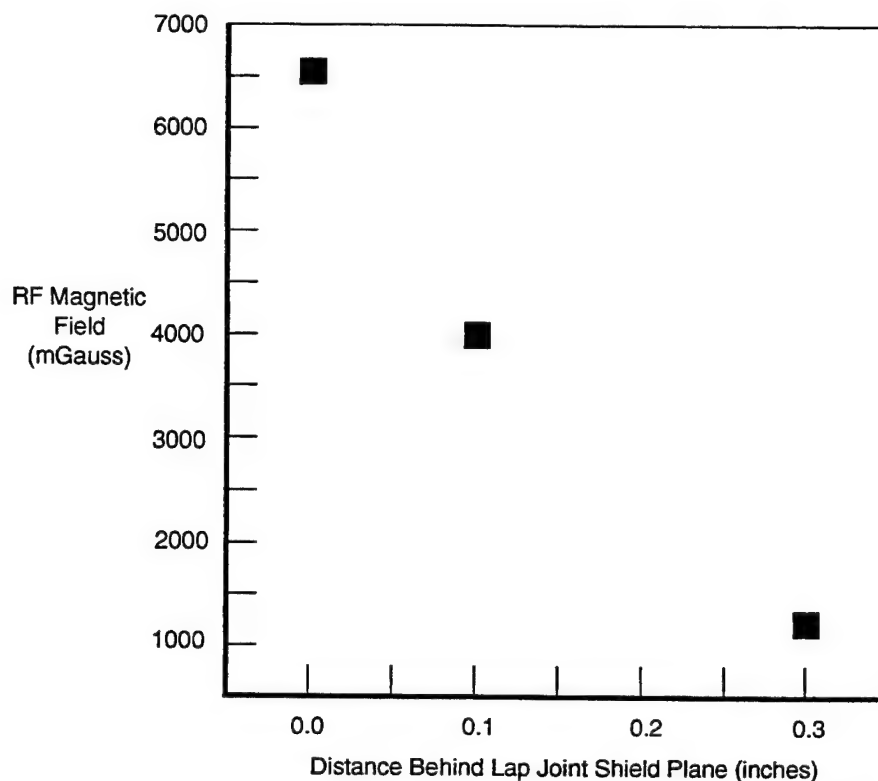
GP54-0893-62-VB

Figure 3.2.2-3. RF Magnetic Field Intensity Detected as a Function of Distance From the Edge of the Overlap in the Lap Joint Simple Structure.

3.2.3 Fastener Configuration

The behavior of the RF magnetic field around fasteners was the third consideration from an airframe structure standpoint. Two types of fasteners are typically encountered: Flush head and protruding head. With this in mind, two simple structures were fabricated: One with a countersunk hole containing a flush head fastener and one with a standard hole containing a protruding head fastener. These simple structures are shown schematically in Figure 3.2.3-1 and pictorially in Figure 3.2.3-2. The structures were fabricated from 7075 aluminum and contained titanium alloy fasteners. For each case, vacuum grease was used as the hydrogen bearing material needed to evaluate RF magnetic field penetration. Vacuum grease has a long spin-spin relaxation and is easy to place on and subsequently clean off. The measurements were performed using the 2.0 Tesla electromagnet, which corresponds to a hydrogen NMR frequency of 85 MHz.

66
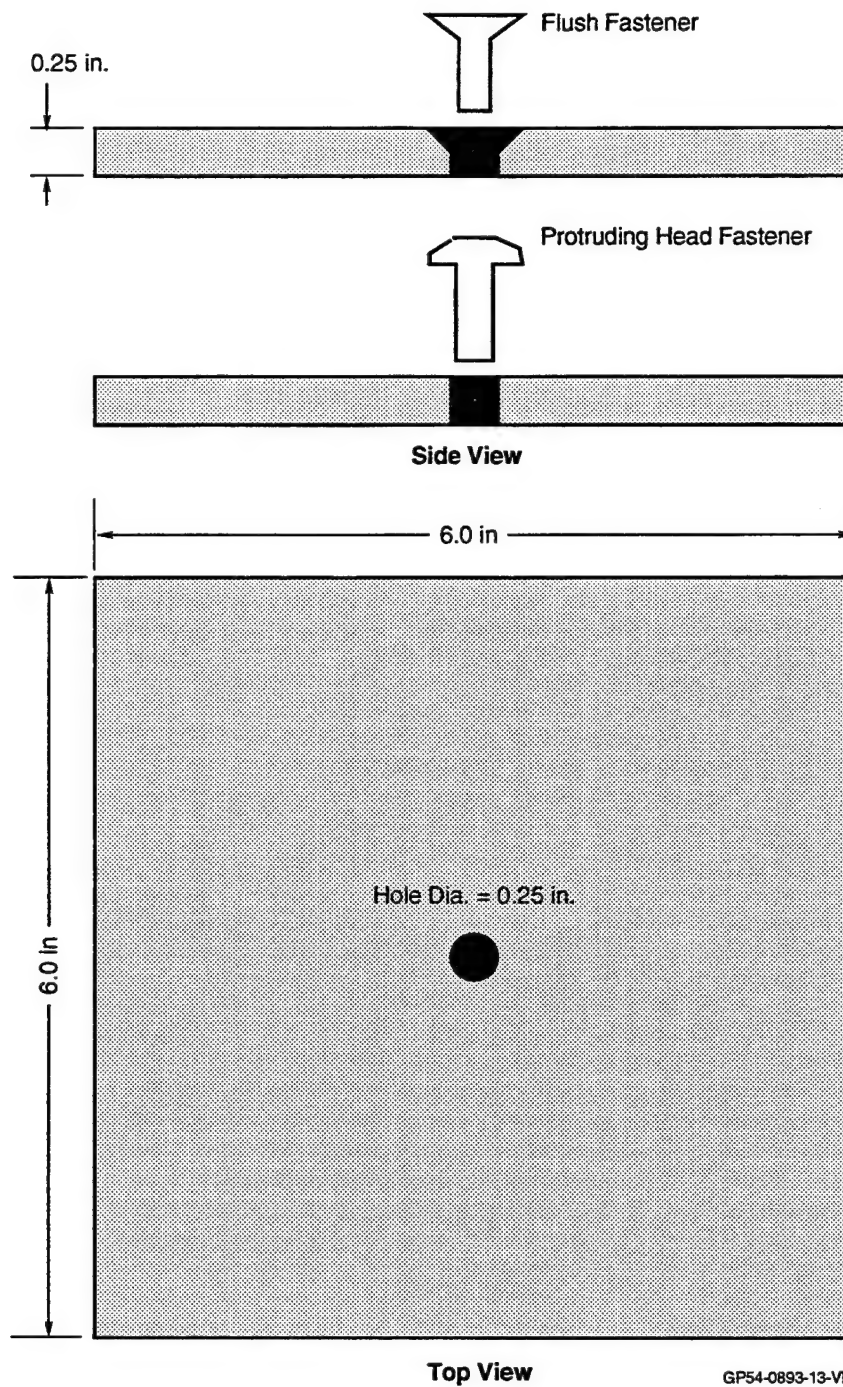
Figure 3.2.3-1. Schematic Representations of Fastener Hole Simple Structures Developed for RF Magnetic Field Evaluation.
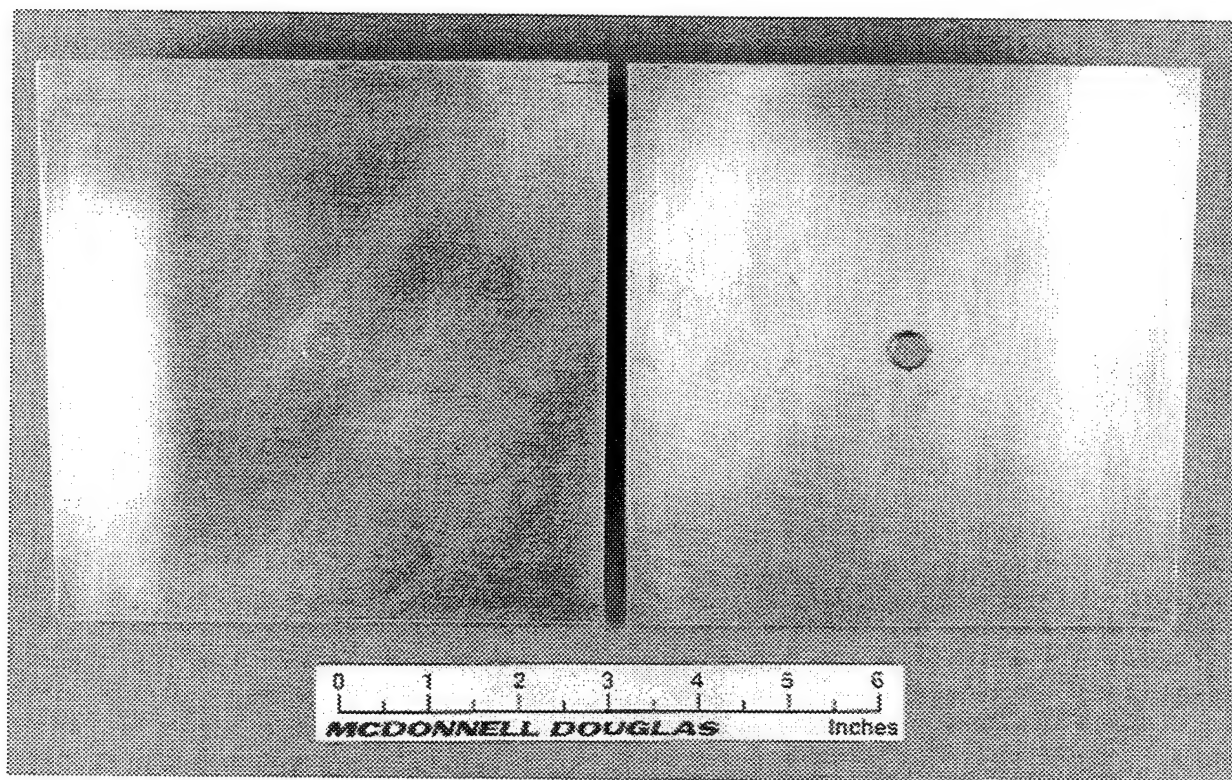
Figure 3.2.3-2. Photograph of Fastener Hole Simple Structures: Flush Head Fastener (Left) and Protruding Head Fastener (Right).

Flush Head Fastener: An NMR signal was obtained from the background hydrogen present in the probe and on the aluminum plate with the countersunk hole. These data are shown in Figure 3.2.3-3 and are labeled "no grease/no fastener." The signal resulted from 40 acquisitions made with the external 2.0 Tesla field. After the background signal was obtained, a thin film of vacuum grease was placed around the bore of the fastener hole and a second NMR signal was obtained. This signal is denoted as "grease/no fastener" in Figure 3.2.3-3. A titanium hi-lok flush head fastener was inserted into the hole and a third NMR measurement was made. This signal is identified in Figure 3.2.3-3 as "grease/fastener." The hydrogen NMR signal is clearly visible, both with and without the fastener present. The signal height does not change appreciably with the fastener installed; however, the signal duration (or apparent T_2^* of the vacuum grease) decreases dramatically. The decrease in T_2 is due to an increase in the external magnetic field inhomogeneity. As was presented in Section 2.3.6, the titanium fastener shows slight magnetic behavior (paramagnetic). This phenomenon can be seen here as it distorts the static external magnetic field in its vicinity, which causes a reduction in the signal duration.
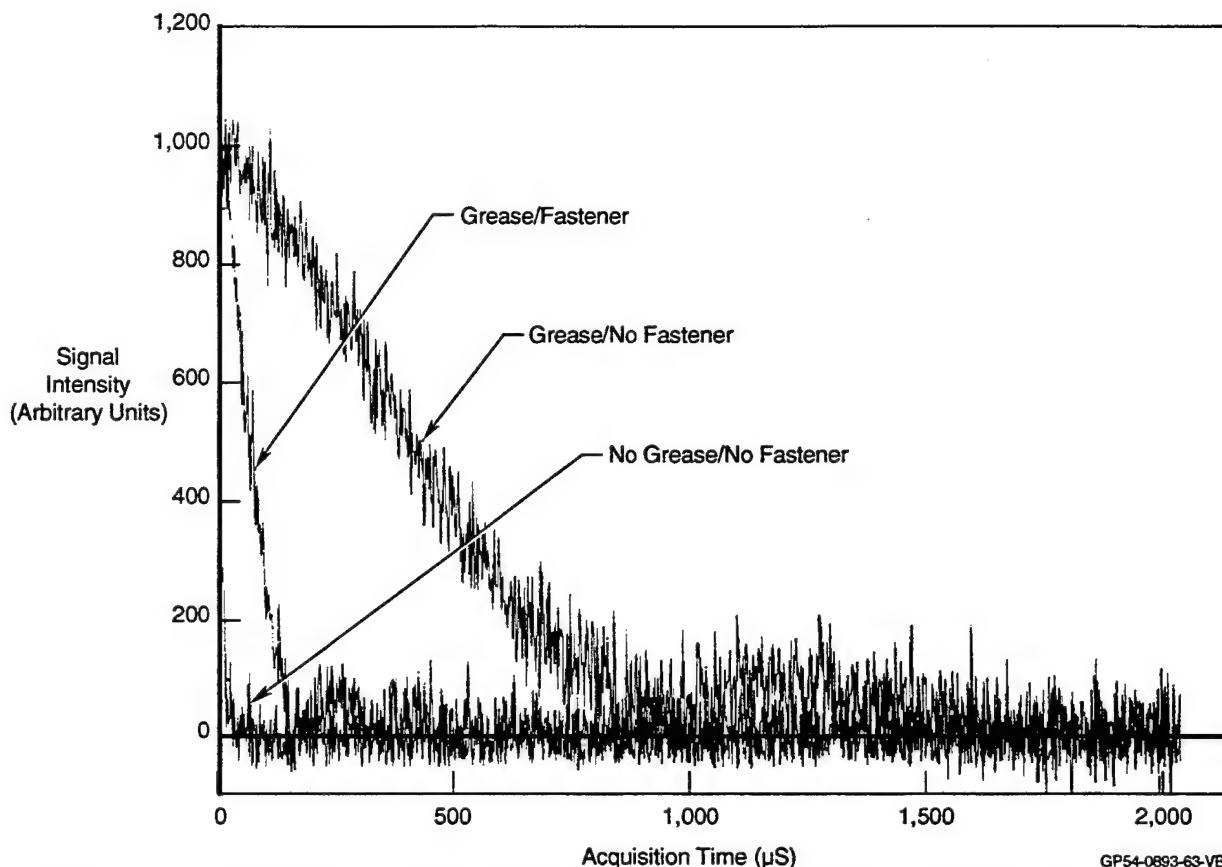
Figure 3.2.3-3. Comparison of Hydrogen NMR Signals From Flush Head Fastener Hole Evaluation.

Protruding Head Fastener: NMR data collected on the specimen containing the protruding head fastener is presented in Figure 3.2.3-4. The hydrogen NMR signal from the vacuum grease is clearly visible, both with and without the fastener present. The primary result from fastener installation is the reduction of the duration of the vacuum grease NMR signal. Because the decrease in the NMR signal duration (apparent T_2) is even greater with the protruding head fastener, it is reasonable to conclude that the fastener used here is more paramagnetic than the flush head fastener used for the corresponding investigation. One explanation for this may be that the protruding head fastener was made from a Ti-6Al-4V alloy higher in iron impurity content. Another might be the geometry of the protruding fastener head.

69
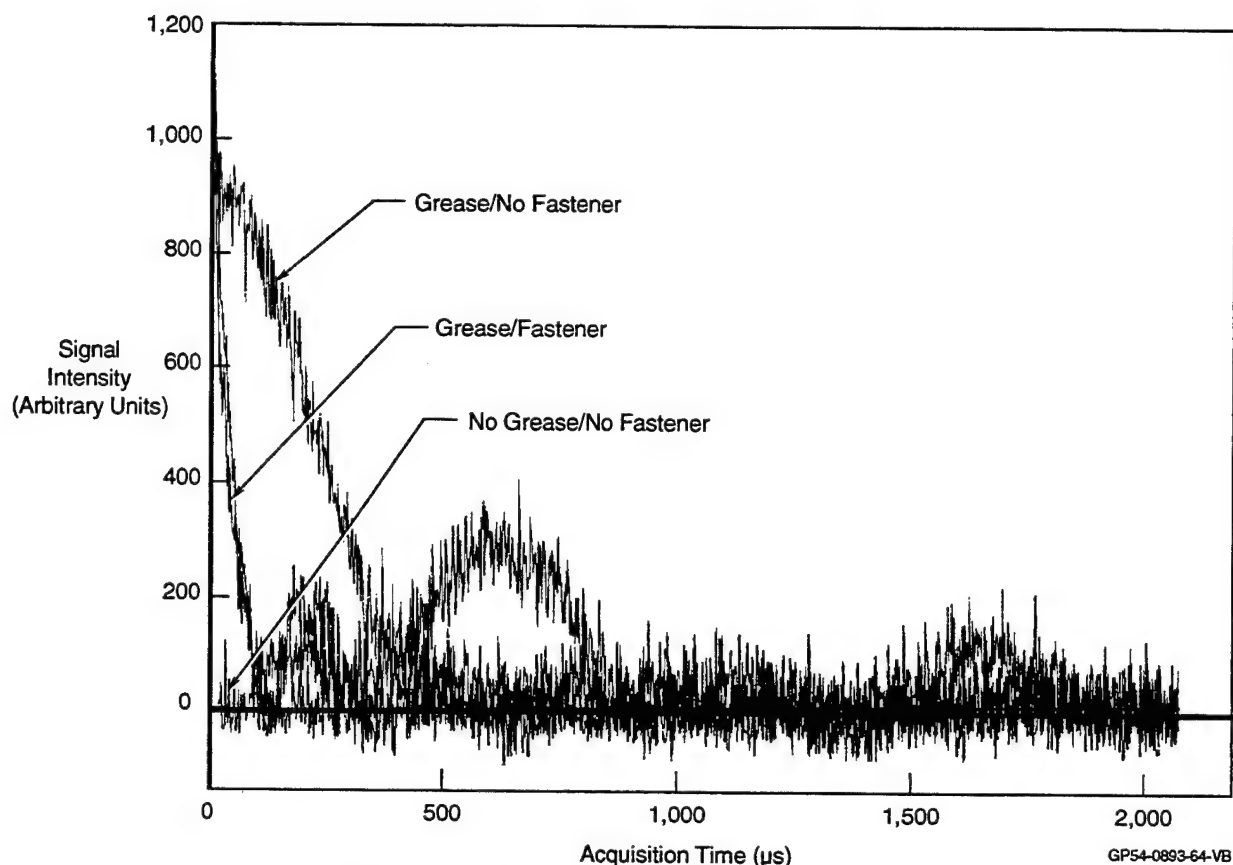
Figure 3.2.3-4. Comparison of Hydrogen NMR Signals From Protruding Head Fastener Hole Evaluation.

In both cases, the experiments revealed that RF magnetic field is detectable around installed fasteners. Although the RF magnetic field modelling around fastener holes did produce favorable results, it is not practical to directly compare the two sets of data since the experimental conditions differed somewhat from the model established for fastener holes. In another matter, while the titanium alloy fasteners may shorten the NMR signal of materials nearby, the hydrogen NMR signal from aluminum corrosion will not be affected as much as signals from grease and water. This is due to the fact that aluminum corrosion products have a much shorter spin-spin relaxation than water. It is important to point out that these results do show that RF will penetrate into and out of a fastener hole independent of the presence of paramagnetic materials.

3.3 NMR Evaluation of Corrosion in Simple Structures

Although it was determined that RF magnetic field does penetrate into gaps, joints and holes to certain extents, the question still remained regarding the detection of corrosion signals emanating from these areas. To determine this, the simple structures fabricated for the RF magnetic field experiments were used again with corrosion product selectively placed or with areas selectively exposed to an SO_2 environment for a period of time. The measurements were made using the 2.0 Tesla electromagnet at a frequency of 85 MHz for hydrogen NMR.

3.3.1 Butt Joint Configuration

The butt joint simple structure was reconfigured with a joint gap width of 0.090 inches and a plate spacing of 0.120 inches. The larger plate spacing was needed in order to accommodate a Teflon specimen holder. A small amount of aluminum corrosion product removed from a 2024-T3 panel exposed for 336 hours was placed in the specimen holder. The corrosion product covered an area of 0.5 x 0.5 inches . The specimen holder was subsequently placed in two positions relative to the joint: (1) directly beneath the joint and (2) so that the edge of the specimen was 0.25 inches away from the joint and completely covered by the OML skin. The corrosion signal was acquired using a saturate-wait-inspect pulse sequence. The saturation pulse was 2.0 ms and the wait/recovery time was 10 ms. When the corrosion specimen was placed directly beneath the gap, the inspection pulse was 20 μs; when the specimen was under the OML skin, an inspection pulse of 60 μs was used. The data collected are shown in Figure 3.3.1-1. It can be seen from these results that the sensitivity to corrosion decreases dramatically when the corrosion specimen is placed under the OML skin. Even though the RF magnetic field penetrates further, the signal/noise requirements for detection of a corrosion signal are not such that it can be reliably detected beyond 0.25 inches into the structure.
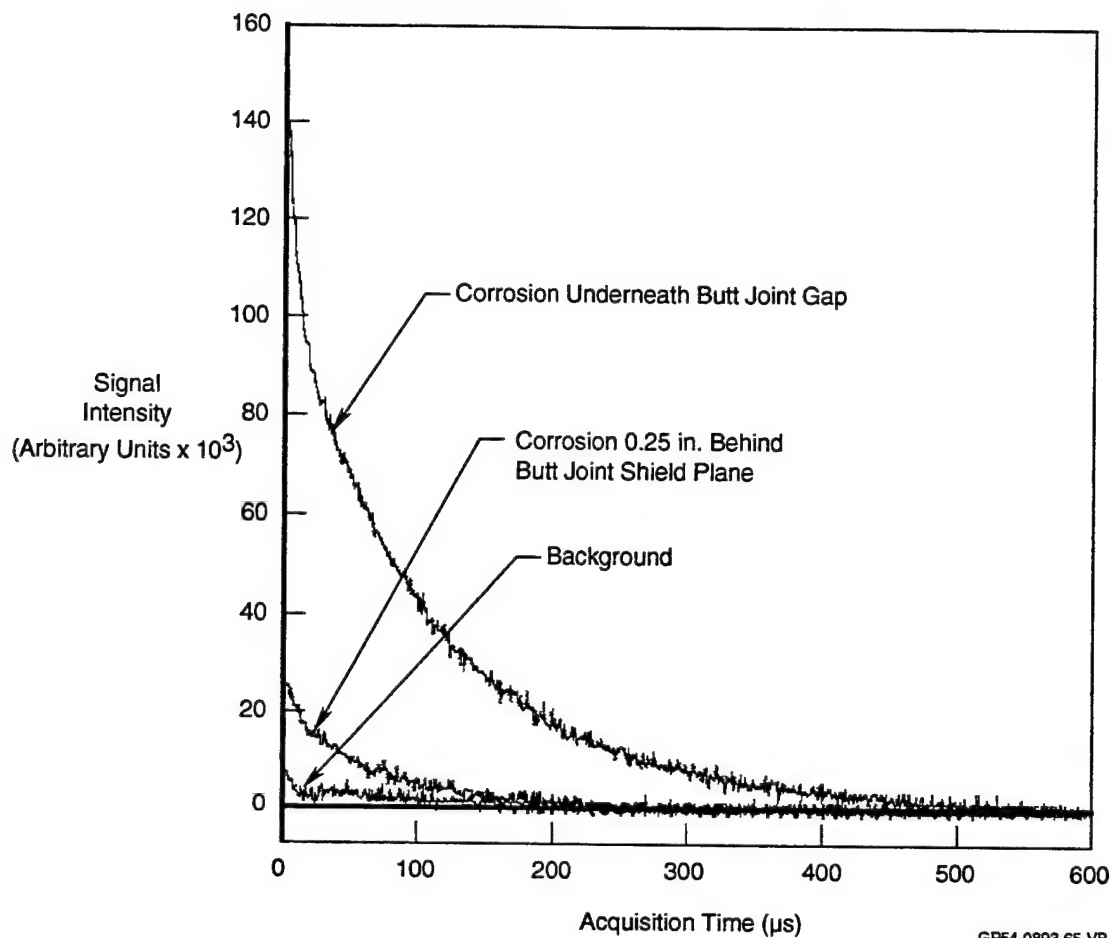
Figure 3.3.1-1. Comparison of Hydrogen NMR Signals From Corrosion Product in Butt-Joint Simple Structure (2.0 Tesla/85 MHz).

3.3.2 Fastener Configuration

Fastener plates identical in dimension and configuration to those used for the RF magnetic field modelling were used. However, to evaluate the ability to detect a corrosion signal, the structures were masked with only the fastener holes exposed and placed in an SO_2 environment for a 48 hour period. In both cases, the holes themselves were completely corroded. Some corrosion was noticed around the fastener holes outside of the hole areas. The bleed-out was more severe for the countersunk hole than for the standard hole.

Flush Head Fastener: The corroded plate with the countersunk fastener hole was evaluated and compared to the plate used for the RF magnetic field evaluation (no corrosion). The corroded fastener hole for the flush head fastener is shown in Figure 3.3.2-1. These signals were acquired using the figure-eight coil and a saturate-wait-inspect pulse sequence. The saturation pulse was 2.0 ms, the

72

recovery time was 1.0 ms and the inspection pulse was 5 μs. Transients numbering 10,000 were acquired and signal averaged. If this inspection were performed in a manner of rapid repetition instead of saturate-inspect, the total experiment time would be 20 seconds. Signals were acquired from the corroded region of the plate with and without the fastener installed. Signals were also collected from the baseline with the fastener installed. The data are presented in Figure 3.3.2-2. From these data, it can be seen that the flush head titanium fastener has a non-negligible magnetic susceptibility and slightly decreases the duration of the hydrogen signal emanating from the aluminum corrosion product. However, the signal intensity is not much less with the fastener in place than without the fastener present. As a result it can be concluded that corrosion can be detected around corroded flush head fasteners. For this case, since a significant amount of corrosion was noticed around the hole, it has to be assumed that the bulk of the signal comes from corrosion around the hole, not necessarily in the hole itself.
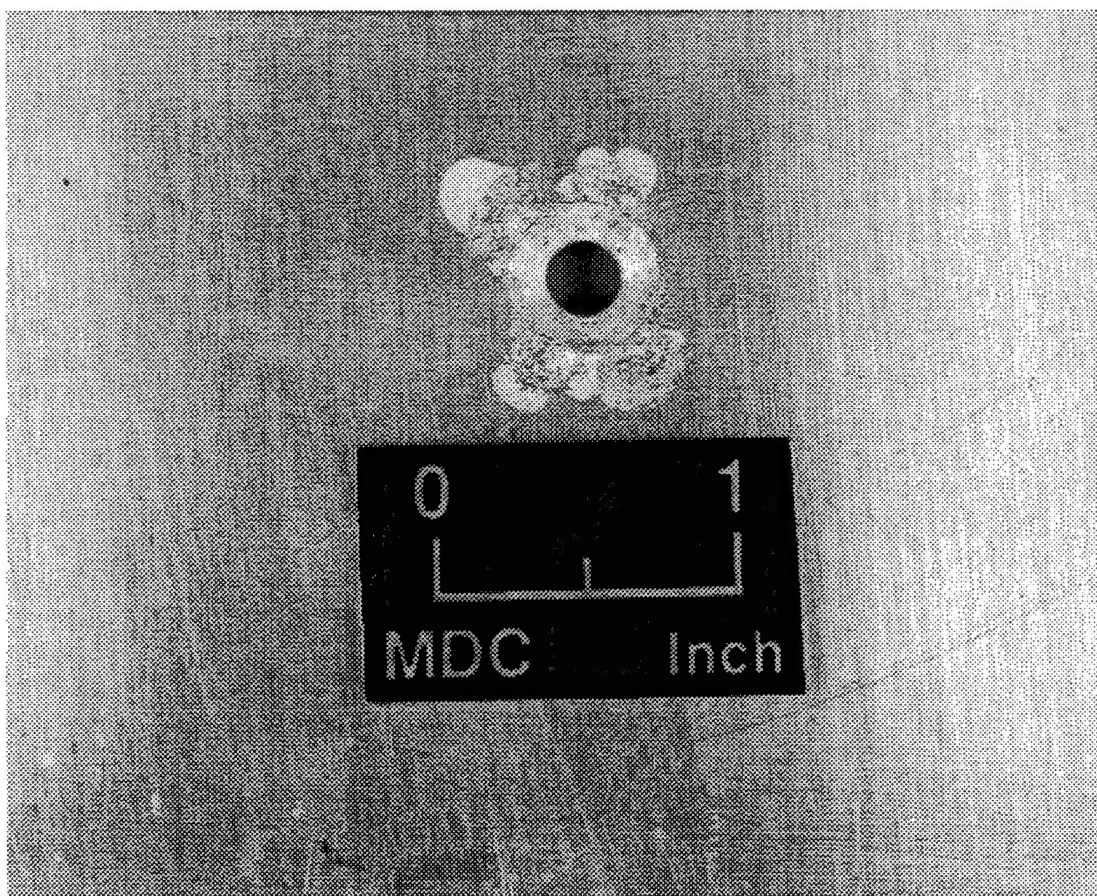
Figure 3.3.2-1. Photograph of Corrosion Around Countersunk Fastener Hole in Flush Head Fastener Hole Simple Structure.

Figure 3.3.2-2. Comparison of Hydrogen NMR Signals From Corrosion With and Without Flush Head Fastener Installed (Pulse Sequence: Saturate-Recover-Inspect/Recovery Time: 1 ms/10,000 Signal Averages/2.0 Tesla/85 MHz).

Protruding Head Fastener: The corroded plate with the protruding head fastener hole was evaluated and compared to the plate used for the RF magnetic field evaluation (no corrosion). The corroded fastener hole for the protruding head fastener is shown in Figure 3.3.2-3. A similar data acquisition procedure was used for the protruding head fastener with the results shown in Figure 3.3.2-4. As was observed when the signals were acquired during the RF magnetic field analysis, the protruding head fastener has a greater effect on magnetic field homogeneity (and hence, shortening the corrosion NMR signal duration) than did the flush head fastener. It appears that the protruding head fastener has a greater magnetic susceptibility than does the flush head fastener. Nevertheless, it was still possible to obtain the NMR signal from corrosion around the fastener hole with the fastener installed. In this case, it may be assumed that most of the signal emanated from corrosion under the fastener head. Even though this specimen had surface corrosion around the fastener, most of it was subsequently covered by the fastener head upon installation. Based on this observation, it may be concluded that most of the signal emanated from corrosion under the fastener head.

74

Figure 3.3.2-3. Photograph of Corrosion Around Fastener Hole in Protruding Head Fastener Hole Simple Structure.
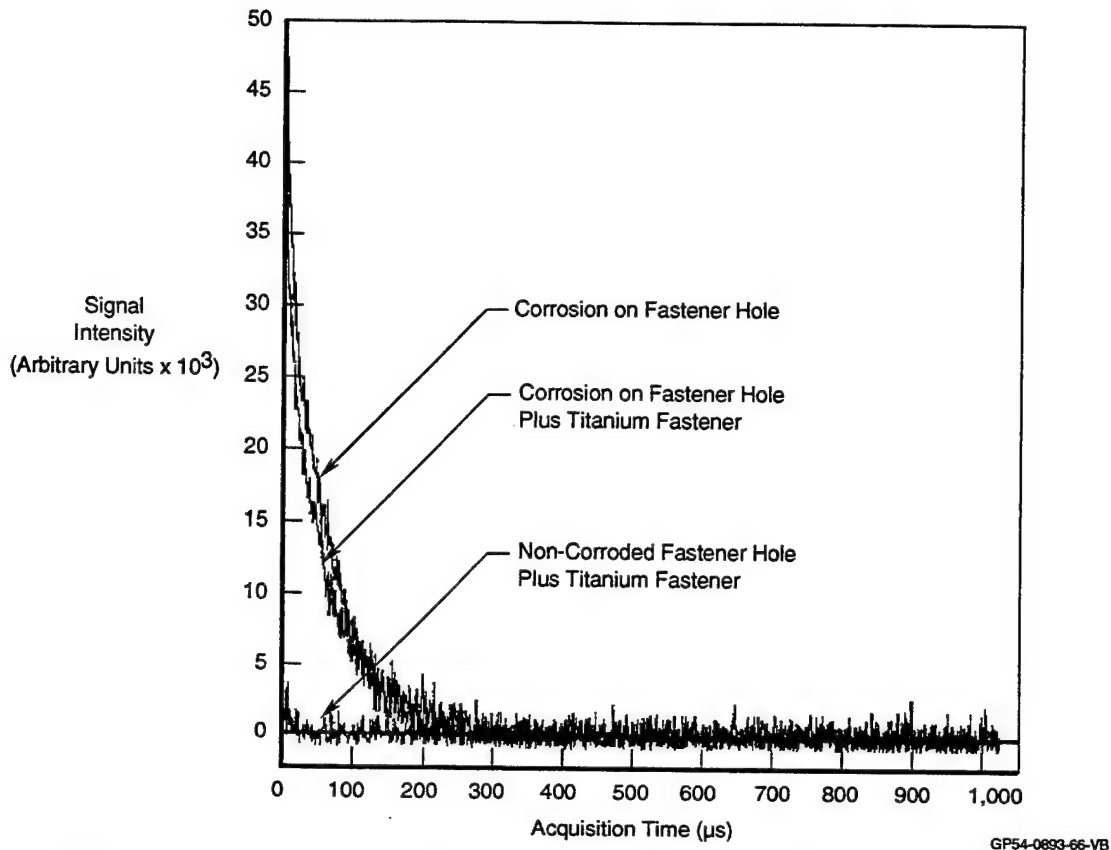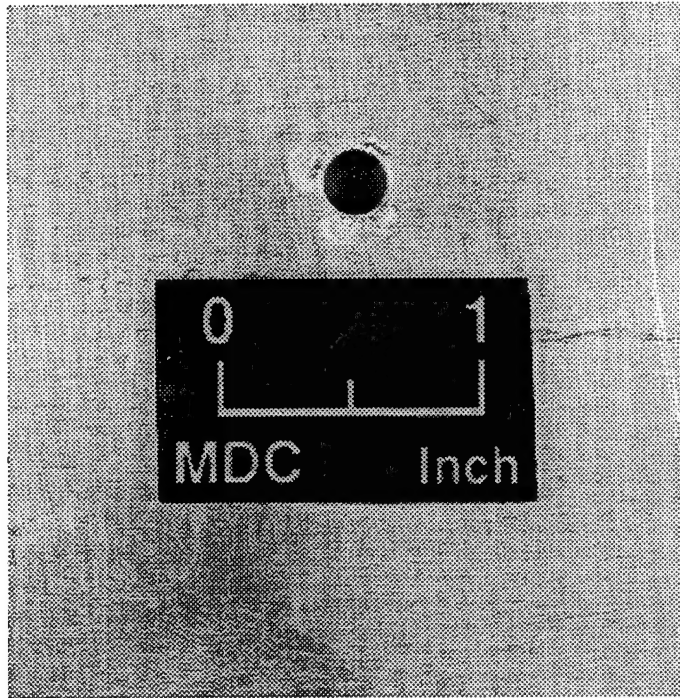

GP54-0893-67-VB
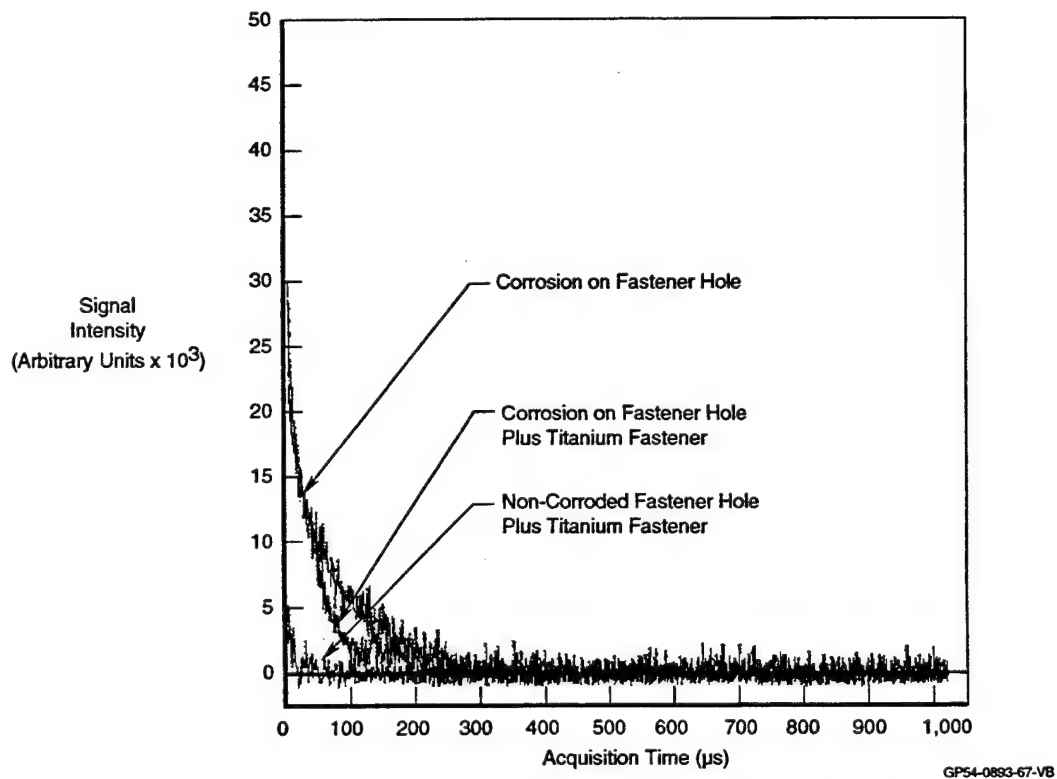
Figure 3.3.2-4. Comparison of Hydrogen NMR Signals From Corrosion With and Without Protruding Flush Head Fastener Installed (Pulse Sequence: Saturate-Recover-Inspect/Recovery Time: 1 ms/10,000 Signal Averages/2.0 Tesla/85 MHz).

3.3.3 Corrosion Under Included Materials

In order to determine the ability to detect corrosion under included materials, two 6.0 x 6.0 inch 2024 sheet aluminum specimens were fabricated. These specimens are shown in Figure 3.3.3-1 with paint, primer and sealant overlays. One of the sheet aluminum specimens was used as a standard and the other was exposed in an SO_2 environment for 336 hours. Both of these specimens were evaluated using a figure-eight surface coil in a static field of 2.0 Tesla. The pulse sequence used was saturate-recover-inspect with a 2.0 ms saturation pulse, a recovery time of 5 ms and an inspection pulse of 10 μs. The data, shown in Figure 3.3.3-2, compare the signal acquired from the corroded aluminum sheet to the signal acquired from the baseline aluminum standard. Signal averaging of 4000 transients was performed. If this experiment was performed using a quick repetition method instead of the saturate-inspect method, signal averaging would last for approximately 24 seconds. The technique clearly discriminates between corrosion and sheet metal with no corrosion. In Section 2.3.5, the results of the included material analysis showed that it may be possible to discriminate between a corrosion signal and other hydrogen bearing materials. To validate this assertion, sheets of paint (MIL-C-83286) and primer (MIL-P-85582) were placed between the sheet aluminum standards and the surface coil. The data collected using a 2.0 Tesla external magnetic field are shown in Figures 3.3.3-3 and 3.3.3-4 for the paint application and primer, respectively. From these data, it is clear that the corrosion signal can be clearly discriminated from paint or primer on the surface.

Figure 3.3.3-1. Photograph of Baseline and Corroded Aluminum Sheets With Paint, Primer and Sealant Overlays.
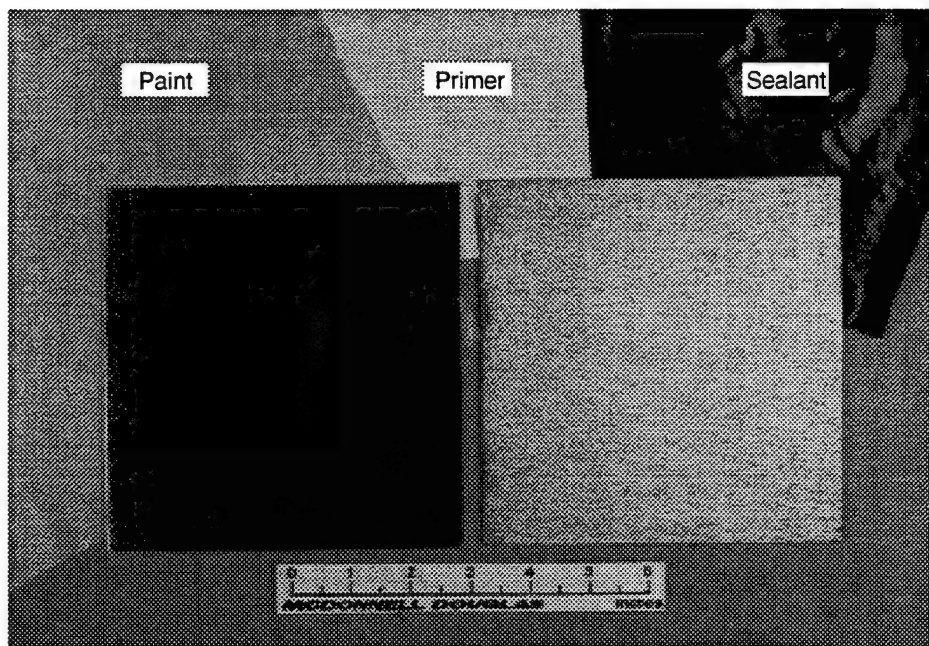
GP54-0893-83-VB

Figure 3.3.3-2. Comparison of Hydrogen NMR Signals From Baseline Sheet and Corroded Sheet Aluminum Simulating Surface Corrosion (Pulse Sequence: 2.0 ms Saturate-5.0 ms Recover-Inspect/4,000 Signal Averages/2.0 Tesla/85 MHz).
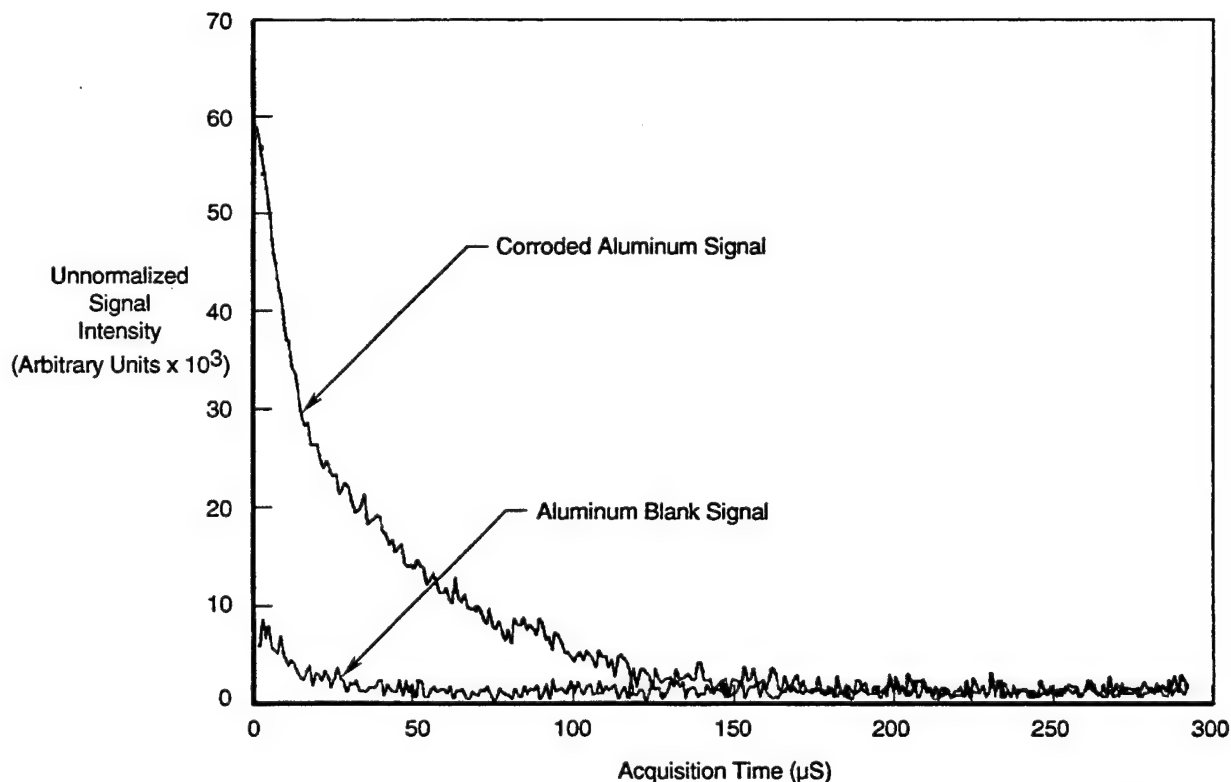
GP54-0893-68-VB

Figure 3.3.3-3. Comparison of Hydrogen NMR Signals From Baseline Sheet and Corroded Sheet Aluminum Simulating Surface Corrosion Under Paint (Pulse Sequence: 2.0 ms Saturate-5.0 ms Recover-Inspect/4,000 Signal Averages/2.0 Tesla/85 MHz).

Figure 3.3.3-4. Comparison of Hydrogen NMR Signals From Baseline Sheet and Corroded Sheet Aluminum Simulating Surface Corrosion Under Primer (Pulse Sequence: 2.0 ms Saturate-5.0 ms Recover-Inspect/4,000 Signal Averages/2.0 Tesla/85 MHz).

The experiments described above were then repeated using a static external magnetic field of 0.5 Tesla, which corresponds to a hydrogen NMR frequency of 21.25 MHz. The same pulse sequences were used for this lower magnetic field evaluation; however, the recovery time was decreased to 0.5 ms because the spin-lattice relaxation times for all materials decreases as the static external field is reduced. The saturation pulse was 2 ms and the inspection pulse was 4 μs. Transients numbering 10,000 were acquired and signal averaged. Using a quick repetition pulse method, the required duration of signal averaging would be approximately 15 seconds. The low external magnetic field data for corrosion on aluminum, paint on aluminum and primer on aluminum are shown in Figures 3.3.3-5, 3.3.3-6 and 3.3.3-7, respectively. The data shown here indicate that it is possible to detect corrosion on an aluminum surface, even at a relatively low field (0.5 Tesla), whether or not the surface is covered by paint or primer. This opens up the possibilities of detecting nascent corrosion under paint and primer using a much smaller magnet. This would be essential if a system was to be developed for practical inspection applications.

Figure 3.3.3-5. Comparison of Hydrogen NMR Signals From Baseline Sheet and Corroded Sheet Aluminum Simulating Surface Corrosion (Pulse Sequence: Saturate-0.5 ms Recover-Inspect/0.5 Tesla/21.25 MHz).
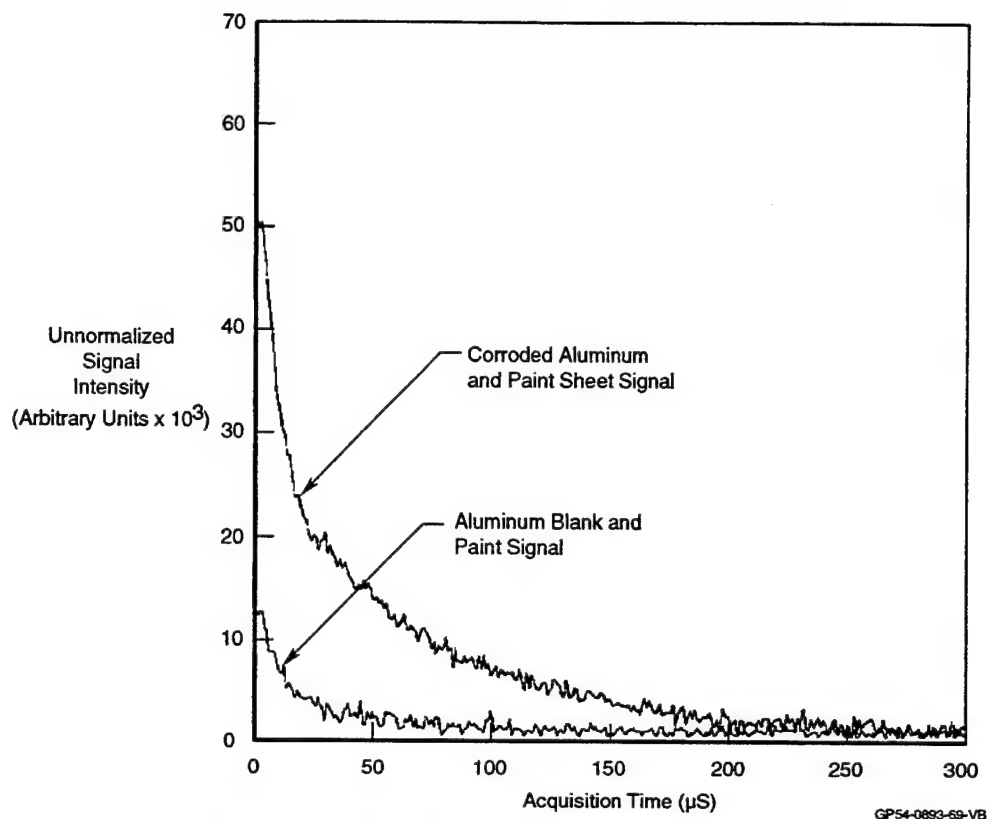
Figure 3.3.3-6. Comparison of Hydrogen NMR Signals From Baseline Sheet and Corroded Sheet Aluminum Simulating Surface Corrosion Under Paint (Pulse Sequence: Saturate-0.5 ms Recover-Inspect/0.5 Tesla/21.25 MHz).
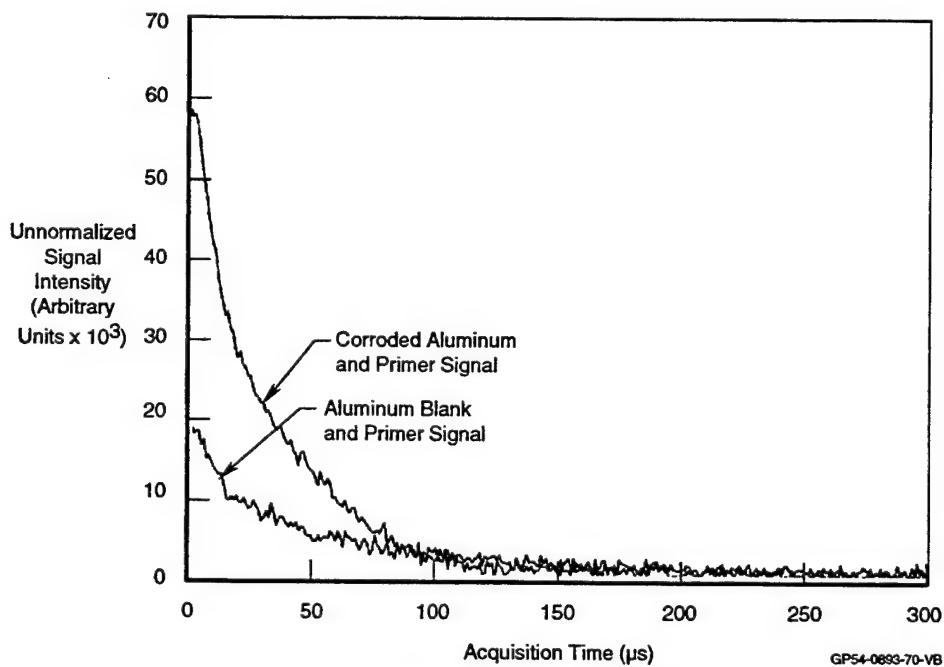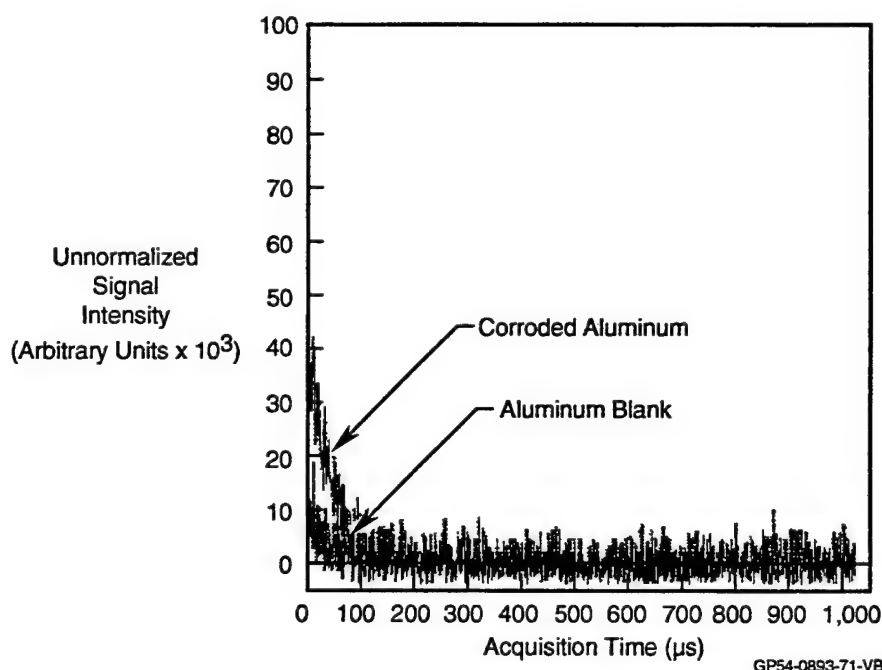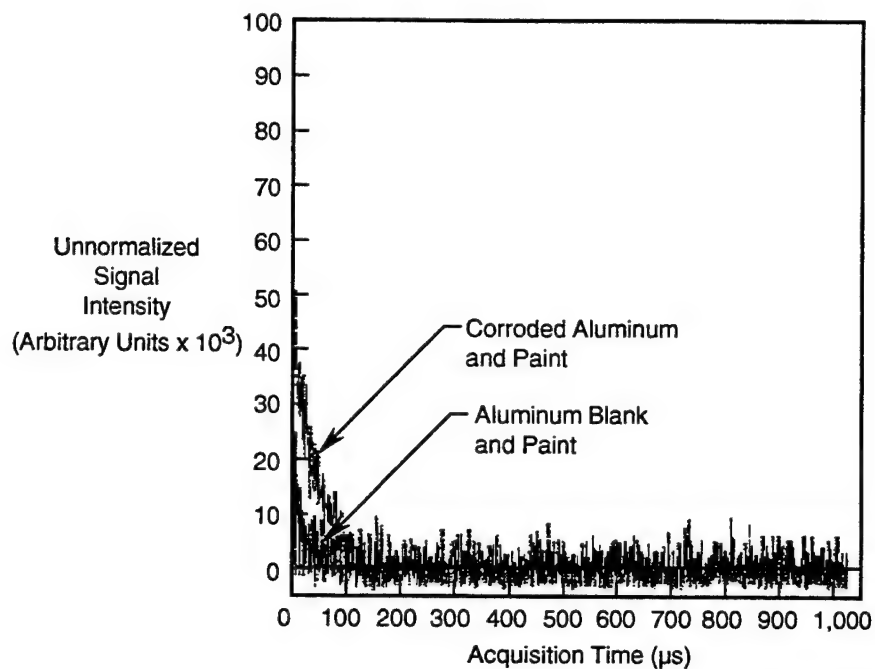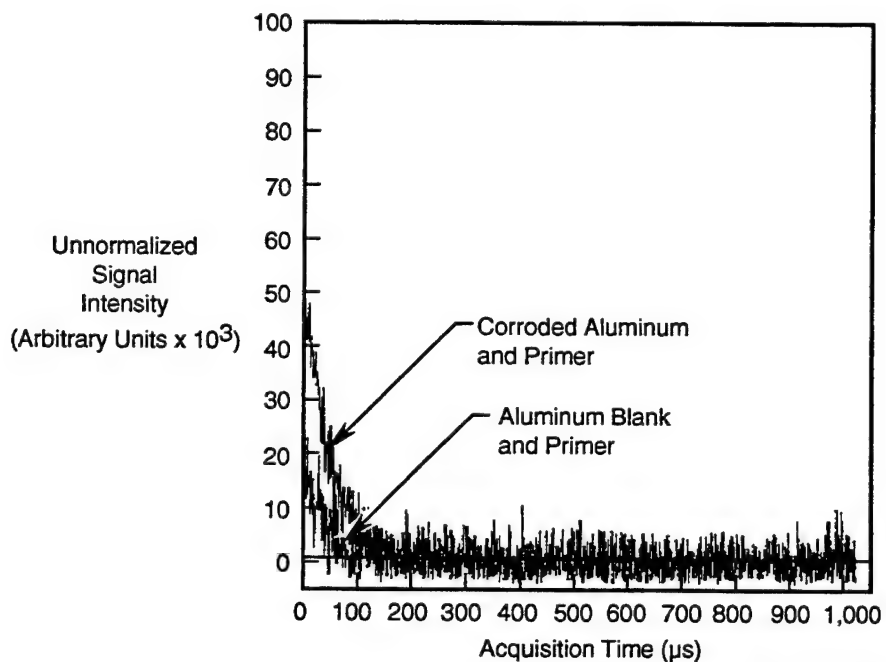

Figure 3.3.3-7. Comparison of Hydrogen NMR Signals From Baseline Sheet and Corroded Sheet Aluminum Simulating Surface Corrosion Under Primer (Pulse Sequence: Saturate-0.5 ms Recover-Inspect/0.5 Tesla/21.25 MHz).

4.0 CONCLUSIONS

The overall objective of this program was to evaluate the capabilities of nuclear magnetic resonance (NMR) as a tool for the quantitative assessment of corrosion in metallic airframe structures. The results obtained during this program indicate that NMR has potential in becoming a practical nondestructive evaluation method for some aircraft inspection applications. The following provides detailed assessments of corrosion sensitivity of NMR and the feasibility of using NMR for inspection of metallic joints, in and around fastener holes and under aircraft coatings.

4.1 Corrosion Sensitivity Using NMR

Both aluminum and hydrogen NMR techniques were found to be extremely sensitive to corrosion at levels far below those detectable using conventional NDE methods. Corrosion layer thicknesses between 0.2 and 2.0 micrometers were detected using both methods; however, the hydrogen technique has the greatest potential for becoming an inspection method due to adequate sensitivity at lower magnetic field strengths. Also, general correlations were noted between NMR signal and exposure times for the alloys investigated. Although this was encouraging, more work needs to be performed to adequately assess the ability of using NMR to quantify the amount of corrosion present.

4.2 Detection of Corrosion in Joints

Both RF modelling and experimental verification showed that the RF magnetic field does penetrate gaps in both butt joint and lap joint configurations. These results were keys to assessing the feasibility of detecting corrosion in the substructure. In addition, the sensitivity was sufficient to detect corrosion signals emanating from the joints and, to some degree, underneath the outer mold line skins. Figure 4.2-1 presents a summary of conclusions for inspection of joints using NMR. Butt joints, where joint gaps in the range of 0.005 to 0.100 inches are not uncommon, provide adequate avenues for RF magnetic field penetration. However, it was experimentally determined that a corrosion signal could only be reliably detected up to 0.25 inches away from the joint. Lap joints, which are typically in contact, are more difficult to evaluate unless corrosion or structural loading creates small gaps (on the order of 0.005 inches) in the overlap area. Detection of corrosion in second or third layers becomes more difficult given the limited avenues for RF magnetic field penetration.

81

Application	Potential for Field/Depot Inspection Technique
Corrosion in Butt-Joint • Joint Area • Under OML Skin (<0.25 in) • Under OML Skin (>0.25 in)	High Moderate Low
Corrosion in Lap Joint • Under OML Skin (<0.25 in) • Under OML Skin (>0.25 in)	Moderate Low

GP54-0893-14-VB

Figure 4.2-1. Summary of Conclusions For Detection of Corrosion in Joints Using NMR

4.3 Detection of Corrosion Around Fastener Holes

Given the tight tolerances and fastener material varieties, application of NMR to detection of corrosion around fastener holes is possible. A summary of conclusions relative to inspection for corrosion in and around fastener holes using NMR is shown in Figure 4.3-1. More than any other characteristic, the fastener material seems to have the greatest effect on the NMR signal. Detection of surface corrosion around fasteners is possible if the fastener materials are aluminum or titanium, although titanium fasteners do have some magnetic susceptibility. CRES (PH13-8Mo) fasteners, which are highly magnetic, render the measurement ineffective due to the severe broadening of the signal in the vicinity of the fastener.

Application	Potential for Field/Depot Inspection Technique
Corrosion Around Fasteners • Surface Corrosion • Corrosion in Hole	High Moderate
Fastener Types • Flush Head • Protruding Head	High Moderate-High
Fastener Materials • Aluminum • Titanium • CRES (PH13-8Mo)	High Moderate-High Not Applicable

GP54-0893-15-VB

Figure 4.3-1. Summary of Conclusions For Detection of Corrosion Around Fasteners Using NMR

4.4 Detection of Corrosion Under Coatings

Detection of nascent corrosion under coatings is the most promising of the applications investigated relative to NMR. This potential as a function of coating type is shown in Figure 4-4-1. Paints and primers, although they are both hydrogen bearing materials, do not inhibit corrosion signals emanating from underneath these coatings. Epoxy-based adhesives do not inhibit NMR corrosion signal detection. Sealants, however, do have relatively short free induction decay times, but with the use of inversion recovery sequences, the corrosion signal may be detected with no signal from the sealant. The one coating material that renders NMR ineffective is magnetic radar absorbing material (MagRAM). Much like the CRES fasteners, an NMR signal in the presence of MagRAM will be broadened to the point that it cannot be detected.

Application	Potential for Field/Depot Inspection Technique
Paint/Topcoat	High
Primer	High
Film/Foaming Adhesive	High
Polysulfide Sealant	Moderate-High
MagRAM	Not Applicable

GP54-0893-16-VB

Figure 4.4-1. Summary of Conclusions For Detection of Corrosion Under Coatings Using NMR

4.5 Environmental/Economic Considerations

To facilitate an NMR system for field or depot inspections, the effects of the system on the environment must be addressed. Stray field effects from the magnet pose the greatest concern relative to field operations. Magnetic field strengths in excess of 0.3 mT may interfere with aircraft communication and navigational devices located within close proximity to the magnet [1]. Stronger stray fields in excess of 0.5 mT may disturb some heart pacemakers, erase magnetic cards and storage devices and adversely affect watches and micro-mechanical devices. Most of the stray field concerns and safety precautions relate to high-field superconducting magnets; however, one-sided, permanent magnets should also be monitored to determine the extent of the stray fields. For electromagnets, the safety measures are usually less stringent relative to stray magnetic fields as they tend to be confined to the poles of the magnet.

In addition to stray field concerns, strong attraction of ferromagnetic objects may occur at close proximities to the magnet. The attractive force depends on the mass of the object and the distance from the magnet. It increases rapidly when the distance is reduced. Hence, it may change from barely noticeable to uncontrollable in a very short distance.

Superconducting magnets use liquid nitrogen and helium as cooling agents. These liquids expand their volume by a factor of 700 during evaporation and warm-up [1]. The gases are nontoxic and completely harmless as long as adequate ventilation is provided to avoid suffocation. During normal operation, only 100 to 150 cubic feet of nitrogen are evaporated per day. However, during a magnet quench, 1500 to 3500 cubic feet of helium gas are produced within a short time. In both cases, adequate ventilation is required.

From the standpoint of hardware cost, NMR equipment can range from reasonable (<$100K) to substantial (>$500K). The overall cost of an NMR system is driven by the magnet. The cost of the supporting electronics (i.e., transmitter/receiver, computer system, etc.) are minimal in comparison. For the application described in this report, the magnet would have to be a one-sided permanent magnet, an example of which is shown in Figure 4.5-1. This magnet, developed for NAWC-Lakehurst under an SBIR program, was specifically designed to detect moisture in aerospace structures. The initial cost impact associated with the introduction of one-sided NMR systems into Air Force environments would be significant. These initial costs would include hardware, personnel training and facilities modifications.
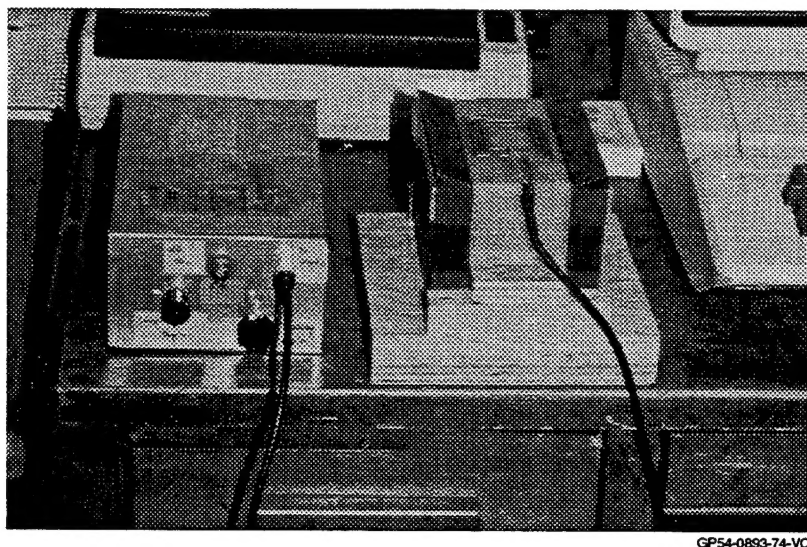
GP54-0893-74-VC

Figure 4.5-1. Permanent, One-Sided Magnet (0.125 Tesla/5 MHz) Developed For Detection of Moisture in Aerospace Structures

5.0 RECOMMENDATIONS

The results obtained in this program provide insight into the feasibility of using NMR as a nondestructive inspection method for corrosion in metallic structures. Although potential applications were identified, additional work must be performed in the exploratory development domain before prototype hardware requirements can be defined. The following are tasks identified to continue exploratory development of the NMR technique for corrosion detection and quantification:

- It was determined that hydrogen signals exist in corrosion products. The elemental characterization work performed in this study was limited to Auger electron microscopy techniques that cannot quantify hydrogen content. In order to determine the amount of hydrogen necessary to generate an NMR signal and provide more detailed information on the hydration phenomenon in general, a hydrogen-sensitive measurement technique needs to be used on specimens similar to those evaluated in this study.

- There is a definite correlation between the amount of corrosion product present and an NMR signal. In the current study, the approach was to measure the amount as a function of product thickness on the surface. Given the variability of corrosion product thickness over a given surface area, the correlation between thickness and NMR signal was identifiable, but not definite. An additional study by which the mass of the corrosion product on a given surface is used as the correlating factor may provide more definitive results and supplement the thickness results previously obtained.

- NMR has shown to be sensitive to corrosion under coatings, such as paints, primers and sealants. It is not fully understood whether or not the corrosion initiates only by moisture intrusion through cracks, gaps and crevices, or by moisture diffusion through the coating itself. NMR is a proven tool for moisture detection and may be helpful in determining if moisture diffusion through coatings is a possible precursor to galvanic activity in the substructure. It is recommended that a study such as this be performed prior to technique development for corrosion detection under coatings using NMR.

- The modelling performed in this program was primarily two-dimensional in nature using a three-dimensional modelling code developed for low observable applications. Although the modelling results showed qualitative agreement with the experimental data, some discrepancies were noted. Most of the discrepancies were not related to the rate of decrease of the RF magnetic field, but the level at which the field reaches equilibrium underneath the outer mold line skin. Initial results indicate that the intensity of the RF magnetic field underneath the outer mold line skin is strongly dependent on the size of the source. Future modeling efforts should include a more detailed study of source size versus field intensity at specific locations. Also, more detailed work needs to be performed relative grounded versus ungrounded cases, especially at fastener locations.

- The feasibility of using NMR at low fields was given a cursory look in this program. For NMR to become a practical, portable inspection method, detection of corrosion must be repeatedly demonstrated at magnetic field strengths of less than 0.5 Tesla. Now that desired sensitivities have been established at higher fields, adequate sensitivities must be demonstrated at lower fields. To accomplish this, coil designs, pulse sequences and signal processing techniques need to be investigated as a function of lower external magnetic field strength.

6.0 REFERENCES

1. D.D. Palmer and C.G. Fry, "Feasibility Study of NMR as a Nondestructive Inspection Method", U.S. Navy Report NAWCADLKE-MISC-02T-0026, June 1993.

2. C.P. Slichter, *Principles of Magnetic Resonance*, Springer-Verlag Press, Berlin, 1990

3. Bloembergen, Pound and Purcell, Phys. Rev., **73** (1948)

4. Lowe and Norberg: Phys. Rev., **107**, 46 (1957)

5. Ellet, Gibby, Haeberlen, Huber, Mehring, Pines and Waugh: Adv. Magn. Res, **5**, 117 (1971)

6. D.D. Palmer, D. J. Leopold, D.M. Snyderman and M.S. Conradi, "Investigation of New Materials Using NMR", U.S. Navy Report NAWCADLKE-MISC-02T-0034, May 1994

7. Metals Handbook, Desk Edition, "Materials for Corrosion Resistant Fasteners", American Society for Metals, Metals Park, OH, 1985.

8. F-15 Fastener Installation Procedure Manual, McDonnell Aircraft Company, 01 March 1977.

9. J. Putnam, L.Medgyesi-Mitschang and M. Gedera, "CARLOS-3D: Three-Dimensional Method of Moments Modelling Code", Technical Manual, McDonnell Douglas Aerospace, 10 December 1992.

10. J.A. Stratton, *Electromagnetic Theory*, McGraw-Hill, New York, 1941.

11. A.W. Maue, Z. Phys., **126**, 7 (1949)

12. A.F. Peterson, Proc. IEEE, **10** (1991)